Power Consumption Models for Tracked and Wheeled Small Unmanned Ground Vehicles on Deformable Terrains

by

Tianyou Guo

A dissertation submitted in partial fulfillment
of the requirements for the degree of
Doctor of Philosophy
(Mechanical Engineering)
in the University of Michigan
2016

Doctoral Committee:

Professor Huei Peng, Chair
Assistant Research Scientist Tulga Ersal
Professor Noel C. Perkins
Associate Professor Adamantia M. Zekkos

ACKNOWLEDGEMENTS

TABLE OF CONTENTS

LIST OF FIGURES

LIST OF TABLES

NOMENCLATURE

SUGV	Small Unmanned Ground Vehicle
FEM	Finite Element Method
DEM	Discrete Element Method
DOF	Degree of Freedom
CG	Center of Gravity
ICR	Instantaneous Center of Rotation
RGB	Red Green Blue
HSV	Hue Saturation Value
SVD	Singular Value Decomposition

ABSTRACT

Small unmanned ground vehicles (SUGVs) are widely used in nuclear, military, space exploration, agriculture, mining, and construction applications. Energy storage, management, and efficient conversion are always critical issues for SUGV designs and controls, and fast and accurate power consumption models are required to avoid immobilization by energy depletion or reduced traction capability.

This dissertation studies methods to improve the locomotion power consumption modeling for both tracked and wheeled SUGVs. As SUGVs are usually operated off-road, terramechanics models can be used to capture the relationship between the running gear and terrain. Most SUGVs use skid steering because of its simplicity and robustness. However, due to the sliding between the running gear and terrain, skid steering can consume a lot of the propulsion power. Thus the skid steering must be included in the power consumption models of SUGVs.

Single track-terrain and single wheel-terrain interaction are first studied and modeled based on terramechanics theory. Skid steering maneuver is then studied using three widely used models of tracked vehicles. None of these models achieve desired computation efficiency and accuracy simultaneously. We subsequently developed a finite element skid steering (FESS) model, which is used for both tracked and wheeled vehicles, and achieve the same accuracy as Wong's model and in the meantime is computationally efficient. The accuracy of the FESS model is validated by experiments using a 6-wheel-drive track/wheel interchangeable test robot on dry sand. Two case studies are conducted on an imaginary Packbot (in 4-wheel, 6-wheel, and track configurations) in two missions (patrolling an area and search and retrieve). Finally, a design comparison between tracked and wheeled configurations on SUGVs is studied, and general conclusions regarding power consumption and mobility are drawn.

CHAPTER 1

Introduction

1.1 Motivation

1.1.1 Small Unmanned Ground Vehicles

Small Unmanned Ground Vehicles (SUGVs) are widely used in nuclear, military, space exploration, agriculture, mining, and construction applications, because they require significantly fewer resources than manned missions. For example, NASA rovers Spirit and Opportunity (landed on Mars in 2004) and Curiosity (landed on Mars in 2012) have provided useful information about Mars for years. The Yutu lunar rover landed on the Moon in 2013 as China's first successful unmanned lunar mission. On the battlefield, SUGVs can perform such tasks as transporting equipment, detecting threats, conducting search and rescue missions, repairing damaged runways, and exploring minefields. To list some examples, Packbot from iRobot, MARCbot from Exponent, MATILDA from MESA Robotics, and TALON from Foster Miller have been deployed by the US military in Afghanistan, Iraq and other battle fields. SUGVs can also help to dispose of explosive ordnance or deal with suspicious packages. The Navy's Explosive Ordnance Disposal Technology Division leads the US military's research and development in explosive ordnance disposal technology. For the nuclear industry, SUGVs can work in areas with radiation levels too high for human workers. Packbots were the first robots to enter the damaged Fukushima nuclear plant after the 2011 Tohoku earthquake and Tsunami. Another example is the *HERMIES* series of mobile robots from the Center for Engineering Systems Advanced Research (CESAR) at Oak Ridge National Laboratory (ORNL) targeting robot's application in radioactive environments. [1]

Energy storage, management, and efficient conversion are always critical issues for SUGV designs and controls. Power consumption of SUGVs is a particularly important

area of research, because these vehicles, compared to traditional automobiles, have four characteristics, as explained below.

First, SUGVs usually are smaller and lighter than automobiles, which limits their power and available energy. For military applications for example, SUGVs are frequently carried by soldiers, which limits their possible weight to around 100 pounds. To achieve small size and low weight, batteries, in most cases, are used as the power source of SUGVs. However, batteries have significantly lower power and energy densities than petroleum fuels [2]. Figure 1.1 shows a Ragone Plot of various types of batteries. It can be seen that batteries can be designed to have high power density or high energy density, but there is a trade-off between them. Figure 1.2 shows several examples of SUGVs power consumption and mission duration. From "Army Future Combat System Spin-Outs and Ground Combat Vehicle" [3], an SUGV should have an operation life time of 6-10 hours and a range of 1km when fully charged. It can be seen that there is a gap between desired power performance and today's achieved power performance. While better batteries can be a solution, other improvements such as better power consumption modeling and energy management also help to mitigate the gap.
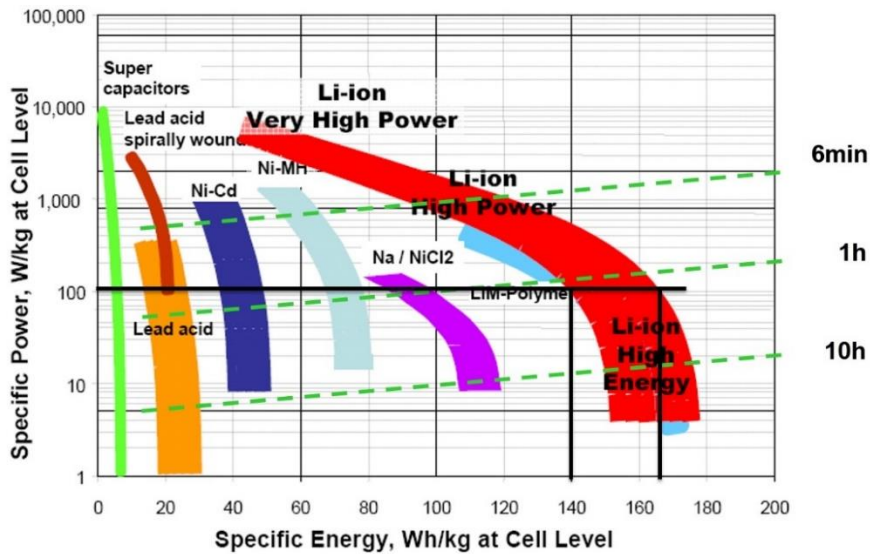
Figure 1.1 Power performance of several types of batteries [4]
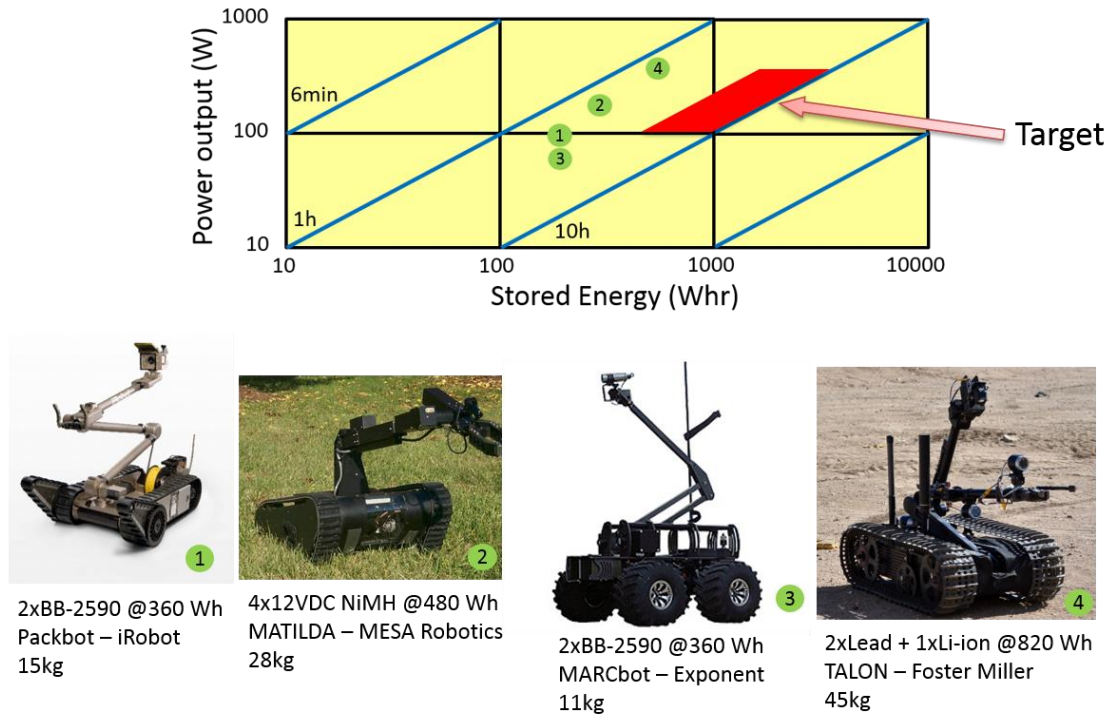
Figure 1.2 Current SUGVs' energy/power performance

Second, SUGVs operate off-road more often. Unlike paved roads, which are assumed not to deform, soils can undergo large deformation and strain. Usually paved road models assume that the tire deforms and the road does not, while most of the off-road models assume that the tire/track does not deform but the soil does. The deformation can be very significant for wheeled SUGVs. Large sinkage can cause increased power consumption and immobilization. The latter is a major concern for SUGVs. Moreover, the operating conditions for on-road situations are typically consistent and well-known, while off-road situations have many uncertainties, e.g., terrain roughness. Tire models developed for on-road operations are not suitable for SUGVs operating off-road. Thus terramechanics, which studies soil mechanics and vehicle-terrain interactions, is applied to describe off-road SUGV operations.

Third, tracks are widely used on SUGVs, because of their ability to traverse a wider range of terrains. Many current SUGVs, e.g., Packbot, TALON, and Matilda are tracked robots. However, track system can consume a great deal of power as a result of the high frictional losses arising from many sliding surfaces and track tension. For SUGVs, which

have limited power and energy, choosing between the wheel configuration and the track configuration can be a major design decision.

Forth, skid steering is widely used in SUGVs for its simplicity and robustness. As opposed to the Ackermann steering commonly used for conventional vehicles, skid steering generates yaw motions by having different rotational speeds for the left and right sides of the vehicle running gear (either tracks or wheels). Because of the unavoidable sliding between the running gear and terrain, especially for tracks, more power is consumed.

In summary, an accurate power consumption model is needed and developed in this dissertation for SUGVs. The findings will benefit both their design and control. For embedded controllers, accurate power consumption models help to generate better path planning to minimize energy consumption and to avoid immobilization. For robot designs, accurate power consumption models are instrumental for such crucial design elements as better system structure, choice of powertrain components, and selection of configuration.

1.1.2 Power consumption modeling for SUGVs

In this dissertation, we developed accurate and fast SUGV power consumption models that can estimate power consumption and energy usage for both wheeled and tracked SUGVs. In addition, we demonstrated the capability of the models using case studies, e.g., choosing between tracked and wheeled designs, and investigation of how tight turning affects power consumption. Tracked vehicles are known to have better mobility but higher losses than wheeled vehicles. The trade-off between these two performance attributes can be understood quantitatively using the developed models.

To model the propulsion power consumption of SUGV, there are 3 main approaches. The simplest approach captures only rolling resistance. In this approach, the resistance due to the running gears of the SUGVs and terrain interaction is modeled as simple coulomb friction. This model's simplicity and fast computation make it very suitable for embedded controls for work load characterization and estimation and vehicle control. The major drawback of this approach is low fidelity. As the forces acting on the contact surface between vehicle and soil come only from coulomb friction, soil deformation and its corresponding effects were not captured.

The second approach uses a large quantity of particles to simulate the running gear-soil interaction. Examples include discrete element and finite element models. The main advantage of this approach is its power in modeling dynamic and complex interactions at the contact surface. However, this approach also has two main drawbacks. One is that it requires extensive computing power, which makes it challenging for embedded control applications or design iterations. The other drawback is that these models are usually very sensitive to variations in model parameters. Since the forces and moments at the contact surface are modeled by interactions among a large number of particles, a small change in stiffness, cohesion or shear resistance parameters can propagate and result in large variances. And while it is almost always possible to tune the model parameters to fit given experiment results, its reliability in predicting/extrapolating is not always guaranteed.

The third approach includes semi-empirical models based on terramechanics. In contrast to the rolling friction model, terramechanics knowledge helps researchers to accurately model the running gear-terrain interaction, based on a large number of off-road experiments. Pressure, sinkage, shear displacement and shear stress are all considered in the modeling of the SUGV-terrain interaction. However, because of its reliance on experiments and empirical equations, it does not capture complex and dynamic interactions (e.g., terrain roughness). In this dissertation, we developed models based on the semi-empirical terramechanics.

1.2 Background

Off-road mobility and power consumption are heavily dependent upon the interaction between the running gear and the soil. While for on-road vehicles, most of the energy loss results from the viscous damping of the tires, for off-road vehicles, the soil can deform plastically, and result in absorption of a large amount of energy. The soil deformation can also result in vehicle immobility. Thus locomotion performance (mobility) and power consumption (efficiency) are two key performance metrics in the design and control of vehicles operating off-road.

1.2.1 Modeling off-road operations

The history of modeling off-road vehicles can be traced back to 400 A.D. In that early period, researchers gain experiences through experiments and failure. Even as late as World War I the development and advancement of off-road vehicles is not through an understanding of soil mechanics, but through empirical knowledge. Problems are frequently solved through trial-and-error rather than through knowledge of the actual bearing capacity of the soil [5]. This empirical approach continued until Karl Von Terzaghi introduced the concept of soil mechanics in 1920. According to Terzaghi, soil mechanics is "*the application of the laws of mechanics and hydraulics to engineering problems dealing with sediments and other unconsolidated accumulations of solid particles produced by the mechanical and chemical disintegration of rocks, regardless of whether or not they contain organic constituents*" [6]. After World War I researchers began to look at the problem of wheel/track-soil interaction, considering important phenomena such as motion resistance and sinkage [5]. And in the middle of the twentieth century, terramechanics, the study of the interactions between the vehicle and the terrain, began to be developed by a group of researchers, pioneered by Dr. M.G. Bekker and his books *Theory of Land Locomotion, Off-the-Road Locomotion*, and *Introduction to Terrain-Vehicle Systems* published in 1960, 1962 and 1969, respectively [7] [5] [8].

Modeling approaches today include purely empirical methods, computational methods, and mathematical analysis methods. Each method has its advantages and disadvantages.

Empirical methods are used because the interaction between the off-road vehicle and the terrain is complex and difficult to model accurately. Following the empirical approach, vehicles are tested in a range of terrains considered to be representative and the terrains are identified by field observations and measurements. The results of vehicle performance and terrain measurements are then empirically correlated. Empirical methods can predict performance to some extent, but often cannot explain the underlying physical phenomena. One of the best known empirical methods for predicting and evaluating off-road vehicle performance was developed in the 1960s by the US Army Corps of Engineers Waterways Experiment Station (WES), which formed the basis for the NATO Reference Mobility Model (NRMM) [9]. This method was originally intended to provide military

intelligence with a simple means to assess terrain traffic-ability and vehicle mobility on a "go/no go" basis. Although this approach has been successfully extended, for example, to predict tire performance on frictionless soils, difficulties were encountered in applying the method to the evaluation of tire performance in certain types of sand, as reported by Reece and Peca [10]. It has also been reported that the empirical approach such as Pacejka "magic formula" does not give sufficiently accurate predictions in some cases perhaps because of it lacks underlying physics [11]. Within the context of their intended purposes, well-developed empirical methods are useful in estimating the performance of vehicles under similar operating conditions. It is by no means, however, that empirical methods can extrapolate beyond the conditions upon which they are derived. Models with underlying physics have better robustness extrapolating to conditions they were not validated against. Furthermore, an entirely empirical approach is only feasible where the number of uncontrolled variables is relatively small. If a large number of variables are required, the time and cost to perform the testing can be very high. The simplicity of empirical methods makes them computationally efficient which is sometimes a deciding factor in embedded applications.

Computational models, such as Finite Element Models (FEM) and the Discrete Element Models (DEM), have been applied to Terramechanics since the 1970s. They can be used to examine vehicle-terrain interaction with complex topology, including lugged wheels/tracks traversing on rough terrains. FEM has been used to model rigid and flexible wheel-soil interaction under longitudinal and lateral slips [12] [13] [14] [15]. Newer FEM techniques such as the Coupled Eulerian-Lagrangian method are capable of modeling large deformations including those caused by grousers [16] [17].

Computational methods also have shortcomings, including the large number of parameters to be determined. In addition, a very large number of finite elements/discrete elements are typically needed. For example, it is estimated that to conduct a realistic three-dimensional simulation of full-scale vehicle-terrain interaction problem by DEM, the number of elements required would be in the order of 10^6 to 10^8 [9]. It is reported that FEM using the arbitrary Eulerian-Lagrangian formulation with 4,000 elements requires a combined CPU performance of 80 GFLOPS, while a system of 256,000 elements would require combined CPU performance of 20,398 GFLOPS [18]. While computation

capability continues to increase exponentially, current processor performance is roughly 20 GFLOPS per core. Therefore we are far away from using these models for real-time applications or for large-scale design or analysis studies [9]. In summary, the applications of FEM or DEM to the study of vehicle-terrain interaction are still in the nascent stage.

In view of the limitations of the empirical and computational methods noted above, computer-aided semi-empirical methods for the simulation or analysis of off-road vehicles have been developed. These methods combine computations with the principles of terramechanics. In the early days terrain is usually modeled as idealized elastic-plastic models (Bekker [5] [7] [8], Reese and Wong [19]). For loads which do not cause failure, classical theory of elasticity is applied: as the stress of the soil increases, the strain increases linearly. Once the stress is released, the soil returns to its original state. However response to large loads is no longer elastic or linear. The Mohr–Coulomb theory, which describes materials with much stronger compressive strength than the tensile strength, can be applied to analyze soil failure behavior. The Mohr–Coulomb theory relates the maximum shear stress of a material to the normal stress on the surface and the material's cohesion and internal shearing resistance [9]. Forces can be calculated by integrating the normal and shear stresses over the defined contact area. Janosi and Hanamoto found that the shear stress-shear displacement relationship can be represented by an exponential equation which combines the elasticity and plasticity properties together, which is later widely used in terramechanics [20]. Over time the Bekker and Wong method has been modified and expanded to add additional features, including the ability to model wheel lugs, flexible wheels, multi-pass effects, and rough terrains [21] [22] [23]. The predictive capabilities of these methods was verified by field test data obtained on various types of terrains. These methods are particularly suitable for the evaluation of competing designs, optimization of controllers, and selection of vehicle design candidates.

1.2.2 Skid steering modeling

As stated in Section 1.1, skid steering systems are commonly used for mobile robots because of its simplicity, robustness, and reliability. A skid-steer system changes vehicle heading direction by adjusting the speeds of the left and right sides. Take tracked vehicles as an example. The thrust of one track is increased and that of the other is decreased, which

creates a turning moment. Because skid steering may consume a large percentage of the vehicle propulsion power, it should be included in any accurate power analysis. However, this is challenging; the modeling of skid steering on soft soils is non-trivial because of the track/wheel-soil interaction and the distributed nature of the shear stress along the contact area.

A number of research papers have been published on the topic of skid steering on deformable terrains in steady state. Steeds conducted a detailed analysis of skid steering, which laid the foundation for subsequent studies by Weiss, Crosheck, Kitano and Jyozaki, among others [24] [25] [26] [27]. In Steed's work, the lateral shear stress is assumed to obey Coulomb's law of friction. Both isotropic and anisotropic frictions were studied. Different values of the friction coefficients were assigned to the lateral directions of the track. Coulomb's law of friction implies that the maximum shear stress between the track and the ground will develop instantly when a small relative movement is initiated. Steeds viewed the lateral resistance coefficient as constant, but the longitudinal resistance as related to shear displacement. Wong's work showed, however, that shear stress is dependent on shear displacement, and that this relationship can vary with terrain types [10]. Kar observed from experimental results that lateral resistance in skid steering maneuvers is dependent on forward velocity and turning radius, which differs from Steeds' analysis [28]. In 2001, Wong developed a modified theory of skid steering of tracked vehicles on firm ground, which relates shear displacement and shear stress both laterally and longitudinally for all contact points [29]. This model was also verified through experiments by Ehlert [30].

For SUGVs with much lower weight and smaller size than the heavy vehicles typically studied in the terramechanics literature, researchers have developed other methods to approximate skid steering behaviors at steady state. The research can be divided into two approaches. The first approach followed Bekker and Wong's theory in terramechanics but added modifications for SUGVs [31] [32] [33] [34] [35]. The core concept of this method is the modeling of the forces acting between the terrain and the wheel/track. The main strength of this approach is the fidelity and capability of the model to simulate torque and power consumption at steady state on deformable terrains. The main drawback of this approach is computation speed. With the complexity of the shear

displacement at the contact surface and the exponential equation of shear stress-shear displacement relationship, the calculation of forces on the contact surface is time consuming. In addition, because closed form solutions in many cases cannot be found, iterations are required.

Another approach focused on the online control of the vehicle, utilizing kinematic models of the vehicle motions to estimate slip ratio [36] [37] [38] [39] [40] [41]. The core idea of this method is to find the instantaneous center of rotation of the outside and inside track or wheel. Thus the motion of each point at the contact surface can be calculated. The force generated at the contact surface is viewed purely as a coulomb friction force. The strength of this approach is its simplicity and the possible onboard control applications. But it also has drawbacks. First, it is based on the assumption that all of the points on the contact surface are in plastic deformation, which is not true when the turning radius is large. Furthermore, this method does not consider the aggregation of shear displacement on the contact surface and the corresponding shear stress, and consequently the power consumption of skid steering is linear with respect to the rotational speed of the shaft, which may be an oversimplification in some cases. Moreover, longitudinal and lateral resistance coefficients in this approach are constant, which conflicts with Wong's theory that the lateral resistance coefficient varies with both turning radius and forward velocity. Another drawback of this method is that soil properties are not included in the model and only a coulomb friction coefficient is assumed, which can cause large discrepancy with test results on deformable soils.

1.3 Contributions

The focus of the dissertation is the development of vehicle-terrain interaction models for torque and power consumption estimation on deformable terrains. The models improved the analysis and simulations of SUGV mobility and energy performance, and enabled better designs of SUGVs operating on deformable terrains. The main contributions are listed below:

- Skid steering mechanism was studied and analyzed. Three widely used skid steering models on tracked vehicles (Steeds' model, Wong's model, and the ICR model)

were reviewed and compared and their strengths and weaknesses were discussed. Simulations and experiments indicated that the Wong's model is the most accurate. However, Steeds' and the ICR model are superior in computation efficiency.

- A 5 DOF skid steering model for wheeled vehicles was developed in contrast to Wong's 3 DOF skid steering model for tracked vehicles. The sinkage of the outer and inner drivetrains were considered as the two additional unknown variables. Vertical force balance and row moment balance equations were added to the vehicle dynamics. The Newton-Raphson numerical method was used to solve the steady state solutions.

- A fast computation skid steering model for tracked vehicles was developed. The fast computation model separated the computation-intensive part (track-terrain interaction) from the computation-light part (vehicle dynamics). Look-up tables for the computation-intensive part were pre-generated offline to achieve improved computation efficiency.

- A new skid steering model, the Finite Element Skid Steering (FESS) model was developed. This model combined both tracked and wheeled vehicle cases and achieved improved computation efficiency by formulating a new method to calculate the shear displacement along the discretized contact surface. Quadratic approximation of the normal shear stress at the wheel-terrain interaction surface was utilized to further improve the computation efficiency of the wheel cases. The accuracy of the FESS model was proved by experiments on dry sand.

- A 6-wheel-drive track/wheel interchangeable test robot was built for experimental validation against the FESS model. Internal resistance of the powertrain and its power consumption were measured to provide an experimental insight into the power consumption distribution among each part of the powertrain. The "pan-cake" suspension design of the test robot showed its functionality and simplicity.

- The tradeoff between track and wheel designs on SUGVs in terms of power consumption and mobility were addressed. Using the FESS model, two case studies on an imaginary Packbot with three possible designs (4-wheel, 6-wheel, and track) were conducted, and a general design comparison between tracked and wheeled SUGVs was

simulated to give an insight into the design of SUGVs and the choice between track and wheel.

1.4 Outline of the dissertation

This dissertation is organized as follows: in Chapter 2, single track/wheel-terrain interaction models on deformable terrains are reviewed and discussed. These models describe the relationship among pressure, sinkage, and compaction resistance, and that among slip ratio, shear displacement, and shear stress. These models serve as the knowledge base for vehicle-terrain interaction. In Chapter 3, the skid steering mechanism is thoroughly studied and analyzed. Three widely used skid steering models on tracked vehicles (Steeds' model, Wong's model, and the ICR model) are reviewed and compared and their strengths and weaknesses are discussed. In Chapter 4, Wong's skid steering model of tracked vehicles is extended to the wheeled vehicles and a 5 DOF skid steering model for wheeled vehicles is developed in contrast to the Wong's 3 DOF skid steering model for tracked vehicles. In Chapter 5, a fast computation skid steering model for tracked vehicles is developed, which separates the computation-intensive and computation-light part. The computation speed drastically increases with the pre-generated look-up maps of the computation-intensive part. In Chapter 6, a new skid steering model, the Finite Element Skid Steering (FESS) model that combines both tracked and wheeled vehicle cases is developed with comparable accuracy and improved computation efficiency by formulating a new method to calculate the shear displacement along the discretized contact surface. In Chapter 7, a 6-wheel-drive track/wheel interchangeable test robot is designed and built to validate the FESS model. Skid steering experiments of the test robot in 4-wheel, 6-wheel, and track configurations on dry sand are conducted. In Chapter 8, two case studies of track vs. wheel on an imaginary Packbot with three possible designs (4-wheel, 6-wheel, and track) are conducted. General design comparison between tracked and wheeled SUGVs in terms of power consumption and mobility is also conducted. Finally, in Chapter 9, the conclusion and future work are presented.

CHAPTER 2

Track/Wheel-Terrain Interaction Model

An adequate knowledge of the mechanical properties of the terrain and its response to vehicular loading is, therefore, essential to the proper development of the model between vehicle and terrain. This chapter first review the basic terramechanics concept and then describe the single track/wheel-terrain interaction model that will be used as the basis for the development of the models used in this research.

2.1 Pressure-sinkage relationship

Pressure-sinkage relationship explains the relationship between the pressure generated on the contact surface and the deformation of terrain (sinkage). The pressure-sinkage relationship may take one of the forms shown in Figure 2.1. Bekker characterized the pressure-sinkage relationship by the following equation [8].

$$P = \left(\frac{k_c}{b} + k_\phi\right) z^n \tag{2.1}$$

where p is the pressure at the wheel-soil interface, b is the dimension of the contact patch, that is, the width of a rectangular contact area, or the radius of a circular contact area, z is the sinkage, and n, k_c, and k_ϕ are soil parameters. Furthermore, n is dimensionless, while the parameters k_c and k_ϕ have variable dimensions, depending on the value of the exponent n. Table 2.1 is a list of the parameters values for some commons soils.
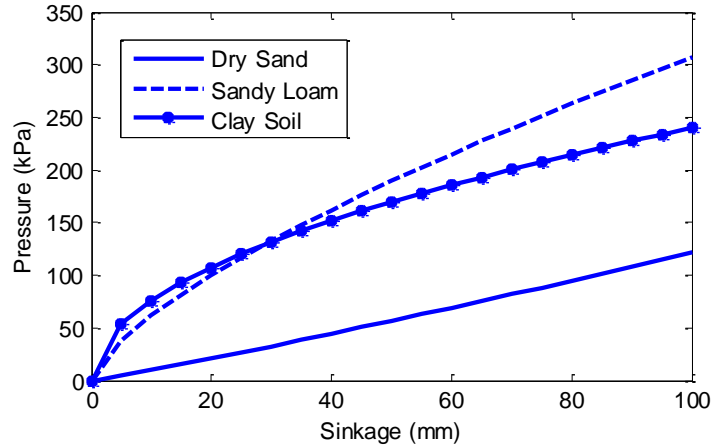
Figure 2.1 Pressure-sinkage relationship of various homogeneous terrains

Table 2.1 Terrain values (Source: [10])

Terrain	n	k_c (kN/m^{n+1})	k_ϕ (kN/m^{n+2})
Dry Sand	1.1	0.90	1523.4
Sandy Loam	0.7	5.3	1515.0
Clay Terrain	0.5	13.2	692.2

It can be seen from Figure 2.1 that parameter n dominates the shape of the pressure-sinkage relationship. When the sinkage increases, the pressure first rises fast and then slow down if n is larger than 1, while the pressure rises first slow then fast, if n is smaller than 1. Compared with dry sand, sandy loam and clay soil are harder, as the sinkage of clay soil or sandy loam is smaller than dry sand under the same load.

2.2 Shear stress-shear displacement relationship

When a torque is applied to the wheel or the sprocket of a track, shearing stress is initiated at the running gear-terrain interface, as shown in Figure 2.2.
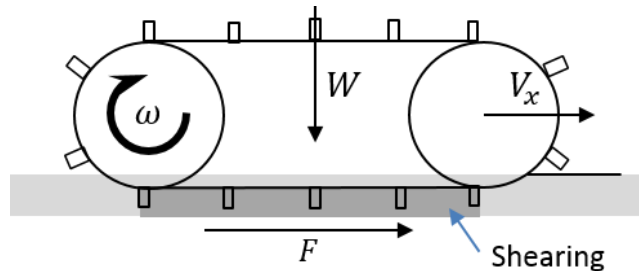
Figure 2.2 Shearing action created at a track/soil interface

14

To predict vehicle thrust as a function of slip, the shear stress-shear displacement relationship of the terrain is required. If the maximum shear stress of the terrain is plotted against the corresponding normal pressure, a straight line may be obtained, as shown in Figure 2.3 [10]. The relationship between the maximum shear stress and normal pressure is described below. The slope of the straight line determines the angle of internal shearing resistance ϕ; the intercept of the straight line with the shear stress axis determines the apparent cohesion c of the terrain; and σ represents the normal pressure. Table 2.2 lists the values of c and ϕ of three soils.

$$\tau_{max} = c + \sigma \tan \phi \tag{2.2}$$
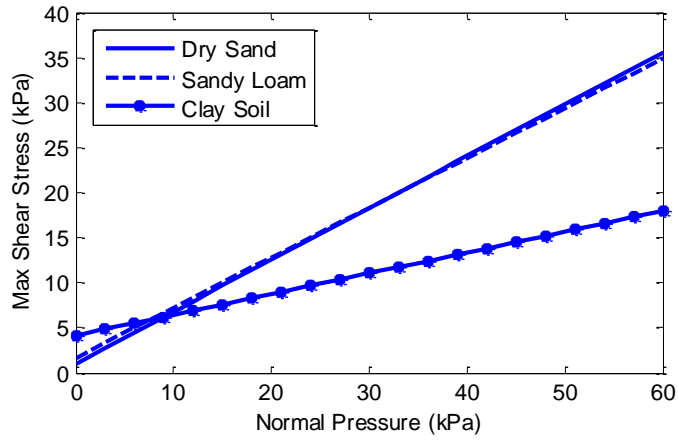
Figure 2.3 The maximum shear stress (τ_{max}) of 3 soils under various normal pressure

Table 2.2 Terrain values (Source: [10])

Terrain	c (Pa)	ϕ $(°)$
Dry Sand	1,000	30
Sandy Loam	1,700	29
Clay Terrain	4,140	13

It can be seen from Figure 2.3 that cohesion coefficient c determines the offset of the line at the Y-axis, while the internal friction angle ϕ determines the slope of the line. The larger the c value is, the more cohesive the terrain performs, while the larger the ϕ value is, the more frictional the terrain is. It should be emphasized here that τ_{max} in Eq. (2.2) is the maximum shear stress that can be generated by the terrain at a given normal

pressure. In terramechanics the actual shear stress on the contact surface is related to both normal pressure and shear displacement.

Based on a considerable amount of field data, it is found that there are three types of shear stress-shear displacement relationship commonly observed [10].

Soil Type A

For loose sand, saturated clay, dry fresh snow, and most of the disturbed soils, the shear stress-shear displacement relationship exhibits characteristics shown in Figure 2.4. The shear stress initially increases rapidly with an increase in shear displacement, and then approaches a constant value with a further increase in shear displacement. This type of relationship can be described by an exponential function proposed by Janosi and Hanamoto [20].
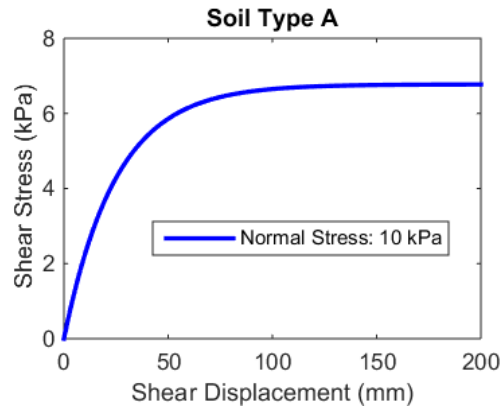
Figure 2.4 A shear curve of a simple exponential form

$$\tau = \tau_{max}\left(1 - e^{-\frac{j}{K}}\right) \tag{2.3}$$

where τ is the shear stress, τ_{max} is the maximum shear stress mentioned in Eq. (2.2), j is the shear displacement, and K is the shear deformation modulus, which is the magnitude of the shear displacement required to develop the maximum shear stress. The value K determines the shape of the shear curve and the distance between the vertical axis and the point of intersection of the straight line tangent to the shear curve at the origin.

Soil Type B

For organic terrain (muskeg) with a mat of living vegetation on the surface and saturated peat beneath it, the shear stress-shear displacement relationship exhibits characteristics shown in Figure 2.5. It can be seen that the shear stress initially increases rapidly with the increase of shear displacement, and reaches a maximum shear stress. With

a further increase of shear displacement, the shear stress continually decreases. This type of shearing behavior may be characterized by the following equation [42] [43]:

$$\tau = \tau_{max} \left(\frac{j}{K_w} \right) e^{1-\frac{j}{K_w}} \tag{2.4}$$

where K_w is the shear displacement where the maximum shear stress occurs.
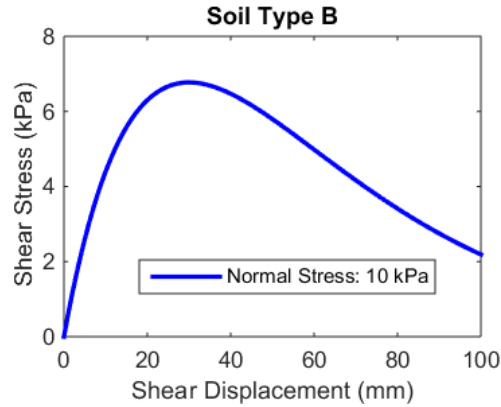
Figure 2.5 A shear curve exhibiting a peak and decreasing residual shear stress

Soil Type C

For compact sand, silt and loam, and frozen snow, they may exhibit shearing characteristics shown in Figure 2.6. It can be seen that the shear stress initially increases rapidly and reaches a maximum shear stress at a particular shear displacement. However, with a further increase in shear displacement, the shear stress decreases and approaches a constant residual value. This type of shearing behavior may be characterized by the following function [44]:

$$\tau = \tau_{max} K_r \left(1 + \left(\frac{1}{K_r(1 - e^{-1})} - 1 \right) e^{\left(-\frac{j}{K_w} \right)} \right) \left(1 - e^{\left(-\frac{j}{K_w} \right)} \right) \tag{2.5}$$

where K_r is the ratio of the residual shear stress to the maximum shear stress, and K_w is the shear displacement where the maximum shear stress occurs.

17
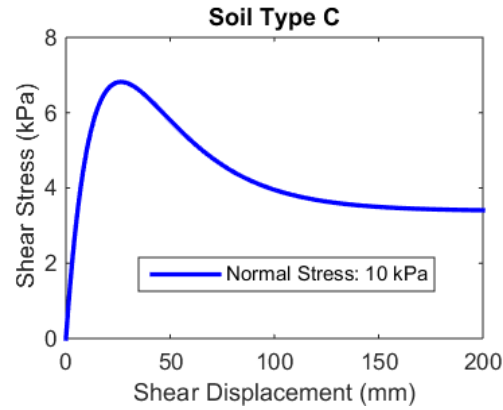
Figure 2.6 A shear curve exhibiting a peak and constant residual shear stress

In this dissertation, only type A soils are studied, since type A soils cover a vast majority of terrains for off-road driving [10] [45]. Figure 2.7 shows the shear curves of the three soils that are used in this chapter. The shear modulus parameter K of each soil is listed in Table 2.3.
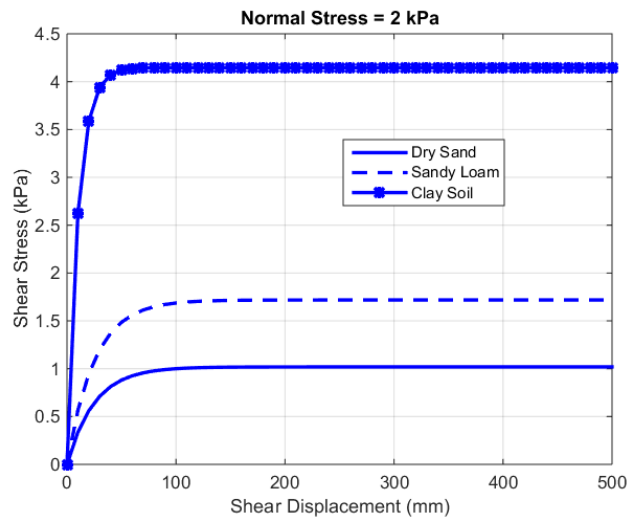
Figure 2.7 Exponential shear curve of dry sand, sandy loam, and clay soil

Table 2.3 Terrain values (Source: [10])

Terrain	K (m)
Dry Sand	0.025
Sandy Loam	0.025
Clay Terrain	0.01

18
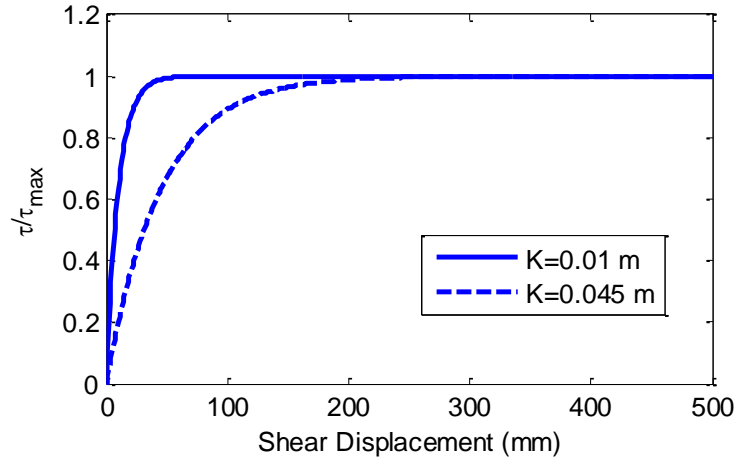
Figure 2.8 Exponential shear curves with $K = 0.01\ m$ and $K = 0.045\ m$

Figure 2.8 shows two shear curves with $K = 0.01\ m$ and $K = 0.045\ m$, respectively. When $K = 0.01\ m$, the shear stress increases more rapidly with the shear displacement and saturates at a much smaller shear displacement than the case when $K = 0.045\ m$. This indicates that for higher value of K, larger shear displacement is required to reach the maximum shear stress. The value of K thus has a considerable influence on the behavior of the shear stress.

2.3 Single track-terrain interaction model

Sections 2.1 and 2.2 explain the terramechanics concept. Models for track-terrain interaction should contain both the vertical and longitudinal equations. In steady state, the normal force from the terrain balances the gravity force and the motion resistance is equal to the tractive effort. Typically the motion resistance of a vehicle running off-road contains four parts: resistance due to vehicle-terrain interaction, ground obstacle resistance, aerodynamic resistance, and internal resistance [9]. Unlike on-road operations where the paved road is not to deform, soils are much softer and can be deformed. The vehicle-terrain interaction can be further divided into two parts: compaction resistance and bulldozing resistance. Compaction resistance comes from the running gear compacting the terrain, which bulldozing resistance comes from the running gear or the vehicle bulldozing the terrain. And bulldozing resistance is especially significant when sinkage is large [10]. However, for SUGVs with light weight and relatively large contact area, the bulldozing

19

resistance is much smaller than heavy vehicles and can be neglected. Ground obstacle resistance arises from terrain undulation. In this research, flat soil is assumed and the ground obstacle resistance is neglected. Aerodynamic resistance can be neglected for SUGVs, as they usually operate at low speed and its relatively small cross-section area makes the air drag resistance very small. Inner resistance comes from the coulomb friction and damping of the drivetrain of the vehicle. Internal resistance is not discussed in this chapter, because it depends on the design and construction of the vehicle. Internal resistance will be measured from the test robot and considered later in Chapter 7.

2.3.1 Compaction resistance

In this study, the contact area between the track and the soil is assumed to have a uniform pressure. Using the pressure-sinkage equation, typically used to characterize soft soils, the sinkage z_0 is given by

$$z_0 = \left(\frac{W/bl}{k_c/b + k_\phi} \right)^{1/n} \tag{2.6}$$

where n, k_c, k_ϕ are the terrain parameters, W is the normal load on the track, b and l are the width and length of the track-terrain contact area, respectively. The work done in compacting the terrain and creating a rut of width b, length l, and depth z_0 is given by

$$\text{Work} = bl \int_0^{z_0} \left(\frac{k_c}{b} + k_\phi \right) z^n dz = bl \left(\frac{k_c}{b} + k_\phi \right) \left(\frac{z_0^{n+1}}{n+1} \right) \tag{2.7}$$

Substituting for z_0 from Eq. (2.6) yields

$$\text{Work} = \frac{bl}{(n+1)(\frac{k_c}{b} + k_\phi)^{1/n}} \left(\frac{W}{bl} \right)^{(n+1)/n} \tag{2.8}$$

According to Wong if a track is pulled a distance l in the horizontal direction, the work done by the towing force, which is equal to the magnitude of the motion resistance due to terrain compaction R_c, can be equated to the vertical work done in making a rut of length l, as expressed by Eq. (2.9) [10].

$$R_c l = \frac{bl}{(n+1)(\frac{k_c}{b} + k_\phi)^{1/n}} \left(\frac{W}{bl} \right)^{(n+1)/n} \tag{2.9}$$

Therefore

$$R_c = \frac{b}{(n+1)(\frac{k_c}{b} + k_\phi)^{1/n}} \left(\frac{W}{bl}\right)^{(n+1)/n} \tag{2.10}$$

Eq. (2.10) is used to calculate the motion resistance due to terrain compaction of a track with uniform pressure distribution, based on the pressure-sinkage relationship.

2.3.2 Tractive effort and slip of a track

The tractive effort of a track is produced by the shear displacement of the terrain, as shown in Figure 2.2. The maximum tractive effort F_{max} that can be developed by a track is determined by the shear strength of the terrain τ_{max} and the contact area A, assuming a uniform pressure on the contact surface:

$$F_{max} = A\tau_{max} = Ac + W \tan \phi \tag{2.11}$$

where A is the contact area of the track, W is the normal load, and c and ϕ are the cohesion and the angle of internal shearing resistance of the terrain, respectively. Experimental data show that the cohesion c of frictional terrain, such as dry sand, is small; the maximum tractive effort, therefore, depends mostly on the vehicle weight. The dimensions of the track has relatively small effect on the maximum tractive effort. On cohesive terrains, such as saturated clay, the value of ϕ is small. And the maximum tractive effort primarily depends on the contact area of the track. The dimensions of the track are crucial in this case.

It should be mentioned that if the normal load is not uniformly distributed on the contact surface, then the maximum tractive effort F_{max} is the integration of τ_{max} over the contact area.

$$F_{max} = \iint (c + \sigma \tan \phi) dA \tag{2.12}$$

In vehicle performance evaluation, however, it is desirable to determine the variation of thrust with track slip ratio over the full operating range. To predict the relationship between thrust and slip ratio, it is necessary to examine the development of shear displacement beneath a track since shear stress is a function of shear displacement. The shear displacement is the aggregation of relative shear velocity over time. The slip ratio can be defined as

$$s = \begin{cases} \dfrac{r\omega - V_x}{r\omega} & driving \\ \dfrac{r\omega - V_x}{V_x} & braking \end{cases} \qquad (2.13)$$

where r is the sprocket radius, ω is the sprocket angular velocity, and V_x is the longitudinal velocity. The range of the slip ratio is $[-1,1]$.

The shear velocity V_j in straight-running situations can be described as

$$V_j = r\omega - V_x \qquad (2.14)$$

It should be noted that when the vehicle is driving, V_j will be in the direction opposite to vehicle motion. When the vehicle is braking, V_j will be in the direction same as vehicle motion. Since the track is assumed to be not stretchable, the shear velocity V_j remains the same for every contact point with terrain. The shear displacement j of a point located at a distance x from the front of the contact area can then be calculated as

$$j = V_j t = (r\omega - V_x)\frac{x}{r\omega} = \begin{cases} sx & driving \\ \dfrac{s}{1+s}x & braking \end{cases} \qquad (2.15)$$

Eq. (2.15) explains the relationship between the shear displacement beneath a flat track and the slip ratio in both straight-line driving and braking cases. With the shear stress-shear displacement relationship (Eq. (2.3)), the total tractive effort of a track can be calculated by integrating the shear stress over the contact area.

$$F = sign(s) \iint \tau dA = sign(s) \iint (c + \sigma \tan\phi)(1 - e^{-|j|/K}) dA \qquad (2.16)$$

Assuming a uniform normal pressure $\sigma = W/bl$, we can then get a closed form expression for the tractive effort F.

$$F = \begin{cases} (Ac + W\tan\phi)\left[1 - \dfrac{K}{sl}\left(1 - e^{-\frac{sl}{K}}\right)\right] & driving \\ -(Ac + W\tan\phi)\left[1 - \dfrac{K(s+1)}{sl}\left(e^{\frac{sl}{K(1+s)}} - 1\right)\right] & braking \end{cases} \qquad (2.17)$$

Eq. (2.17) shows the functional relationship among tractive effort, vehicle parameters, terrain values, and track slip ratio. The first part of the equation $Ac + W\tan\phi$ is the maximum shear force that can be generated on the contact surface with a uniform load W. The part inside the square bracket is the integration of $1 - e^{-|j|/K}$ under driving and braking cases, which indicates to what extent the maximum shear force can be achieved.

22

2.3.3 Simulations of the track-terrain interaction model

In the previous sections, vertical (pressure-sinkage) and longitudinal (shear stress-shear displacement) relationships are explained and the corresponding forces on the contact surface are derived. In this section the track-terrain interaction will be modeled. In steady state we have

$$\begin{cases} F_s - R_c = F_d \\ F_z = W \end{cases} \tag{2.18}$$

where F_s is the shear force, R_c is the compaction resistance, F_d is the drawbar pull, F_z is normal force from terrain and W is the vehicle weight. We have two unknowns that are slip ratio and sinkage. And we have two equations. So the problem can be solved theoretically. It should be noted here that Eq. (2.6) and Eq. (2.10) do not include slip ratio and Eq. (2.17) does not include sinkage. So Eq. (2.18) can be solved separately for sinkage and slip ratio.

Figure 2.9 shows the sinkage and compaction resistance of a track under various normal load on dry sand, sandy loam and clay terrain. Terrain parameters are shown in Table 2.1 and Table 2.2. The track parameters are: width 0.07m, length 0.7m (based on the Packbot, an SUGV made by iRobot Co.).
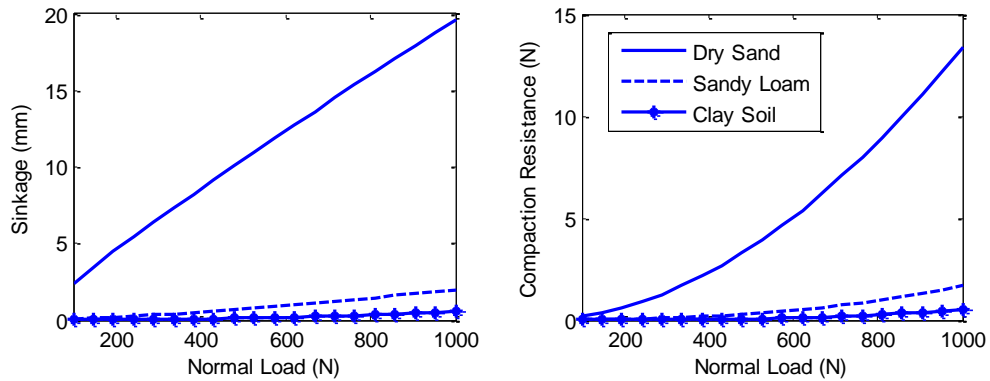
Figure 2.9 The sinkage and compaction resistance of a track on 3 types of soils

It can be seen from Figure 2.9 that on soft terrain (dry sand), the sinkage is from 3mm to 20mm with normal load from 100N to 1000N and the corresponding compaction resistance is from less than 1N to 13N, while on medium-hard terrain (sandy loam and clay soil), the sinkage and the compaction resistance are much smaller and the sensitive to normal load is also lower.

Figure 2.10 shows the drawbar pull of a track with various slip ratio on the same three types of soils. K values are 0.025m, 0.025m, and 0.01m for dry sand, sandy loam and clay soil, respectively (Source: [45]). Track parameters are the same as those used in Figure 2.9. The normal load is set as 100 N. (The Packbot weighs from 15.8kg to 28.31kg, depending on the accessories. Source: [46])
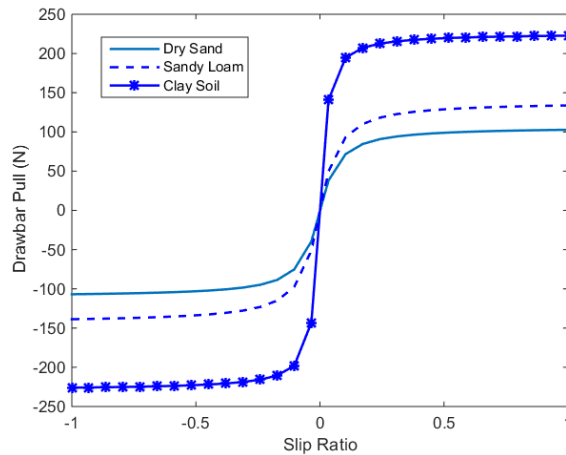
Figure 2.10 Drawbar pull of a track vs. slip ratio on 3 types of soils

It can be seen from the graph that terrain properties affect the drawbar pull of a track. Because of the large contact area of the track, drawbar pull increases rapidly with the slip ratio. On all 3 types of soils, drawbar pull saturates at about 20% slip.

It should be emphasized here that all of Bekker and Wong's equations are measured and deduced for steady state conditions. And the instantaneous terrain response to vehicle load is not considered.

2.4 Wheel-terrain interaction model

In the modeling of wheel-terrain interaction, sinkage and the distribution of normal and shear stresses on the contact surface should be considered. Wong and Reece developed a single wheel-terrain interaction model on straight-running situations [19]. In this model, the wheel thrust or tractive effort and resistance forces are found by integrating the shear stress (τ) and normal stress (σ) along the interface, as illustrated in Figure 2.11.

The slip ratio is defined in the same way as the track model in Eq. (2.13). The only difference is that ω is the wheel angular velocity.

As shown in Figure 2.11, z represents the wheel sinkage relative to the uncompact terrain in front of the wheel. From simple geometric relationship we have

$$\theta_f = \cos^{-1}(1 - z/r) \tag{2.19}$$

where θ_f is the entry contact angle. The exit contact angle θ_r can be calculated in the following form

$$\theta_r = (b_0 + b_1 s)\theta_f \tag{2.20}$$

where b_0 and b_1 are terrain-dependent empirical parameters [19].
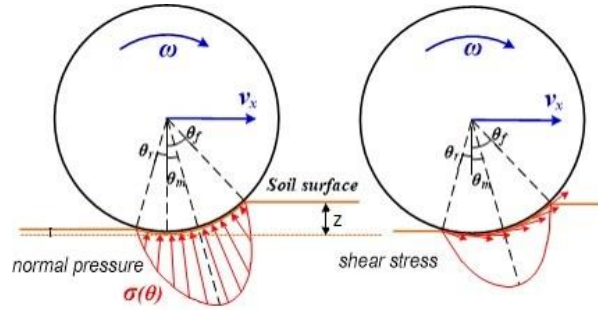
Figure 2.11 Wheel-Terrain interaction geometry

2.4.1 Normal stress distribution

Given the geometry and the contact surface, Wong and Reece calculated stress distributions along the wheel-terrain interface. The normal pressure can be presented as

$$\sigma(\theta) = \begin{cases} r^n \left(\dfrac{k_c}{b} + k_\phi\right) [\cos\theta - \cos\theta_f]^n & (\theta_m \le \theta \le \theta_f) \\ r^n \left(\dfrac{k_c}{b} + k_\phi\right) [\cos\theta_e - \cos\theta_f]^n & (\theta_r \le \theta \le \theta_m) \end{cases} \tag{2.21}$$

with

$$\begin{cases} \theta_e = \theta_f - (\theta - \theta_r)(\theta_f - \theta_m)/(\theta_m - \theta_r) \\ \theta_m = (a_0 + a_1 s)\theta_f \\ \theta_r = (b_0 + b_1 s)\theta_f \end{cases} \tag{2.22}$$

where θ_e is the equivalent front region contact angle for points in the rear contact region, θ_m is the angle corresponding to the maximum normal stress, and a_0, a_1, b_0, b_1 are empirical parameters. In this study these empirical parameters are listed below.

Table 2.4 Terrain values (Source: [19])

Terrain	a_0	a_1	b_0	b_1
Dry Sand	0.24	0.32	-0.45	0

25

2.4.2 Shear stress distribution

The shear velocity v_j on the contact surface with regard to a contact angle of θ can be expressed as

$$v_j(\theta) = r\omega - v\cos\theta = \begin{cases} r\omega[1 - (1 - s)\cos\theta] & driving \\ r\omega[1 - \dfrac{1}{1 + s}\cos\theta] & braking \end{cases} \tag{2.23}$$

The corresponding shear displacement can be calculated following the same way used in the track model.

$$j(\theta) = \int_0^t v_j(\theta)dt = \int_\theta^{\theta_f} v_j(\theta)\frac{d\theta}{\omega} \tag{2.24}$$

$$j(\theta) = \begin{cases} r[(\theta_f - \theta) - (1 - s)(\sin\theta_f - \sin\theta)] & driving \\ r[(\theta_f - \theta) - \dfrac{1}{(1 + s)}(\sin\theta_f - \sin\theta)] & braking \end{cases} \tag{2.25}$$

The same as the results for the track model, the magnitude of the shear stress is expressed by the formula given by Janosi and Hanamoto

$$\tau(\theta) = sign(s)(c + \sigma(\theta)\tan\phi)(1 - e^{(-|j(\theta)|/K)}) \tag{2.26}$$

where c is the cohesion, ϕ is the internal friction angle of the terrain, and K is the shear modulus of the terrain.

2.4.3 Simulations of the wheel-terrain interaction model

The above two sections discussed the calculation of the normal stress and the shear stress on the contact surface between the wheel and terrain. We can determine the forces exerted on the wheel by integrating the corresponding stresses along the wheel-terrain contact area. The longitudinal and vertical forces can be formulated as

$$\begin{cases} F_x = rb\displaystyle\int_{\theta_r}^{\theta_f}(-\sigma(\theta)\sin\theta + \tau(\theta)\cos\theta)d\theta \\ F_z = rb\displaystyle\int_{\theta_r}^{\theta_f}(\sigma(\theta)\cos\theta + \tau(\theta)\sin\theta)d\theta \end{cases} \tag{2.27}$$

where F_x, F_z are the longitudinal and vertical forces exerted on the wheel. We have two unknown variables (sinkage and slip ratio). Similar to the track model, in steady state, there are two force balance equations which are longitudinal and vertical force balance, shown

in Eq. (2.28). In the wheel model, compaction resistance is inherently included in the calculation of F_x.

$$\begin{cases} F_x = F_d \\ F_z = W \end{cases} \tag{2.28}$$

where W is the wheel load and F_d is the drawbar pull. So we have two unknowns and two equations. The model can be solved theoretically.

Compared to the track model, the wheel model is more complicated in two aspects. One is that the calculation of normal stress distribution on the wheel-terrain interaction surface is non-trivial which makes the calculation of shear stress also non-trivial. The other aspect is that the slip ratio and sinkage can affect the entry and exit contact angles, which changes the area of the contact surface, in turn changing the longitudinal and vertical forces. For a given load and drawbar pull, the slip ratio and sinkage in steady state should be solved simultaneously. Due to the two aspects mentioned above, closed form solutions of sinkage and slip ratio are not available unless further simplification assumptions are made. Researchers have developed simplified models to approximate the solution. For example, Iagnemma and Jia used linear and 2nd order polynomial equations to approximate the normal and shear stresses on the contact surface [45] [47]. Smith used pre-calculated look-up tables to accelerate the calculation [48].

In this study we developed a numerical method, Newton-Raphson method, to solve the equation set. A solution vector $x = [z, s]'$ is generated, where z is sinkage and s is slip ratio. And we rewrite Eq. (2.28):

$$F(x) = \begin{bmatrix} F_x - F_d \\ F_z - W \end{bmatrix} = 0 \tag{2.29}$$

The Newton-Raphson method then be used based on the following formulation:

$$x_{k+1} = x_k - \frac{F(x_k)}{F'(x_k)} \tag{2.30}$$

To initialize this iterative solution process, a set of good starting value x_0 should be given. We use

$$x_0 = [z_0 \quad 0.2]' \tag{2.31}$$

where z_0 is the initial guess of the sinkage and initial slip ratio is 20%. The calculation of z_0 is based on Bekker's empirical equation of wheel load-sinkage relationship expressed below [8].

$$z_0 = \left[\frac{3W}{b(3-n)\left(\frac{k_c}{b} + k_\phi\right)\sqrt{2r}} \right]^{\left(\frac{2}{2n+1}\right)} \tag{2.32}$$

The numerical method for approximating $F'(x_k)$ is shown in the following.

$$F'(x_k) \approx \begin{pmatrix} \dfrac{\Delta F_1}{\Delta z} & \dfrac{\Delta F_1}{\Delta s} \\ \dfrac{\Delta F_2}{\Delta z} & \dfrac{\Delta F_2}{\Delta s} \end{pmatrix} \tag{2.33}$$

The iteration stops when the absolute value of each equation in eq. (2.29) is less than 0.001 N. When the sinkage and slip ratio are solved we can further calculate the torque on the wheel shaft by this equation:

$$M_y = -r^2 b \int_{\theta_r}^{\theta_f} \tau(\theta)d\theta \tag{2.34}$$

Figure 2.12 shows the solutions of sinkage and slip ratio of the wheel with various loads on 3 different types of soils. We use the same terrain parameter values as in the track model shown in Table 2.1 and Table 2.2. K values are 0.025m, 0.025m, and 0.01m for dry sand, sandy loam, and clay soil respectively. We set the wheel width at 0.07m, and wheel radius at 0.1m, the same as the track simulation results reported in the previous section.
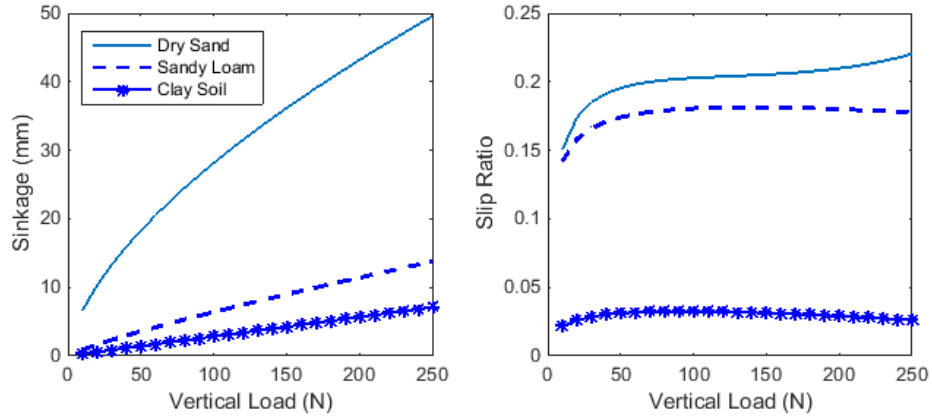
Figure 2.12 The sinkage of the wheel under various loads and slip ratio on 3 types of soils

It can be seen from Figure 2.12 that on dry sand (soft and frictional) the sinkage is much larger than on sandy loam (hard and frictional) or clay soil (hard and cohesive). The slip ratio on dry sand is also much larger. For example, when the vertical load is 150 N, the sinkage on dry sand is almost 9 times larger than on clay soil. Moreover, the slip ratio

on dry sand, is 7 times larger than on clay soil. Although sinkage always increases with the vertical load, yet slip ratio can increase or decrease with the vertical load.

Figure 2.13 shows the drawbar pull performance and the torque exerted on the wheel shaft (vertical load remains 100 N). A constant vehicle forward velocity 0.5m/s is assumed.
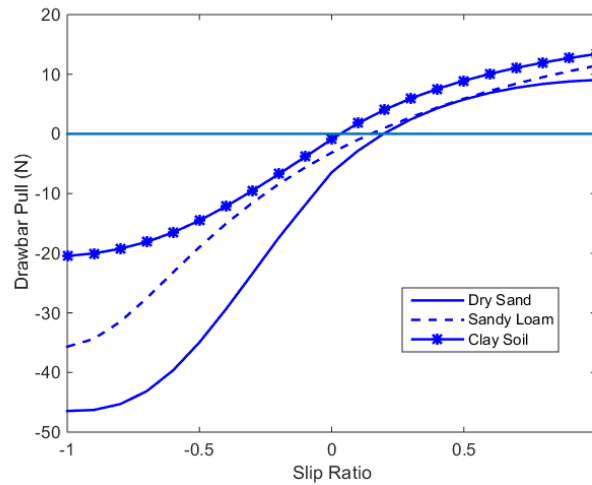
Figure 2.13 Drawbar pull and the torque exerted on the wheel shaft

It can be seen from Figure 2.13 that the drawbar pull is different from the track model shown in Figure 2.10 (the track model shows near symmetric performance of drawbar pull in positive and negative slip ratio areas). For example, the maximum drawbar pull of the wheel simulated on dry sand is 9.05N, when the slip ratio is 1. And the minimum drawbar pull is -46.45N, when the slip ratio is -1. The range of drawbar pull for the wheel on sandy loam and clay soil are $[-35.67,11.42]N$ and $[-20.46,13.39]N$ respectively. And in order to achieve a positive drawbar pull, the slip ratio required is 0.19, 0.15, and 0.04, respectively for dry sand, sandy loam, and clay soil. The main reason is that the wheel contact surface is not symmetric with respect to the wheel contact angle θ. And the front entry angle is always larger than the exit angle, which indicates that a bulldozing force always exits. When the slip ratio is negative, the entry angle becomes larger while the exit angle is smaller, which increases the bulldozing effect. The bulldozing effect of the wheel contribute negatively to its mobility compared to a track design.

2.5 Comparisons between track and wheel

More comparisons between track-terrain interaction and wheel-terrain interaction are shown in Figure 2.14 and Figure 2.15 on 3 different types of soils. As driving case (positive slip ratio) is more important in power consumption modeling, Figure 2.14 and Figure 2.15 only include driving cases. The track and wheel parameters are listed in Table 2.5.
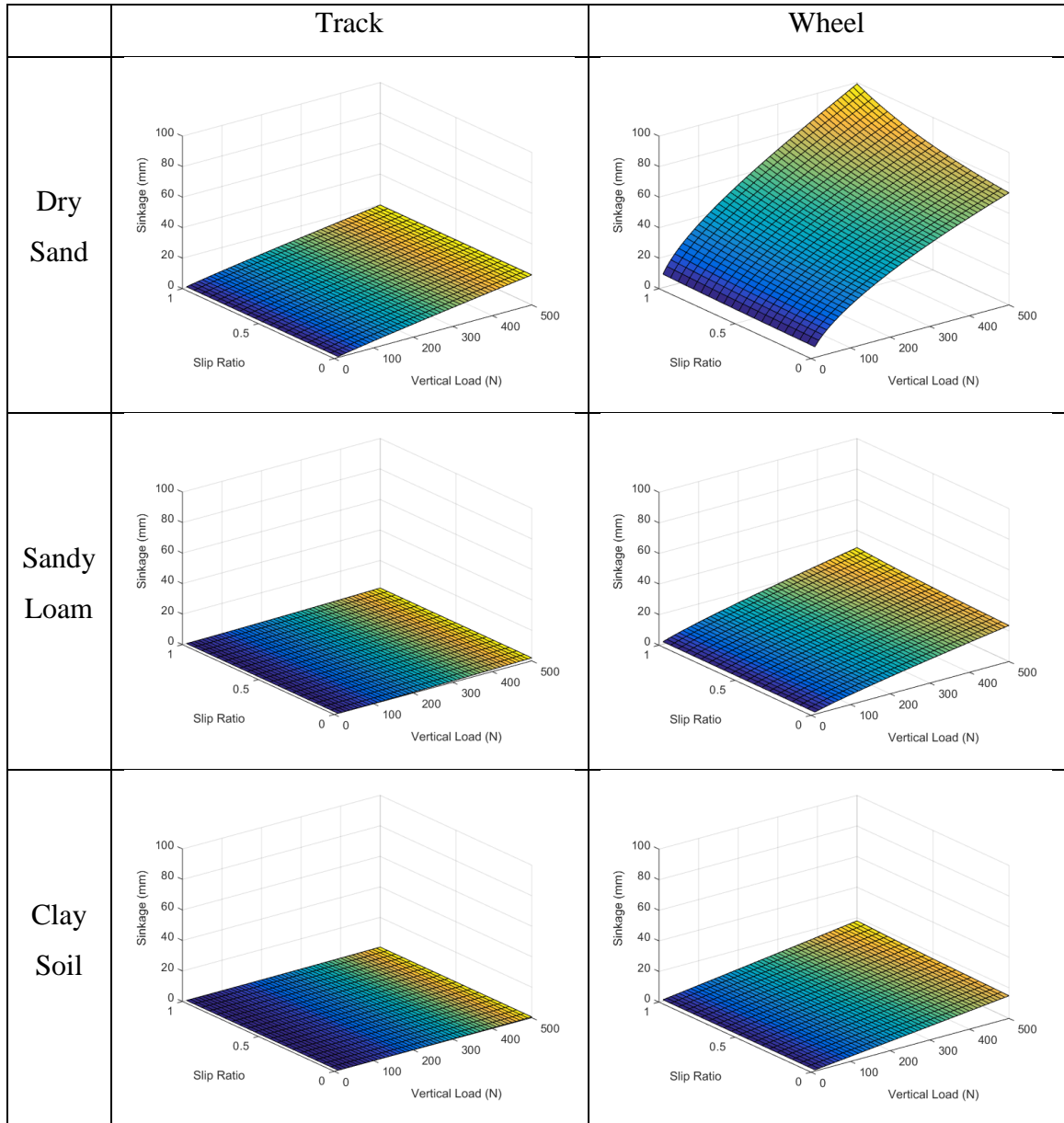
Figure 2.14 Sinkage comparison between wheel-terrain and track-terrain interaction
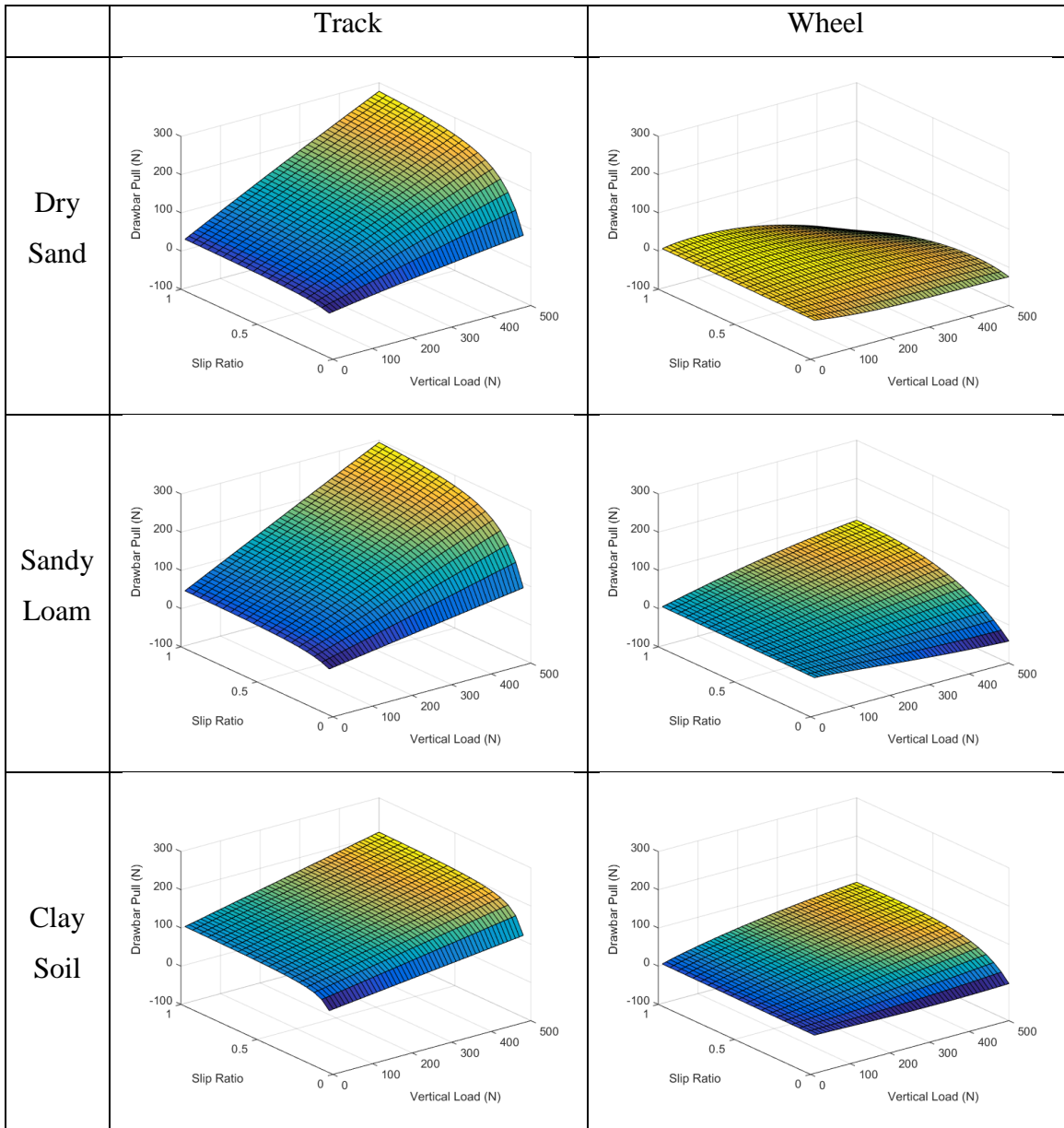
Figure 2.15 Drawbar pull comparison between wheel-terrain and track-terrain interaction

Table 2.5 Track and wheel parameters

Track	
Track Length (m)	0.35
Track Width (m)	0.07
Sprocket Radius (m)	0.1
Wheel	
Wheel Width (m)	0.07
Wheel Radius (m)	0.1

The track configuration always shows a larger drawbar pull and a smaller sinkage over the wheel configuration, meaning better mobility performance. The drawbar pull ability of the track increases with the vertical load, while the drawbar pull ability of the wheel may decrease, depending on the type of terrain and slip ratio. On dry sand, the drawbar pull of the wheel is sensitive to the vertical load. Large vertical load will result in large sinkage and drawbar pull can become negative at large slip ratio. On hard terrain, such as sandy loam and clay, the sinkage of wheel is much smaller than that on dry sand. A positive drawbar pull can be achieved with large enough slip ratio by the wheel on sandy loam and clay soil. It also can be seen in Figure 2.14 that slip ratio of the wheel model can affect sinkage (especially on dry sand), because slip ratio will change the contact surface area (entry angle θ_f and exit angle θ_r) and the position of the maximum shear and normal stress (θ_m) on the contact surface, resulting in different shear and normal stress. For the track model slip ratio does not have a significant relationship with sinkage due to the assumption that the track model has a flat contact surface and therefore the sinkage is largely related to the vertical load. The flat and larger contact surface of the track also contributes to the larger drawbar pull than the wheel. This is partially because the direction of the shear stress is parallel to the drawbar pull, while there is a contact angle θ between the direction of shear stress and the drawbar pull in the wheel configuration. In summary, track is superior to wheel in terms of drawbar pull, thus has better mobility (acceleration, gradability). Its main drawback is lower efficiency, (larger resistances between tracks and sprockets), which will be demonstrated later in this research.

2.6 Summary

In this chapter, basic elements of terramechanics, including pressure-sinkage relationship and shear stress-shear displacement relationship were discussed. A track-terrain interaction model and a wheel-terrain interaction model were developed. Sinkage and slip ratio are decoupled in the track-terrain interaction model and closed form solutions for the traction forces on the contact surface and torque on the sprocket were found. The wheel-terrain interaction model is more complicated as sinkage and slip ratio are coupled due to the circular contact surface. The Newton-Raphson numerical method was applied to

solve the model in steady state. Comparisons of sinkage and drawbar pull between the track model and the wheel model were shown with regard to various vertical load and slip ratio. These two models served as the basis to model skid steering for both tracked and wheeled SUGVs running off-road in the following chapters.

CHAPTER 3
Skid Steering Models for Tracked SUGVs

In this chapter, three widely used skid steering models (Steeds' Model, Wong's Model, and the Instantaneous Center of Rotation (ICR) Model) for tracked vehicles were reviewed. Their assumptions and features were analyzed. Simulation results of the three models on a tracked SUGV were compared. Finally, conclusions were drawn regarding the advantages and drawbacks of these three models.

3.1 Skid steering

The principle of skid steering is that the thrust of one side of the driveline is increased and that of the other is either held constant or reduced. A turning moment is then generated. Since the moment of turning resistance is large when the turning radius is small, significantly more power is consumed in a turn than in a straight line motion. Furthermore, braking of the inside track or wheels may be required to make a turn, which reduces the maximum forward thrust that the vehicle can develop. Because of all of these unique features and characteristics, skid steering distinguishes itself from the Ackermann steering system on traditional on-road passenger cars.

Take the tracked vehicle in the skid steering maneuver, shown in Figure 3.1, as an example. L_o and L_i are the vertical loads on the outside and inside track. F_o and F_i are the thrusts of the outside and inside tracks. R_o and R_i are the resistances on the outside and inside tracks. $\dot{\phi}$ is the yaw rate, v is the forward velocity of the vehicle, and R is the turning radius. The vehicle has track length l, track width b, tread of the vehicle B, CG height h, and mass m.
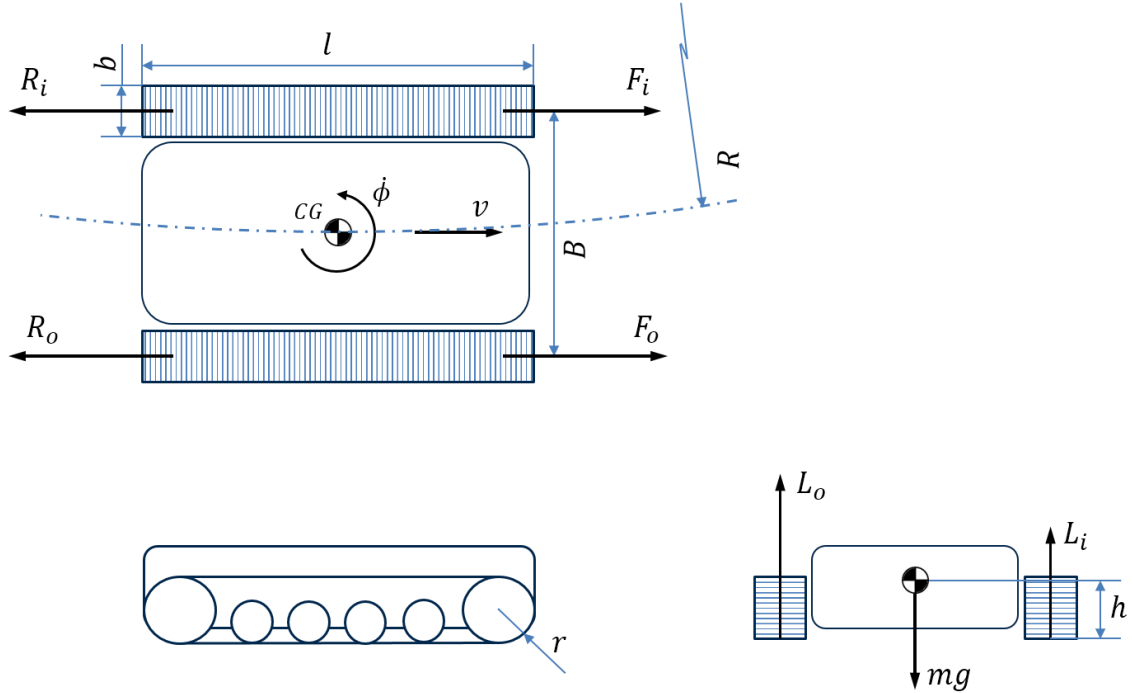
Figure 3.1 A tracked vehicle in a skid steering maneuver (F_o should be larger than F_i)

If we treat the tracked vehicle as a rigid body, there are 6 degrees of freedom: longitudinal, lateral and vertical translational motions and roll, pitch and yaw rotational motions. In the dynamic analysis of skid steering, pitching rotation can be neglected assuming that the accelerating and breaking rate of a vehicle is small. Therefore, 5 degrees of freedom (5DOF) dynamic equations are widely used.

Among the three models for tracked vehicles, rolling and vertical dynamic equations can be solved separately. In the vertical direction, the sum of the loads on the outside and inside tracks is equal to the vehicle weight. The load on the outside and inside tracks can be calculated from the following equations, assuming CG is at the geometric center of the vehicle.

$$\begin{cases} L_o + L_i = mg \\ \dfrac{(L_o - L_i)B}{2} = \dfrac{mv^2}{R}h \end{cases} \rightarrow \begin{cases} L_o = \dfrac{mg}{2} + \dfrac{mv^2}{RB}h \\ L_i = \dfrac{mg}{2} - \dfrac{mv^2}{RB}h \end{cases} \tag{3.1}$$

Consequently, the dynamic analysis of skid steering becomes the analysis of force balance in the longitudinal and lateral directions and moment balance in the yaw direction.

35

3.2 Steeds' skid steering model

In the longitudinal direction, the calculation of motion resistance in Steeds' model on the outside and inside tracks (R_o and R_i) due to the compaction of soil follows the pressure-sinkage relationship and the corresponding equations developed in Chapter 2.

$$\begin{cases} R_o = \dfrac{b}{(n+1)(\frac{k_c}{b}+k_\phi)^{1/n}}\left(\dfrac{L_o}{bl}\right)^{(n+1)/n} \\[4mm] R_i = \dfrac{b}{(n+1)(\frac{k_c}{b}+k_\phi)^{1/n}}\left(\dfrac{L_i}{bl}\right)^{(n+1)/n} \end{cases} \tag{3.2}$$

In the lateral direction, a constant coefficient of lateral resistance μ_t over various surfaces is assumed. The values of μ_t is given in Table 3.1.

Table 3.1 Values of μ_t (Source: [10])

Track Material	Coefficient of Lateral Resistance μ_t		
	Concrete	Unpaved Hard Ground	Grass
Steel	0.50-0.51	0.55-0.58	0.87-1.11
Rubber	0.90-0.91	0.65-0.66	0.67-1.14

In Steeds' model the lateral resistance on the outside and inside tracks is assumed to be distributed uniformly, as can be seen in Figure 3.2. Therefore, the lateral resistance dR_l on a segment of the track is

$$dR_l = \frac{\mu_t W}{l}\,dx \tag{3.3}$$

where dx is the segment length.

The dynamics under skid steering in the steady state are described by

$$\begin{cases} \sum F_x = 0, \ \ F_o + F_i = R_o + R_i + \dfrac{mv^2}{R}\sin\beta \\[3mm] \sum F_y = 0, \ \ R_{lo} + R_{li} = \dfrac{mv^2}{R}\cos\beta \\[3mm] \sum M_z = 0, \ \ \dfrac{(F_o - F_i)B}{2} - \dfrac{(R_o - R_i)B}{2} + \dfrac{mv^2}{R}\cos\beta\, s_0 = M_{ro} + M_{ri} \end{cases} \tag{3.4}$$
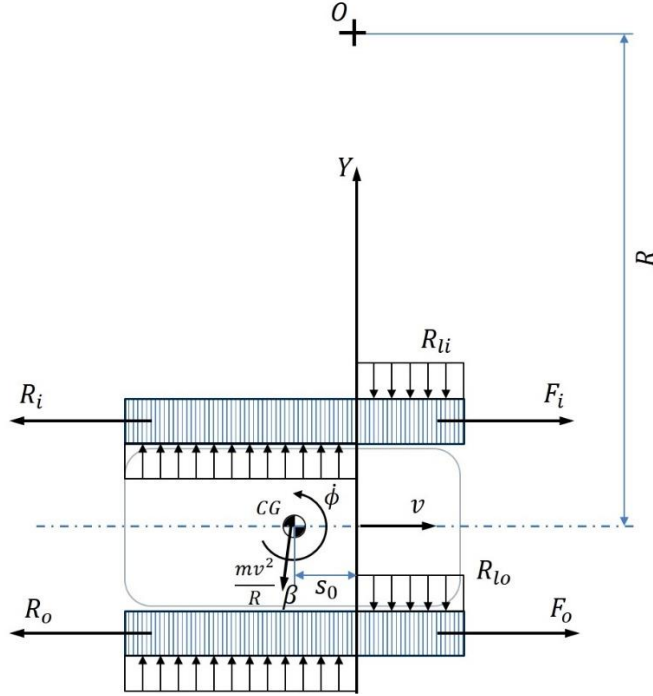
Figure 3.2 Forces acting on a tracked vehicle during a turn in Steeds' model

In Eq. (3.4), R_o and R_i can be calculated from the track-terrain interaction model developed in Chapter 2. Lateral resistances R_{lo} and R_{li} can be calculated using Eq. (3.3):

$$R_{lo} = 2\frac{\mu_t L_o}{l} s_0$$

$$R_{li} = 2\frac{\mu_t L_i}{l} s_0$$

(3.5)

It can be seen from Eq. (3.4) that the lateral resistance acting on the track by the ground must be equal to the centrifugal force, as shown in Figure 3.2. Assuming that the normal pressure distribution along the track is uniform, and that the coefficient of lateral resistance μ_t is a constant, the center of rotation must lie at a distance s_0 in front of the center of gravity in order to satisfy the equilibrium condition in the lateral direction. The corresponding moment caused by lateral resistance is calculated as

$$M_{ro} = \frac{\mu_t L_o}{l}\left[\int_0^{\frac{l}{2}+s_0} x dx + \int_0^{-\frac{l}{2}+s_0} x dx\right] = \frac{\mu_t L_o}{2l}\left(\frac{l^2}{2} + 2s_0^2\right)$$

(3.6)

$$M_{ri} = \frac{\mu_t L_i}{l}\left[\int_0^{\frac{l}{2}+s_0} x dx + \int_0^{-\frac{l}{2}+s_0} x dx\right] = \frac{\mu_t L_i}{2l}\left(\frac{l^2}{2} + 2s_0^2\right)$$

37

There are three unknowns F_o, F_i and s_0 which can be solved separately from Eq. (3.4) by using Eqs. (3.2), (3.5) and (3.6). Assuming a small side slip angle β, the three unknowns are solved.

$$s_0 = \frac{v^2 l}{2R\mu_t g}$$

$$F_o = R_o + \frac{M_{ro} + M_{ri} - \frac{mv^2}{R} s_0}{B} \tag{3.7}$$

$$F_i = R_i - \frac{M_{ro} + M_{ri} - \frac{mv^2}{R} s_0}{B}$$

The torques on the sprocket (T_o and T_i) can then be calculated from the thrust forces (F_o and F_i) and the sprocket radius r.

Plots of s_0, T_o and T_i are shown in Figure 3.3 using the simulation parameters shown in Table 3.2.
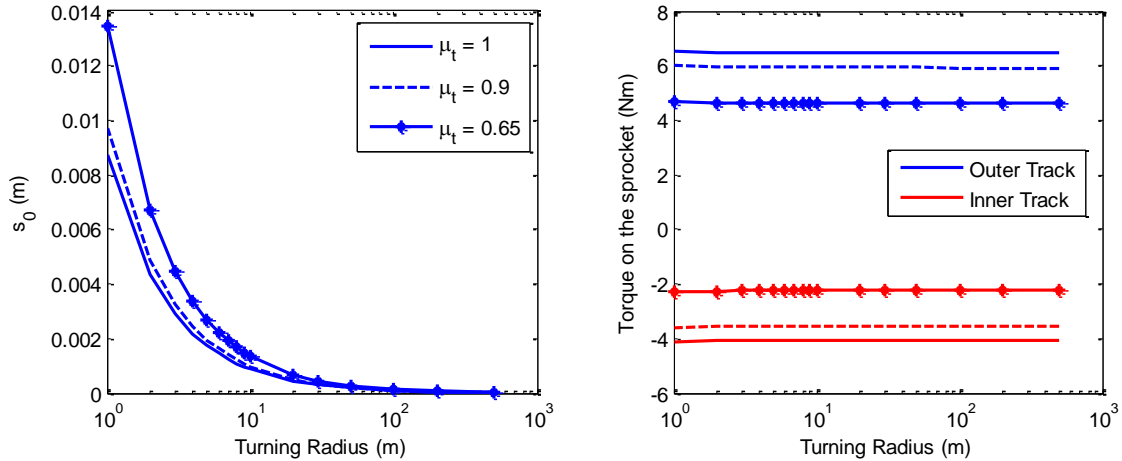
Figure 3.3 Plots of s_0 and sprocket torque from the Steeds' model

Table 3.2 Vehicle parameter values used in the simulations

Vehicle Parameters	
Mass (kg)	30
Track Length (m)	0.7
Track Width (m)	0.07
Tread of the Vehicle (m)	0.4
Sprocket Radius (m)	0.1
CG Height (m)	0.15
Simulation Case	
Forward Velocity (m/s)	0.5

Figure 3.3 illustrates the offset of the turning center s_0 and the torque on the sprocket of the outside and inside tracks versus the turning radius under different μ_t. It can be seen that s_0 increases as the turning radius decreases. This is mainly because a larger offset of turning center can create larger lateral force to overcome the effect of the larger centrifugal force. Moreover, it can be seen on the right hand side of Figure 3.3 that larger μ_t requires larger sprocket torques. However, their magnitude remains almost constant with various turning radius. This phenomenon violates the experimental results reported in [9] [28] [32] [34]. When the turning radius is very large, i.e. 500 meters, the difference of the sprocket torques at the outside and inside tracks is small, because turning at large radius should approximate straight-running situation. A typical tracked vehicle sprocket torque plot under skid steering is shown in Figure 3.4 [29]. It can be seen that the model output from Steeds' model look very differently from experiment results.

The reason for the poor predictive capability of using Steeds' model, discussed by Wong, is primarily because of the assumption that the lateral shear stress obeys Coulomb's law of friction [29]. Coulomb's law of friction implies that the maximum shear stress between the track and ground is developed instantly, as soon as a small relative movement between the track and the ground is developed. However, experimental evidence has shown that the shear stress is dependent on the shear displacement, which can also be seen in the track-terrain and wheel-terrain interaction models presented in Chapter 2. This means that the shear stress will reach its maximum value only after a certain shear displacement is reached. The different treatments of longitudinal (shear stress-shear displacement) and lateral (Coulomb's law of friction) direction of dynamics in Steeds' model lead to its poor modeling accuracy. Thus Wong developed a general theory for the skid steering of tracked vehicles with isotropic assumptions of the shear stress-shear displacement relationship in both longitudinal and lateral directions.
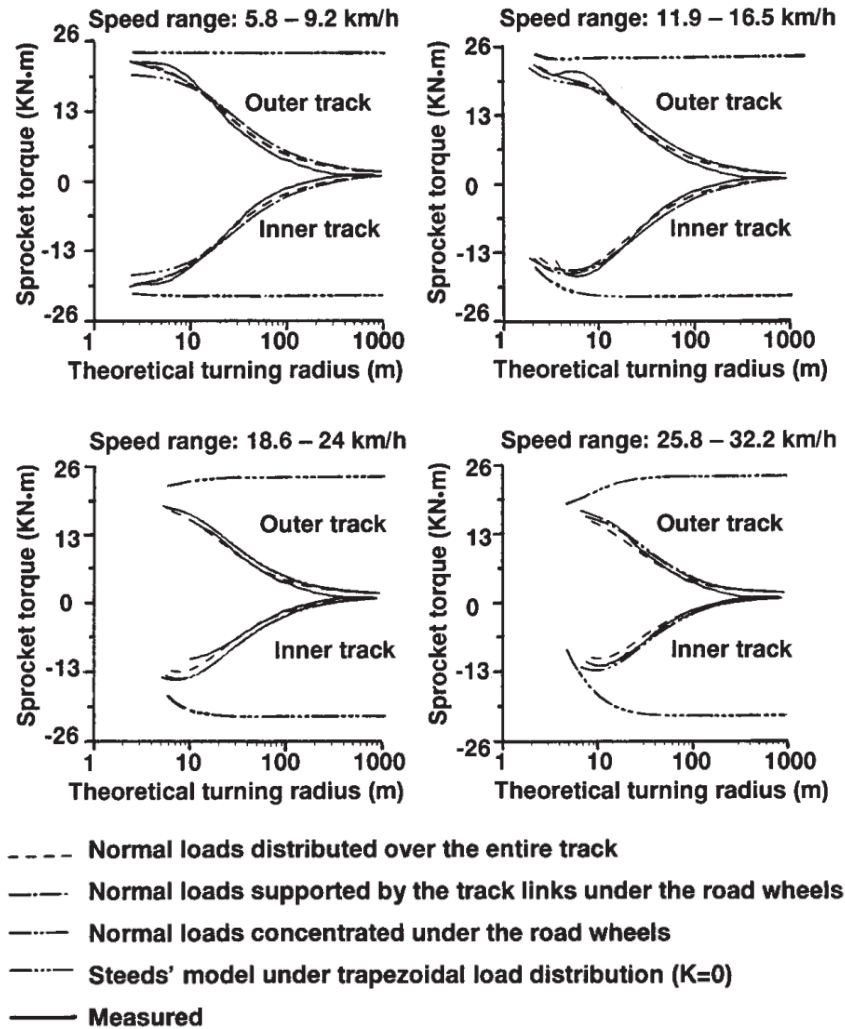
Figure 3.4 Sprocket torque measurement versus Steeds' model simulation (Source: [29])

3.3 Wong's general skid steering theory

In this section, Wong's skid steering model was reviewed. The basic assumptions of this model are as follows: (1) the shear stress developed at a given point on the track-terrain interface during a turning maneuver is dependent on the shear displacement and the relationship is $\tau = \tau_{max}(1 - e^{-j/K})$; (2) The component of the shear stress along the longitudinal direction of the track constitutes the tractive or braking effort, while the lateral component forms the lateral resistance of the track and the moments of the lateral resistance about the center of rotation of the tracks constitute the moments of turning resistance. The kinematics in a steady-state turn of a tracked vehicle is shown in Figure 3.5. The turning

center is O. X_1, Y_1 and X_2, Y_2 are reference frames fixed to and moving with the vehicle hull located on the longitudinal centerline of the outer and inner track.
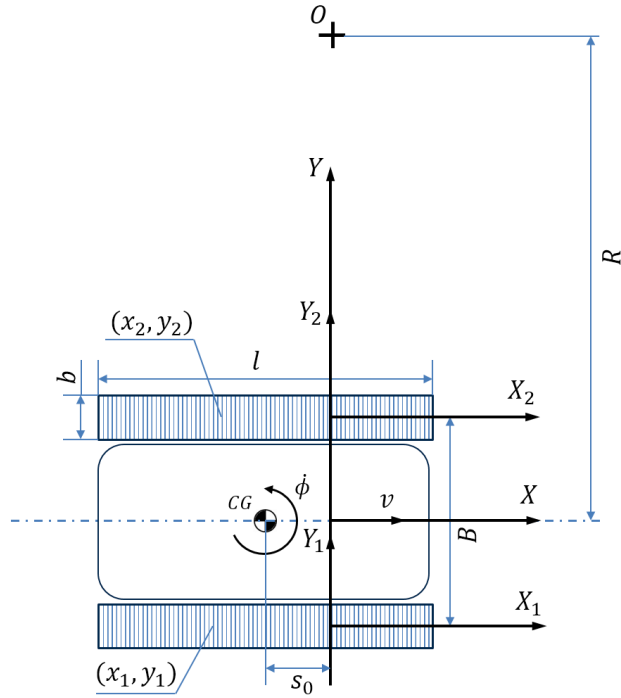
Figure 3.5 The kinematics of a tracked vehicle in a steady state turn

The shear displacements j_{xo}, j_{yo}, at a point (x_1, y_1) on the outside track in the X- and Y- directions with respect to a fixed frame of reference XY, are expressed by the following equations:

$$j_{xo} = \left(R + \frac{B}{2} + y_1\right) \sin\left[\frac{\left(\frac{l}{2} - s_0 - x_1\right)\dot{\phi}}{r\omega_0}\right] - \left(\frac{l}{2} - s_0\right)$$

$$+ x_1 \cos\left[\frac{\left(\frac{l}{2} - s_0 - x_1\right)\dot{\phi}}{r\omega_0}\right]$$

$$j_{yo} = \left(R + \frac{B}{2} + y_1\right)\left\{\cos\left[\frac{\left(\frac{l}{2} - s_0 - x_1\right)\dot{\phi}}{r\omega_0}\right]\right.$$

$$\left. - 1\right\} - x_1 \sin\left[\frac{\left(\frac{l}{2} - s_0 - x_1\right)\dot{\phi}}{r\omega_0}\right]$$

(3.8)

where $\dot{\phi}$ is the yaw rate about the turning center O, R is the turning radius, r is the sprocket radius, ω_o is the sprocket angular velocity of the outside track, B is the tread of the vehicle, l is the contact track length, b is track width and s_0 is the offset of the turning center. Thus the resultant shear displacement of the point (x_1, y_1) on the outside track is expressed as:

$$j_o = \sqrt{j_{xo}^2 + j_{yo}^2} \tag{3.9}$$

Similarly, the shear displacement of a point (x_2, y_2) on the inside track in the X-, Y- directions with respect to a fixed frame of reference XY are expressed by the following equations:

$$j_{xi} = \left(R - \frac{B}{2} + y_2\right) \sin\left[\frac{\left(\frac{l}{2} - s_0 - x_2\right)\dot{\phi}}{r\omega_i}\right] - \left(\frac{l}{2} - s_0\right)$$

$$+ x_2 \cos\left[\frac{\left(\frac{l}{2} - s_0 - x_2\right)\dot{\phi}}{r\omega_i}\right]$$

$$j_{yi} = \left(R - \frac{B}{2} + y_2\right)\left\{\cos\left[\frac{\left(\frac{l}{2} - s_0 - x_2\right)\dot{\phi}}{r\omega_{0i}}\right]\right.$$

$$\left. - 1\right\} - x_2 \sin\left[\frac{\left(\frac{l}{2} - s_0 - x_2\right)\dot{\phi}}{r\omega_i}\right] \tag{3.10}$$

where ω_i is the sprocket angular velocity of the inside track. The resultant shear displacement of the point (x_2, y_2) on the inside track is then expressed as:

$$j_i = \sqrt{j_{xi}^2 + j_{yi}^2} \tag{3.11}$$

The resultant shear stress on the track-terrain interface follows Bekker's equation as an exponential function of shear displacement as shown below.

$$\tau_{o,i} = (c + \sigma_{o,i} \tan\phi)\left(1 - e^{-j_{o,i}/K}\right) \tag{3.12}$$

where $\sigma_{o,i}$ is the normal pressure on the outside/inside track, c and ϕ are the cohesion and internal frictional angle of the terrain, and K is the shear deformation modulus of the terrain. Based on the assumptions above, the unit force dF_o and dF_i on the outside and inside tracks are calculated from

$$dF_{o,i} = (c + \sigma_{o,i} \tan \phi)(1 - e^{-j_{o,i}/K})dA \tag{3.13}$$

where dA is an area element on the track. The longitudinal forces F_{xo} and F_{xi}, and the lateral forces F_{yo} and F_{yi} are then expressed as:

$$F_{x(o,i)} = -\int_{-\frac{l}{2}-s_0}^{\frac{l}{2}-s_0} \int_{-\frac{b}{2}}^{\frac{b}{2}} (c + \sigma_{o,i} \tan \phi)\left(1 - e^{-\frac{j_{o,i}}{K}}\right) \sin \delta_{1,2} dx_{1,2} \, dy_{1,2}$$

$$F_{y(o,i)} = -\int_{-\frac{l}{2}-s_0}^{\frac{l}{2}-s_0} \int_{-\frac{b}{2}}^{\frac{b}{2}} (c + \sigma_{o,i} \tan \phi)\left(1 - e^{-\frac{j_{o,i}}{K}}\right) \cos \delta_{1,2} dx_{1,2} \, dy_{1,2} \tag{3.14}$$

where δ_1 and δ_2 are the angles between the resultant shear displacement direction and the lateral direction of the points on the outside and inside tracks respectively.

$$\sin \delta_{1,2} = \frac{j_{xo,i}}{j_{o,i}} \quad and \quad \cos \delta_{1,2} = \frac{j_{yo,i}}{j_{o,i}} \tag{3.15}$$

Assuming that the center of gravity is at the vehicle's geometric center, then the turning moments M_{Lo} and M_{Li} due to the longitudinal shear forces are expressed as the following:

$$M_{L(o,i)} = -\int_{-\frac{l}{2}-s_0}^{\frac{l}{2}-s_0} \int_{-\frac{b}{2}}^{\frac{b}{2}} \left(\frac{B}{2} + y_1\right)(c$$

$$+ \sigma_{o,i} \tan \phi)\left(1 - e^{-\frac{j_{o,i}}{K}}\right) \sin \delta_{1,2} dx_{1,2} \, dy_{1,2} \tag{3.16}$$

$$M_{T(o,i)} = -\int_{-\frac{l}{2}-s_0}^{\frac{l}{2}-s_0} \int_{-\frac{b}{2}}^{\frac{b}{2}} x_1 (c + \sigma_{o,i} \tan \phi)\left(1 - e^{-\frac{j_{o,i}}{K}}\right) \cos \delta_{1,2} dx_{1,2} \, dy_{1,2}$$

Considering the load transfer induced by the centrifugal force, the normal pressure distributions on the outside and inside tracks are different. Ignoring the effect of the side slip angle β, the normal pressures on the tracks are:

$$p_o = \frac{\frac{mg}{2} + \frac{mv^2}{BR}h}{bL}$$

$$p_i = \frac{\frac{mg}{2} - \frac{mv^2}{BR}h}{bL} \tag{3.17}$$

Given the longitudinal and lateral forces on the outside and inside tracks and the turning and resistance moments, three equations for steady state skid steering can be generated:

43

$$\sum F_x = 0 \quad F_{xo} + F_{xi} = R_{to} + R_{ti} + \frac{mv^2}{R}\sin\beta$$

$$\sum F_y = 0 \quad F_{yo} + F_{yi} = \frac{mv^2}{R}\cos\beta \qquad (3.18)$$

$$\sum M_o = 0 \quad M_{Lo} - M_{Li} - \frac{B}{2}(R_{to} - R_{ti}) + \frac{mv^2}{R}\cos\beta\, s_0 = M_{To} + M_{Ti}$$

where R_{to} and R_{ti} are the compaction resistance on the outside and inside tracks, calculated from the pressure-sinkage relationship shown in Chapter 2. The side slip angle β can be expressed as $\beta = \tan^{-1}(s_0/R)$. It should be noted that given the vehicle parameters, s_0 (offset of turning center), ω_o (outside track rotational speed) and ω_i (inside track rotational speed) are the three variables to be solved from (3.18).

3.3.1 Numerical method

Solving 3 unknowns with 3 equations is theoretically possible yet not necessarily straightforward. Finding explicit solutions for s_0, ω_o and ω_i is hard because the equations contain exponential terms and double integration. There is no discussion of the solution method in [29]. We solve this problem by using the Newton-Raphson method. A solution vector $x = [s_0, \omega_o, \omega_i]'$ is generated, and we rewrite the equation set (3.18) to:

$$F(x) = \begin{bmatrix} F_{xo} + F_{xi} - \left(R_{to} + R_{ti} - \frac{mv^2}{R}\sin\beta\right) \\ F_{yo} + F_{yi} - \frac{mv^2}{R}\cos\beta \\ M_{Lo} - M_{Li} - \frac{B}{2}(R_{to} - R_{ti}) + \frac{mv^2}{R}\cos\beta\, s_0 - M_{To} - M_{Ti} \end{bmatrix} = 0 \qquad (3.19)$$

Newton-Raphson method then results in:

$$x_{k+1} = x_k - \frac{F(x_k)}{F'(x_k)} \qquad (3.20)$$

To initiate this iteration, a set of good starting values x_0 is given. We use

$$x_0 = \begin{bmatrix} \dfrac{l}{4} & \dfrac{(R + B/2)\dot{\phi}}{r} & \dfrac{(R - B/2)\dot{\phi}}{r} \end{bmatrix}' \qquad (3.21)$$

An initial value of s_0 is set as $l/4$, which is reasonable, because it is known that s_0 ranges between 0 and $l/2$. Initial values of ω_o and ω_i are calculated from the (idealized) no-slip speed relationship.

The numerical method for approximating $F'(x_k)$ is shown in the following.

$$F'(x_k) \approx \begin{pmatrix} \dfrac{\Delta \sum F_x}{\Delta s_0} & \dfrac{\Delta \sum F_x}{\Delta \omega_o} & \dfrac{\Delta \sum F_x}{\Delta \omega_i} \\[2mm] \dfrac{\Delta \sum F_y}{\Delta s_0} & \dfrac{\Delta \sum F_y}{\Delta \omega_o} & \dfrac{\Delta \sum F_y}{\Delta \omega_i} \\[2mm] \dfrac{\Delta \sum M_o}{\Delta s_0} & \dfrac{\Delta \sum M_o}{\Delta \omega_o} & \dfrac{\Delta \sum M_o}{\Delta \omega_i} \end{pmatrix} \tag{3.22}$$

The iteration stops when the absolute value of all three equations in Eq. (3.19) is less than 0.001. With a given Packbot-like SUGV (with parameters shown in Table 3.3), solutions of s_0, ω_o and ω_i on three types of soils are shown in Figure 3.6, Figure 3.7 and Figure 3.8. We also obtain sprocket torque and power consumption of the outside and inside tracks, as shown in Figure 3.9 and Figure 3.10.

Table 3.3 Simulation parameters

Vehicle Parameters	
Mass, m (kg)	30
Track Length, l (m)	0.7
Track Width, b (m)	0.07
Tread Width, B (m)	0.4
Sprocket Radius, r (m)	0.1
CG Height, h (m)	0.15
Soil Parameters	
Shear Deformation Modulus, K (m)	0.025
Sinkage Exponent, n	1.1
Cohesive Modulus, k_c (kN/m^{n+1})	0.9
Frictional Modulus, k_ϕ (kN/m^{n+2})	1523.4
Cohesion, c (Pa)	1000
Internal Friction Angel, ϕ (°)	30
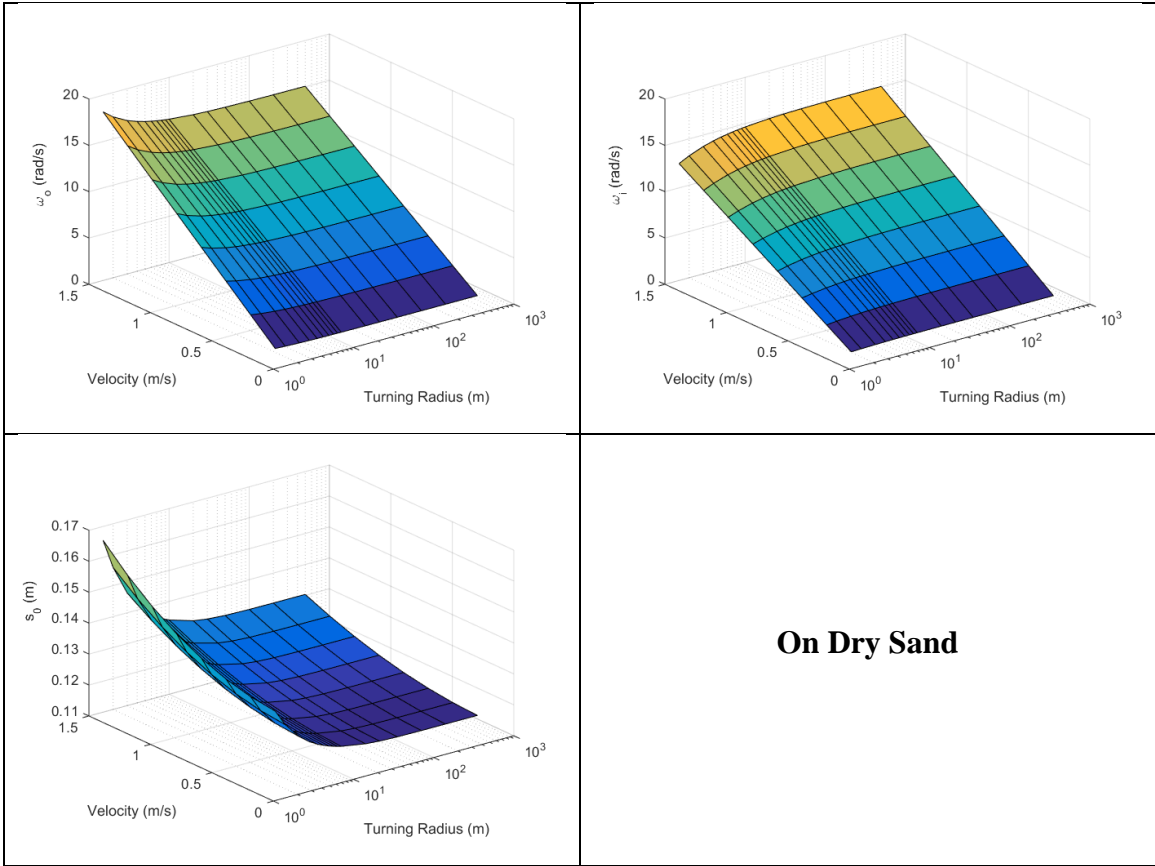
Figure 3.6 The solutions of a tracked SUGV in skid steering on dry sand
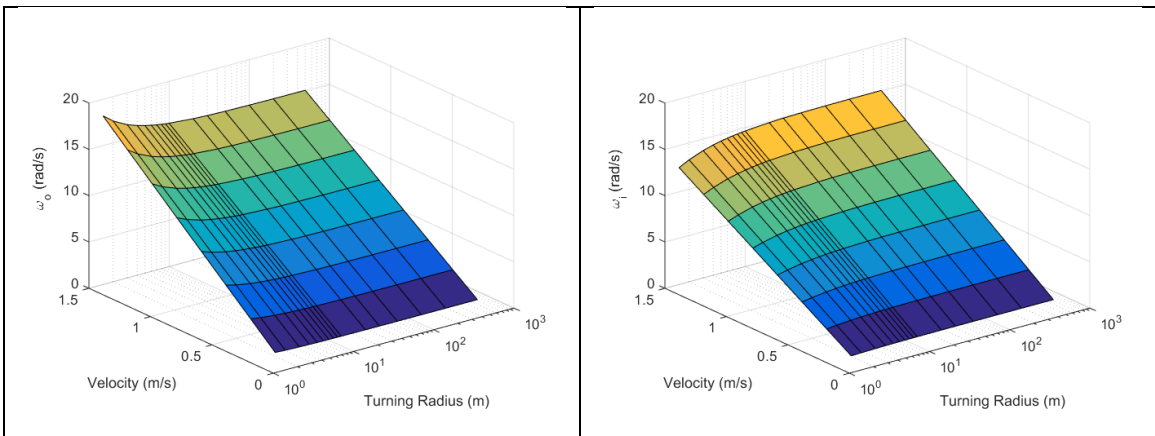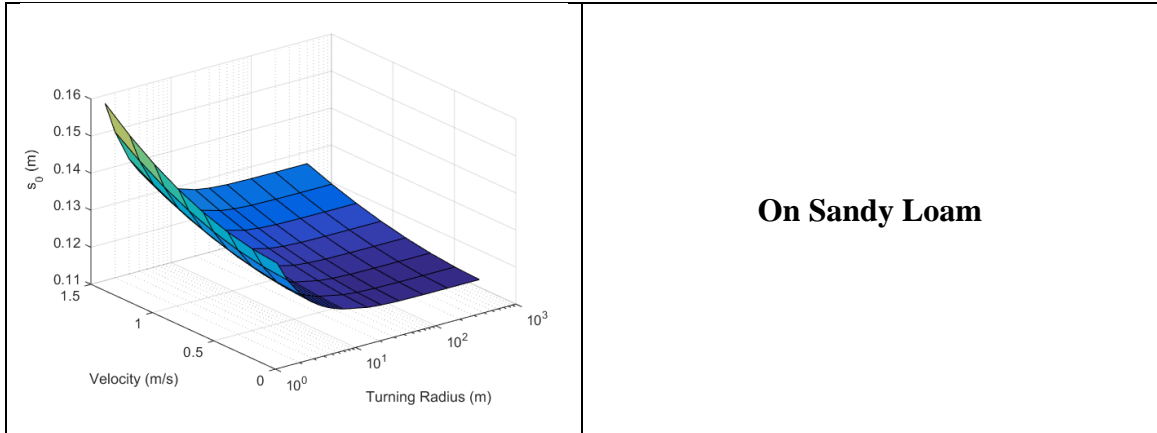
On Sandy Loam

Figure 3.7 The solutions of a tracked SUGV in skid steering on sandy loam
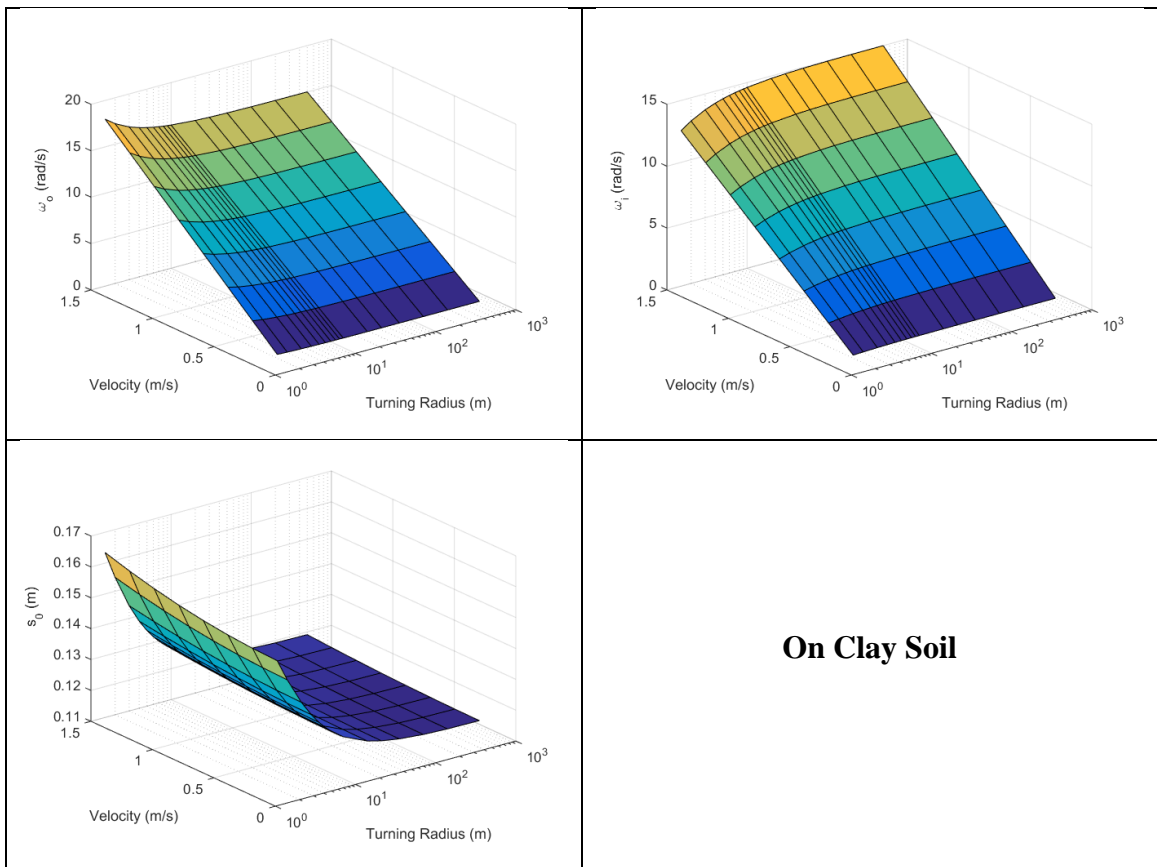
On Clay Soil

Figure 3.8 The solutions of a tracked SUGV in skid steering on clay soil

Figure 3.9 Sprocket torque of the outside and inside tracks under various vehicle forward speeds

Figure 3.10 Power consumption of the outside and inside tracks under various vehicle forward speed

From Figure 3.9 and Figure 3.10 it can be seen that skid steering can consume a large amount of power when the turning radius is small.

Our numerical method is not fast. The time to obtain a solution $(s_0, \omega_o, \omega_i)$ map $(8 \times 16$ points) is 244.8 seconds on an Intel i7 quad core 4.4GHz desktop with 16G

DRAM. Therefore, a faster model is needed for real-time applications or extensive design studies. In Chapter 5, a simplified skid steering model for tracked SUGVs will be developed and discussed.

3.4 Instantaneous center of rotation (ICR) model

Another widely used method in modeling skid steering maneuvers is the ICR method proposed by Martinez, and further refined by Yi, Wu, etc. [37] [38] [39] [40]. It can be seen from Wong's method that direct implementation on robotic platforms is difficult due to the complexity, computation resources, and need for extensive knowledge of vehicle and terrain parameters. The ICR method, however, use kinematic relationship to enable fast computation and only need a small number of parameters.

The local frame of the vehicle is assumed to have its X-axis aligned with the forward direction shown in Figure 3.11. The CG is again assumed to be collocated with the geometrical center of the vehicle.
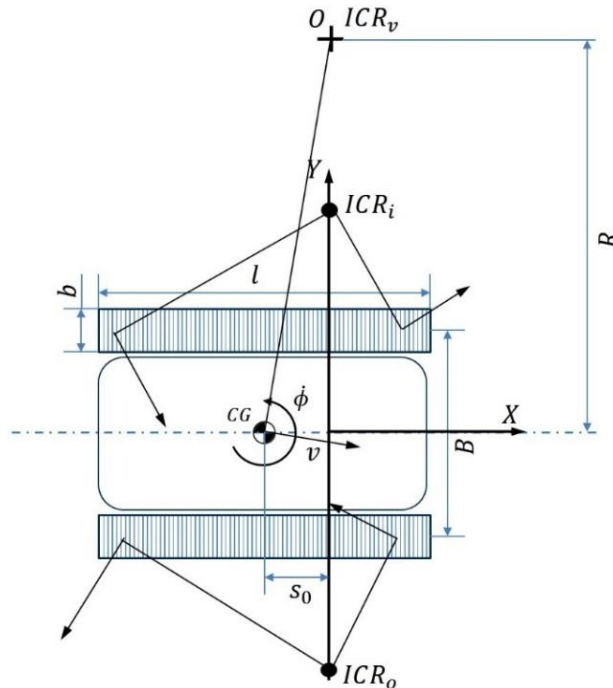
Figure 3.11 Schematic diagram of the ICR model with the two ICRS of the tracks illustrated

If the vehicle is considered as a rigid body with planar motion, then its instantaneous center of rotation (ICR) is defined as the point on the horizontal plane where

the motion of the vehicle can be represented by a rotation and no translation. In Figure 3.11, the vehicle's ICR is labeled as ICR_v or the origin O. In the planar motion of a tracked vehicle, the motion of both tracks should be considered. A track can be modeled as another rigid body with an extra degree of freedom, which is its rolling speed. Thus the motion of a point on the contact surface is the composition of the motion of the vehicle and that due to track rolling. Because of this, the ICR of a track on the motion plane is different from the ICR of the entire vehicle. Then the ICRs for the inside and outside tracks can be defined in the local frame as ICR_i and ICR_o respectively, shown on Figure 3.11. The position of the track ICRs can be calculated with vehicle forward velocity v_x, vehicle lateral velocity v_y, vehicle yaw rate $\dot{\phi}$, and inside and outside track rotational velocity ω_i and ω_o.

$$x_{ICRo} = x_{ICRi} = s_0 = \frac{v_y}{\dot{\phi}}$$

$$y_{ICRo} = \frac{\omega_o r - v_x}{\dot{\phi}} \tag{3.23}$$

$$y_{ICRi} = \frac{\omega_i r - v_x}{\dot{\phi}}$$

Having known the ICR positions of the outside and inside tracks, the calculation of the shear force on the contact surface is based on the general isotropic friction model with Coulomb friction law.

$$d\vec{f} = -\mu p \frac{\vec{v}}{\|v\|} dA \tag{3.24}$$

where p is the pressure on a contact element dA on the contact surface, μ is the friction coefficient that depends both on track and terrain types, and $\vec{v}$ is the slipping velocity of a contact element dA which can be calculated based on the distance to the ICR position times vehicle yaw rate.

$$\vec{v} = \dot{\vec{\phi}} \times \vec{d} \tag{3.25}$$

where $\vec{d}$ is the distance vector between the contact element dA and ICR position in the local frame.

The longitudinal force and lateral force on the outside and inside tracks can be calculated with the integration of the $d\vec{f}$ along the contact surface.

$$F_x = b\mu \int_{-\frac{L}{2}}^{\frac{L}{2}} d\vec{f} \cos \theta \, dx$$

(3.26)

$$F_y = b\mu \int_{-\frac{L}{2}}^{\frac{L}{2}} d\vec{f} \sin \theta \, dx$$

Figure 3.12 and Figure 3.13 show the torque and power consumption of the outside and inside track in the ICR model with $\mu = 1.12$ [49]. Other simulation parameters are the same as those used for the Wong's model.
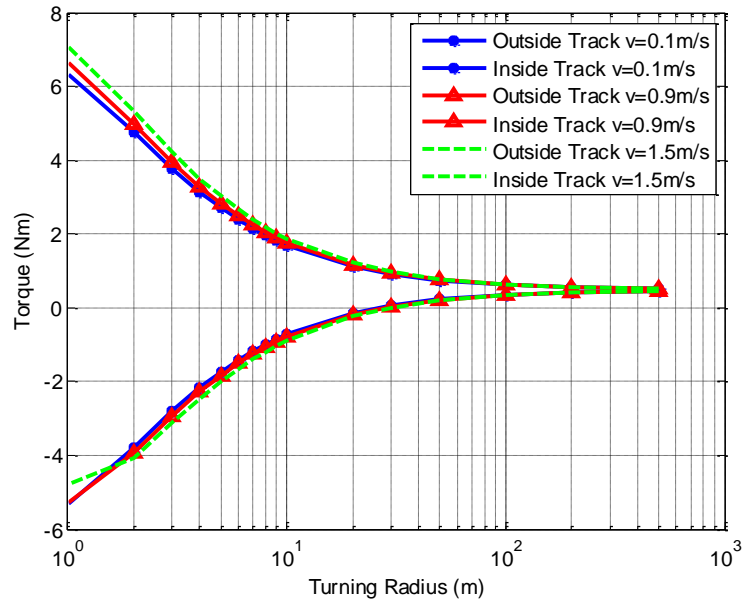

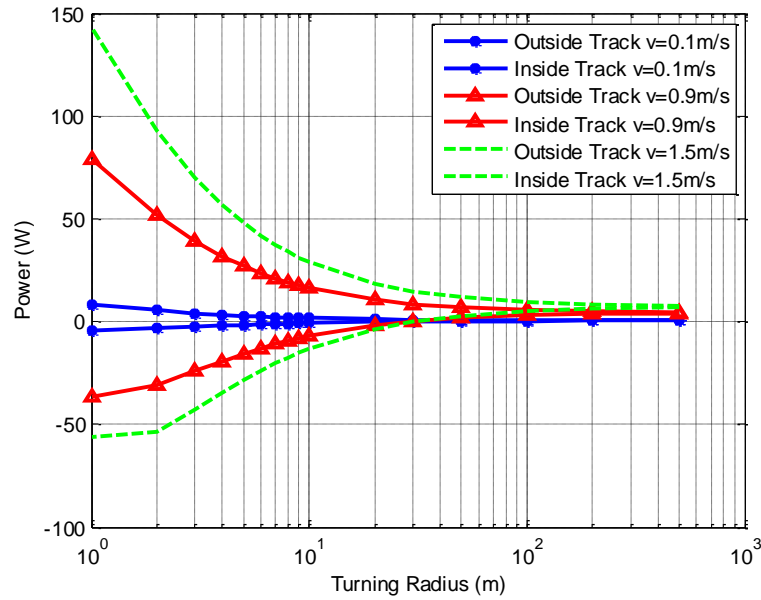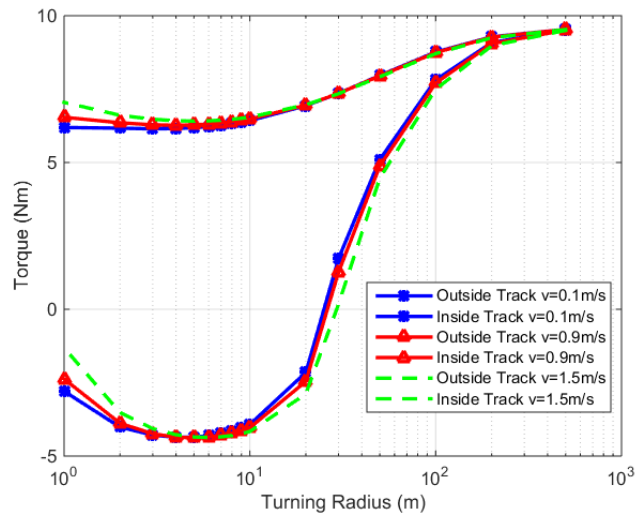Figure 3.12 Sprocket torque of the outside and inside tracks under various vehicle forward speeds
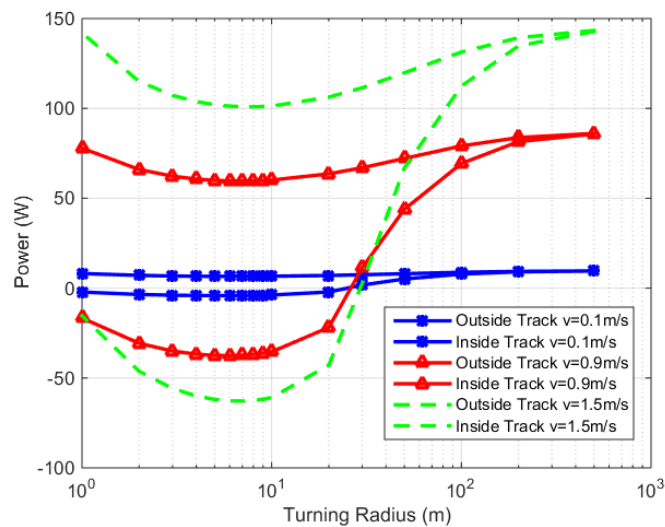
Figure 3.13 Power consumption of the outside and inside tracks under various vehicle forward speeds

From Figure 3.12 and Figure 3.13 it can be seen that the torque and power consumption of the outside and inside track are very different from the results shown in Figure 3.9 and Figure 3.10. In fact, none of the literature so far using the ICR model has plotted torque and power consumption for the large range of turning radius from 1m to 500m. And the results of ICR model, especially when the turning radius is large, is questionable. The reason is that in the ICR model the shear force on the contact surface is assumed to be saturated regardless of turning radius and slip ratio. In Wong's model, it can be seen that when the turning radius is small, the soil fails and the shear force on the contact surface is saturated, however when the turning radius is large, the soil does not fail and the shear force is not saturated. Therefore the ICR model is only suitable for small turning radius cases. Although the coefficient μ can be tuned separately in the X and Y directions [37] or tuned for different turning radius and forward speed [41] to fit the experiment data, μ loses its physical meaning as coulomb friction coefficient. Overall, the ICR model is only useful for small turning radius cases.

3.5 Comparisons between the three skid steering models

All the three skid steering models (Steed's Model, Wong's Model, and ICR Model) consider the offset of the turning center s_0 in the modeling of skid steering maneuver. But they differ from each other mainly in the modeling of the lateral shear displacement and the corresponding shear stress. In Steed's model, the longitudinal and lateral shear stress are modeled separately. The longitudinal shear stress is calculated based on Bekker's shear stress – shear displacement relationship, while the lateral shear stress is developed based on Coulomb law of friction, which means that the lateral shear stress reaches its maximum value instantly as soon as a small relative movement on the contact surface is initiated. In the ICR model, both the longitudinal and the lateral shear stress are developed based on Coulomb law of friction. And the direction of the friction is determined by the instantaneous center of rotation of each track. As both of these models do not consider the development of shear displacement in the lateral direction, they are only useful in small turning radius cases when the shear displacement is large so that the shear stress can be assumed to be saturated on the contact surface. Wong's model considers the development

of shear displacement in both the longitudinal and lateral direction. Thus this model can predict the forces and moments on the contact surface more accurately. However, Wong's model is more complicated and requires more computation power than both Steed's model and the ICR model. In fact, finding explicit solutions of Wong's model is very hard. In this chapter, we proposed a numeric method to approximate the solutions.

Figure 3.14 shows the comparison of the lateral shear stress between the three models. It can be seen that the lateral shear stress distribution on the contact surface differs each other in the three models. In Wong's model, only when there is shear displacement between the track and terrain, there is shear stress. However, in Steeds' and ICR model, when there is shear speed between the track and terrain, there is shear stress. Specifically for the tip point of the contact patch, although it may have a very large shear speed, yet it has no shear displacement. In Steeds and ICR model, this tip point has maximum shear stress, while in Wong's model this point has no shear stress. Steeds and ICR model have only been verified in small turning radius conditions, usually smaller than 10 meters, while Wong's model is verified by experiments from small radius turning ($R = 1m$) to large radius turning ($R = 1000m$). Steeds and ICR models are useful with fine tuning of the coefficient μ in small radius turning maneuvers on hard soil where the terrain can easily fail and frictional force dominates. Figure 3.15 shows the comparison of μ_t (the lateral coefficient of friction, also known as the coefficient of turning resistance) between the three models. In both Steeds model and ICR model, this coefficient computes the yaw moment of turning resistance. μ_t is defined as:

$$\mu_t = \frac{M_T}{WL} \tag{3.27}$$

where M_T is the total turning resistance moment, W is vertical load, L is track length.

From Figure 3.15 it can be seen that μ_t in Steeds model remains constant, while it varies with forward speed and turning radius in Wong's and ICR models. This is because in Steeds model the longitudinal and lateral dynamics are considered separately and a constant μ_t is assumed. μ_t in Wong's model can be the same as the ICR model in extreme cases (forward velocity is 1.5m/s and turning radius is 1m), when the soil fails and shear stress is saturated. Throughout the surface studied, qualitatively μ_t in the ICR model shares the same trend with Wong's, yet quantitatively they result in different values.
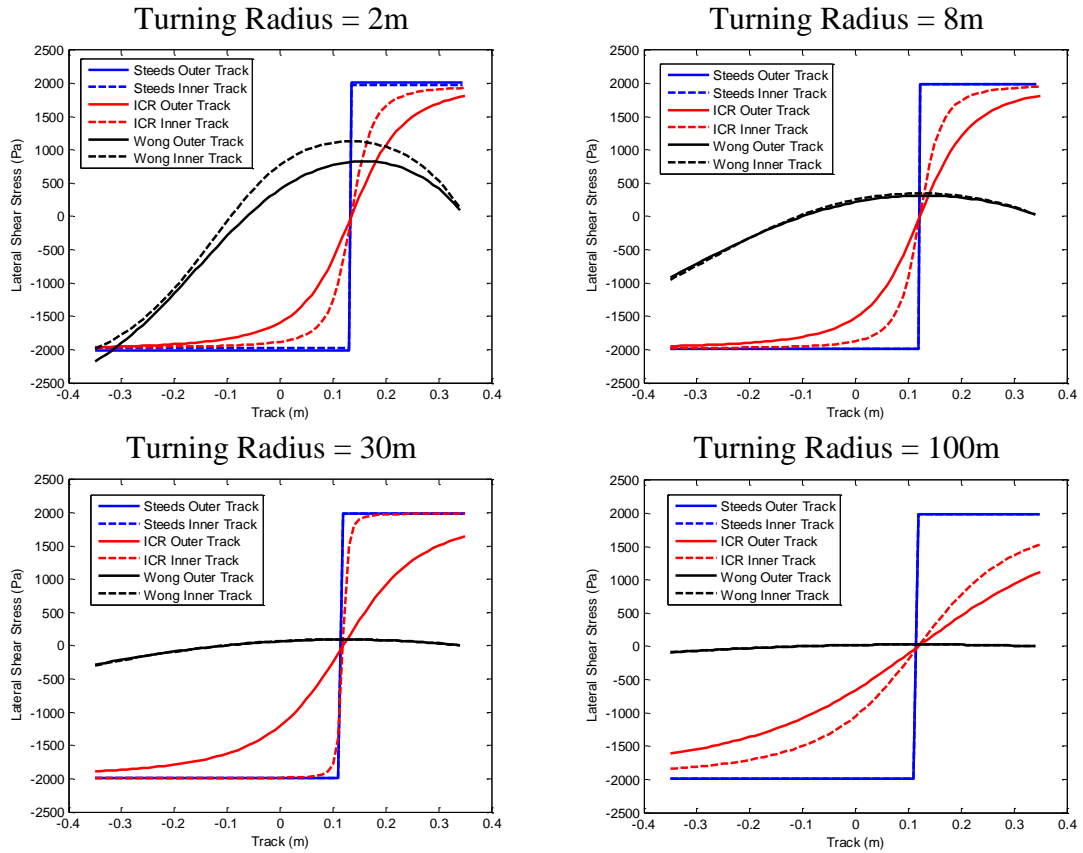
Figure 3.14 Comparison of the lateral shear stress between Steed's, ICR and Wong's models
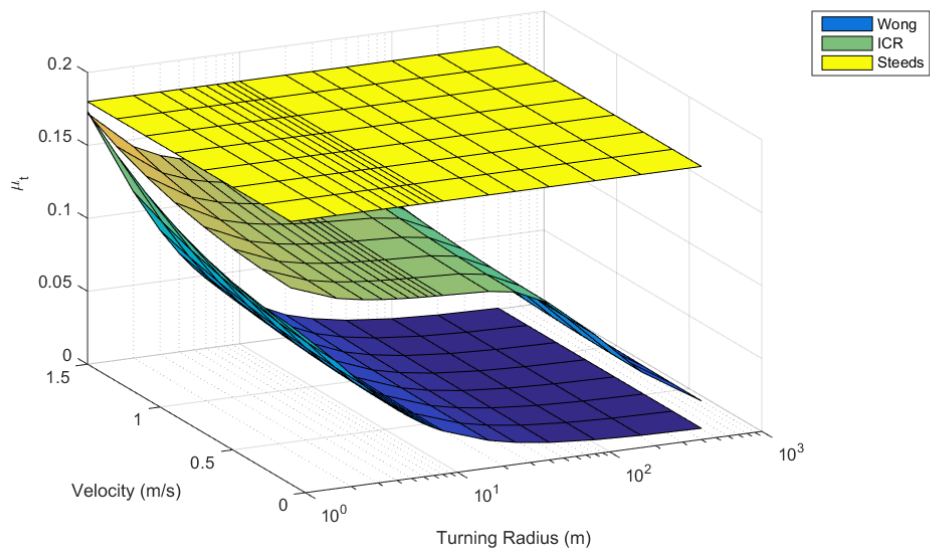
Figure 3.15 Comparison of μ_t between Steed's, ICR and Wong's models

3.6 Summary

Three widely used skid steering models (Steeds, Wong, and the ICR) for tracked SUGVs running off-road were reviewed and compared in this chapter. Steeds' and the ICR models viewed the shear force as frictional force. Thus these two models did not consider the shear displacement on the contact surface. These two models were shown to be fast to compute and capable of predicting SUGVs' motions on hard soil in small turning radii cases. Wong's model was shown to be the most accurate among the three as the shear stress is calculated by shear stress-shear displacement relationship. However, finding the solutions for Wong's model is computationally intensive. A numerical method to achieve solutions in steady state was presented in this chapter.

CHAPTER 4
Skid Steering Model of Wheeled SUGVs

In Chapter 3, three skid steering models for tracked vehicles were studied and discussed. The Wong's model was shown to be the most accurate. Although there is literature about modeling of skid steering of wheeled SUGVs using Steeds' or ICR models, there is little or no open literature so far about skid steering on wheeled SUGVs using Wong's model. We extended Wong's general skid steering theory on tracked vehicles to wheeled vehicles in this chapter, utilizing the wheel-terrain interaction model developed in Chapter 2. The difficulty in developing this model lays in the complexity of Wong's skid steering model and the complexity of normal and shear stress distribution on the wheel-terrain interaction.

4.1 Difference between tracked and wheeled SUGVs on skid steering

The mechanism to achieve skid steering on tracked and wheeled SUGVs is similar. However, the normal and shear stress on the contact surface between wheel and terrain is different to those of track, especially on soft soils where sinkage is severe, as was stated in the single wheel-terrain interaction model in Chapter 2. Thus skid steering for wheeled SUGVs on soft soils should be further developed. Due to the complexity of single wheel-terrain model, the skid steering model for wheeled SUGVs is more complicated than that of tracked SUGVs.
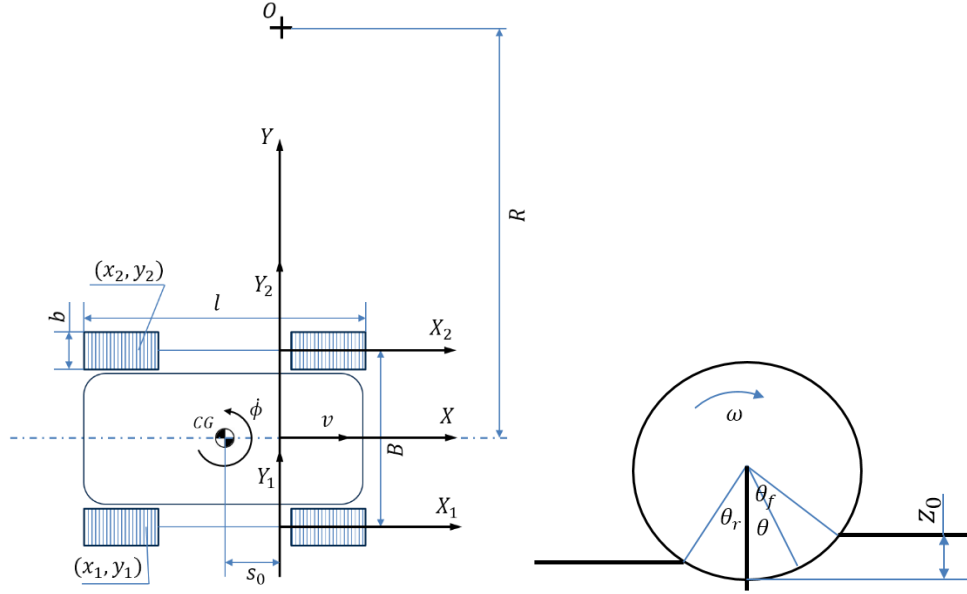
Figure 4.1 The kinematics of a wheeled vehicle in a steady state turn

A 4-wheel SUGV in skid steering maneuver is shown in Figure 4.1. X, Y is the global frame. X_1, Y_1 and X_2, Y_2 are the reference frames fixed to and moving with the vehicle hull located on the longitudinal centerline of the outer and inner wheels. θ is the local frame on the wheel. Front outside, front inside, rear outside, and rear inside wheels are denoted as fo, fi, ro and ri respectively. We also assume that the wheels on the same side of the driveline share the same speed, which means $\omega_{fo} = \omega_{ro}$ and $\omega_{fi} = \omega_{ri}$. This is a reasonable assumption, because shafts of wheels on the same side are usually connected together with chain or belt to have simple all-wheel drive configuration, which is widely used on SUGVs. Similar to the kinematic analysis of shear velocity presented in Chapter 3, we can write the shear velocity of each wheel in the X_1, Y_1 and X_2, Y_2 frame as

$$\widehat{v_{fo}} = \begin{bmatrix} \left(\dfrac{B}{2} + R + y_1\right)\dot{\phi} - r\omega_o \\ x_1\dot{\phi} \end{bmatrix} \quad \widehat{v_{fi}} = \begin{bmatrix} \left(-\dfrac{B}{2} + R + y_2\right)\dot{\phi} - r\omega_i \\ x_2\dot{\phi} \end{bmatrix}$$

$$\widehat{v_{ro}} = \begin{bmatrix} \left(\dfrac{B}{2} + R + y_1\right)\dot{\phi} - r\omega_o \\ x_1\dot{\phi} \end{bmatrix} \quad \widehat{v_{ri}} = \begin{bmatrix} \left(-\dfrac{B}{2} + R + y_2\right)\dot{\phi} - r\omega_i \\ x_2\dot{\phi} \end{bmatrix} \tag{4.1}$$

where B is the tread of the vehicle, r is the wheel radius, R is the turning radius, $\dot{\phi}$ is the yaw rate of the vehicle, ω_o and ω_i are the outside and inside wheel angular speeds. Considering the wheel-terrain interaction model, there is an angle θ between the skid

57

steering motion frame and the shear frame on the contact surface on the wheel. So the expression above should be rewritten to the following

$$\widetilde{v_{fo}} = \begin{bmatrix} \left(\frac{B}{2} + R + y_1\right)\dot{\phi}\cos\theta - r\omega_o \\ x_1\dot{\phi} \end{bmatrix}$$

$$\widetilde{v_{fi}} = \begin{bmatrix} \left(-\frac{B}{2} + R + y_2\right)\dot{\phi}\cos\theta - r\omega_i \\ x_2\dot{\phi} \end{bmatrix}$$

(4.2)

$$\widetilde{v_{ro}} = \begin{bmatrix} \left(\frac{B}{2} + R + y_1\right)\dot{\phi}\cos\theta - r\omega_o \\ x_1\dot{\phi} \end{bmatrix}$$

$$\widetilde{v_{ri}} = \begin{bmatrix} \left(-\frac{B}{2} + R + y_2\right)\dot{\phi}\cos\theta - r\omega_i \\ x_2\dot{\phi} \end{bmatrix}$$

Replacing x_1, x_2 with θ on the local wheel coordinate, we get

$$\widetilde{v_{fo}} = \begin{bmatrix} \left(\frac{B}{2} + R + y_1\right)\dot{\phi}\cos\theta - r\omega_o \\ \left(r\sin\theta + \left(\frac{wb}{2} - s_0\right)\right)\dot{\phi} \end{bmatrix}$$

$$\widetilde{v_{fi}} = \begin{bmatrix} \left(-\frac{B}{2} + R + y_2\right)\dot{\phi}\cos\theta - r\omega_i \\ \left(r\sin\theta + \left(\frac{wb}{2} - s_0\right)\right)\dot{\phi} \end{bmatrix}$$

(4.3)

$$\widetilde{v_{ro}} = \begin{bmatrix} \left(\frac{B}{2} + R + y_1\right)\dot{\phi}\cos\theta - r\omega_o \\ \left(r\sin\theta + \left(-\frac{wb}{2} - s_0\right)\right)\dot{\phi} \end{bmatrix}$$

$$\widetilde{v_{ri}} = \begin{bmatrix} \left(-\frac{B}{2} + R + y_2\right)\dot{\phi}\cos\theta - r\omega_i \\ \left(r\sin\theta + \left(-\frac{wb}{2} - s_0\right)\right)\dot{\phi} \end{bmatrix}$$

Then the shear velocity on the X_1, Y_1 and X_2, Y_2 frames can be transformed to the global (X, Y) frame.

$$\begin{bmatrix} v_{xfo} \\ v_{yfo} \end{bmatrix} = \begin{bmatrix} \cos\phi & -\sin\phi \\ -\sin\phi & -\cos\phi \end{bmatrix} \begin{bmatrix} \left(\dfrac{B}{2} + R + y_1\right)\dot{\phi}\cos\theta - r\omega_o \\ \left(r\sin\theta + \left(\dfrac{wb}{2} - s_0\right)\right)\dot{\phi} \end{bmatrix}$$

$$\begin{bmatrix} v_{xro} \\ v_{yro} \end{bmatrix} = \begin{bmatrix} \cos\phi & -\sin\phi \\ -\sin\phi & -\cos\phi \end{bmatrix} \begin{bmatrix} \left(\dfrac{B}{2} + R + y_1\right)\dot{\phi}\cos\theta - r\omega_o \\ \left(r\sin\theta + \left(-\dfrac{wb}{2} - s_0\right)\right)\dot{\phi} \end{bmatrix}$$

$$\begin{bmatrix} v_{xfi} \\ v_{yfi} \end{bmatrix} = \begin{bmatrix} \cos\phi & -\sin\phi \\ -\sin\phi & -\cos\phi \end{bmatrix} \begin{bmatrix} \left(-\dfrac{B}{2} + R + y_2\right)\dot{\phi}\cos\theta - r\omega_i \\ \left(r\sin\theta + \left(\dfrac{wb}{2} - s_0\right)\right)\dot{\phi} \end{bmatrix}$$

$$\begin{bmatrix} v_{xri} \\ v_{yri} \end{bmatrix} = \begin{bmatrix} \cos\phi & -\sin\phi \\ -\sin\phi & -\cos\phi \end{bmatrix} \begin{bmatrix} \left(-\dfrac{B}{2} + R + y_2\right)\dot{\phi}\cos\theta - r\omega_i \\ \left(r\sin\theta + \left(-\dfrac{wb}{2} - s_0\right)\right)\dot{\phi} \end{bmatrix}$$

(4.4)

where ϕ can be expressed as

$$\phi = \frac{\dot{\phi}\theta}{\omega_{o,i}} \tag{4.5}$$

Integrate $v_{fo,ro,fi,ri}$ along the contact areas, we get the shear displacement as

$$
\begin{aligned}
j_{xfo} &= \int_{\theta}^{\theta_f} v_{xfo}\frac{d\theta}{\omega_o} & j_{xfi} &= \int_{\theta}^{\theta_f} v_{xfi}\frac{d\theta}{\omega_i} \\
j_{xro} &= \int_{\theta}^{\theta_f} v_{xro}\frac{d\theta}{\omega_o} & j_{xri} &= \int_{\theta}^{\theta_f} v_{xri}\frac{d\theta}{\omega_i} \\
j_{yfo} &= \int_{\theta}^{\theta_f} v_{yfo}\frac{d\theta}{\omega_o} & j_{yfi} &= \int_{\theta}^{\theta_f} v_{yfi}\frac{d\theta}{\omega_i} \\
j_{yro} &= \int_{\theta}^{\theta_f} v_{yro}\frac{d\theta}{\omega_o} & j_{yri} &= \int_{\theta}^{\theta_f} v_{yri}\frac{d\theta}{\omega_i}
\end{aligned}
\tag{4.6}
$$

Similar to the skid steering model for tracked SUGVs, the shear displacement is

$$j = \sqrt{j_x^2 + j_y^2} \tag{4.7}$$

and the corresponding shear stress is

$$\tau_{x,y} = (c + \sigma\tan\phi)(1 - e^{-j/K})\frac{j_{x,y}}{j} \tag{4.8}$$

where σ is the normal pressure on the contact surface, which is modeled in Chapter 2. It should be pointed out that the normal pressure σ is related to angle θ. Longitudinal, lateral forces and moments on each of the wheel can then be expressed using the single wheel model mentioned in Chapter 2.

$$
\begin{cases}
F_x = rb \int_{\theta_r}^{\theta_f} (-\sigma(\theta) \sin\theta + \tau(\theta) \cos\theta) d\theta \\[2mm]
F_z = rb \int_{\theta_r}^{\theta_f} (\sigma(\theta) \cos\theta + \tau(\theta) \sin\theta) d\theta \\[2mm]
M_y = -r^2 b \int_{\theta_r}^{\theta_f} \tau(\theta) d\theta
\end{cases}
\tag{4.9}
$$

It should be stated here that in the modeling of skid steering for wheeled SUGVs, there are 2 more variables (outside and inside wheel sinkage) than the 3 variables in tracked cases (outside and inside wheel slip ratio, and offset of turning center). Because in the wheel vehicle cases, sinkage and slip ratio are coupled together, as mentioned in Chapter 2. Thus 5 equations needed to be solved simultaneously.

$$
F_{xfo} + F_{xro} + F_{xfi} + F_{xri} = \frac{mV^2}{R} \sin\beta
$$

$$
F_{yfo} + F_{yro} + F_{yfi} + F_{yri} = -\frac{mV^2}{R} \cos\beta
$$

$$
F_{zfo} + F_{zro} + F_{zfi} + F_{zri} = W
$$

$$
\frac{(F_{zfo} + F_{zro} - F_{zfi} - F_{zri})B}{2} = \frac{mV^2}{R} h
\tag{4.10}
$$

$$
\frac{(F_{xfo} + F_{xro} - F_{xfi} - F_{xri})B}{2} + s_0 \cos\beta \frac{mV^2}{R}
$$

$$
= (F_{yfo} + F_{yfi})(\frac{wb}{2} - s_0) + (F_{yro} + F_{yri})(\frac{wb}{2} + s_0)
$$

These 5 equations are longitudinal, lateral, and vertical force balances, roll and yaw moment balances.

4.2 Simulations of the skid steering model of wheeled SUGVs on deformable terrains

The numerical method for the wheeled model is similar to that of the tracked model. A solution vector $x = [\omega_o, \omega_i, z_o, z_i, s_0]'$ representing slip ratio outside and inside, sinkage outside and inside, and offset of turning center, is generated.

We also rewrite Eq. (4.10) into

$$F(x) = 0 \qquad (4.11)$$

To converge to the solution quickly, it is necessary to start from a set of good initial vector x_0. We use the single wheel-terrain interaction model output $(\widetilde{\omega}, \widetilde{z})$ and a quarter of the wheel base as the initial x_0.

$$x_0 = [\widetilde{\omega}, \widetilde{\omega}, \widetilde{z}, \widetilde{z}, \frac{wb}{4}]' \qquad (4.12)$$

The numerical method for approximating $F'(x_k)$ is shown in the following

$$F'(x_k) \approx \begin{pmatrix} \dfrac{\Delta F_1}{\Delta \omega_o} & \dfrac{\Delta F_1}{\Delta \omega_i} & \dfrac{\Delta F_1}{\Delta z_o} & \dfrac{\Delta F_1}{\Delta z_i} & \dfrac{\Delta F_1}{\Delta s_0} \\[2mm] \dfrac{\Delta F_2}{\Delta \omega_o} & \dfrac{\Delta F_2}{\Delta \omega_i} & \dfrac{\Delta F_2}{\Delta z_o} & \dfrac{\Delta F_2}{\Delta z_i} & \dfrac{\Delta F_2}{\Delta s_0} \\[2mm] \dfrac{\Delta F_3}{\Delta \omega_o} & \dfrac{\Delta F_3}{\Delta \omega_i} & \dfrac{\Delta F_3}{\Delta z_o} & \dfrac{\Delta F_3}{\Delta z_i} & \dfrac{\Delta F_3}{\Delta s_0} \\[2mm] \dfrac{\Delta F_4}{\Delta \omega_o} & \dfrac{\Delta F_4}{\Delta \omega_i} & \dfrac{\Delta F_4}{\Delta z_o} & \dfrac{\Delta F_4}{\Delta z_i} & \dfrac{\Delta F_4}{\Delta s_0} \\[2mm] \dfrac{\Delta F_5}{\Delta \omega_o} & \dfrac{\Delta F_5}{\Delta \omega_i} & \dfrac{\Delta F_5}{\Delta z_o} & \dfrac{\Delta F_5}{\Delta z_i} & \dfrac{\Delta F_5}{\Delta s_0} \end{pmatrix} \qquad (4.13)$$

Then the Newton-Raphson method results in:

$$x_{k+1} = x_k - \frac{F(x_k)}{F'(x_k)} \qquad (4.14)$$

The iteration stops when the absolute value of each equation in Eq. (4.11) is less than 0.001. With a given wheeled SUGV (same parameters as Table 3.3 except that 4 wheels are used with wheel radius $r = 0.1m$, wheel width $b = 0.074m$, and wheel base $wb = 0.45m$). Solutions on the 3 types of soils are plotted in Figure 4.2, Figure 4.3 and Figure 4.4. The computation is also too slow for real-time implementation. The total time for a solution $(s_0, \omega_o, \omega_i, z_o, z_i)$ map (5×16 points) is 1362.2 seconds on an Intel i7 quad

core 4.4GHz desktop with 16GB DRAM. Shaft torque and shaft power under different forward velocity on 3 soils are showed in Figure 4.5.

It can be seen that soil affects the torque and power consumption more for wheeled SUGVs than for tracked SUGVs. Driving at higher speeds requires larger torque and power. Moreover, torque and power consumption increase significantly when the turning radius becomes small (large yaw rate), similar to tracked SUGVs. Among the 3 soils, dry sand requires the highest torque and power, while clay soil requires the least. This demonstrates that wheeled SUGVs have less mobility on soft soil than on hard soil.
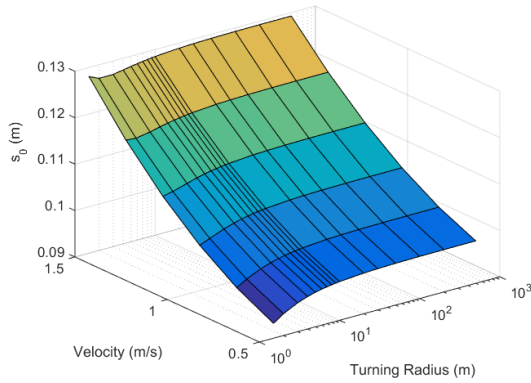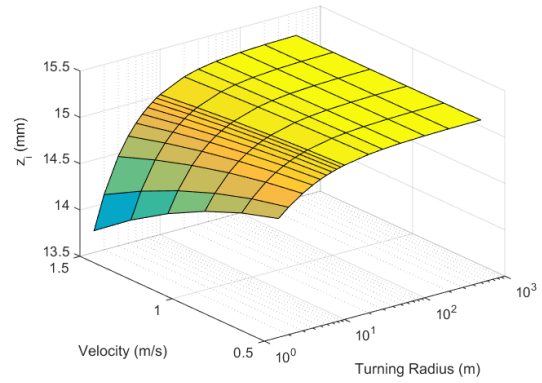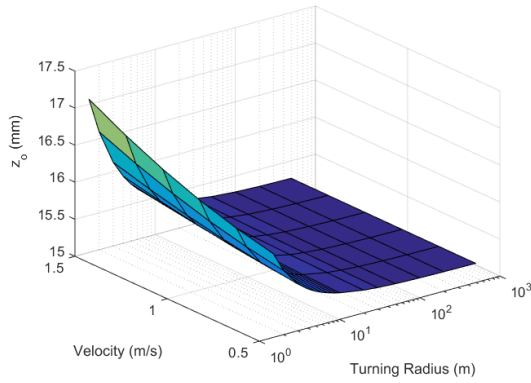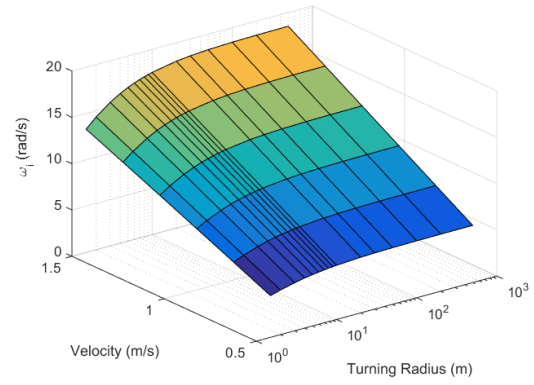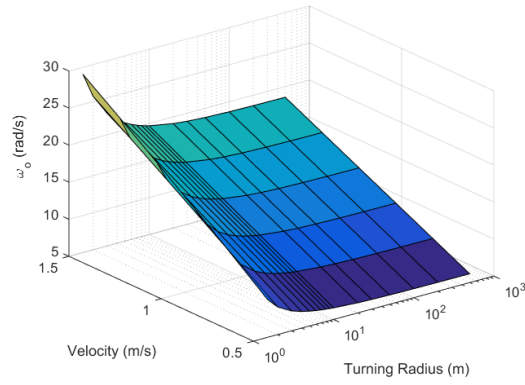
On Dry Sand

Figure 4.2 The solutions of a wheeled SUGV in skid steering on dry sand
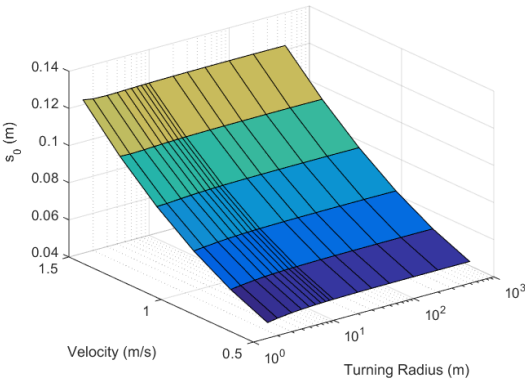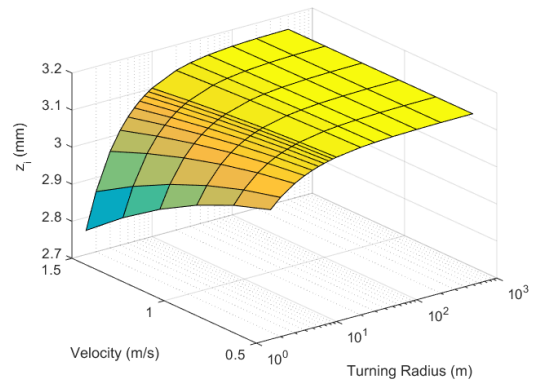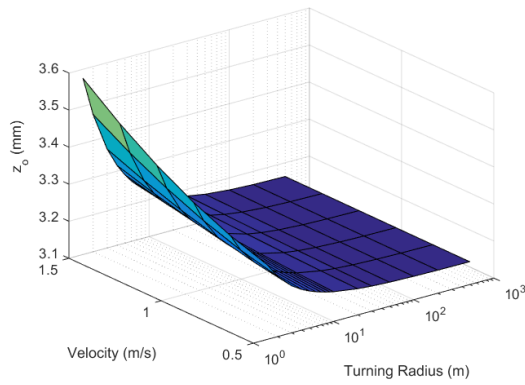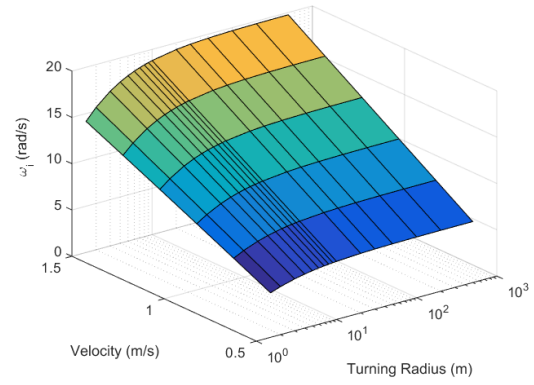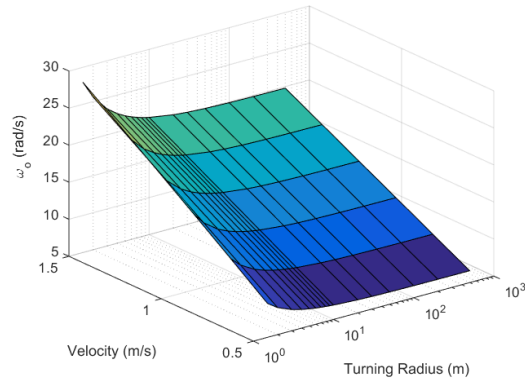
On Sandy Loam

Figure 4.3 The solutions of a wheeled SUGV in skid steering on sandy loam
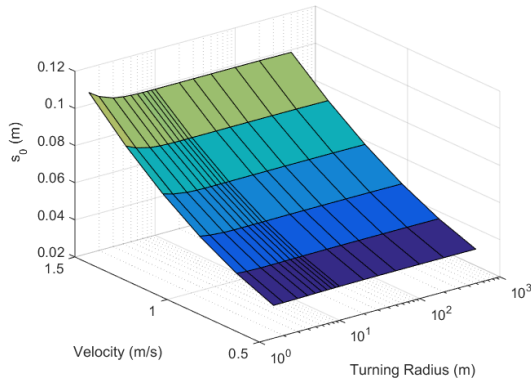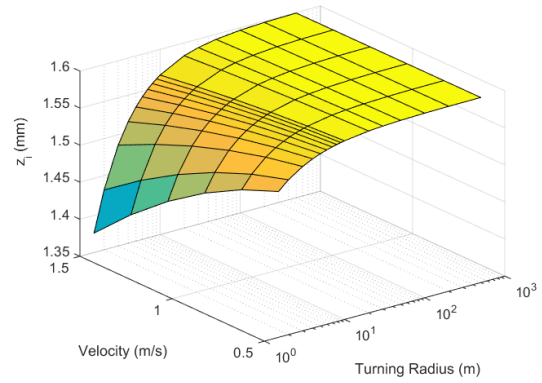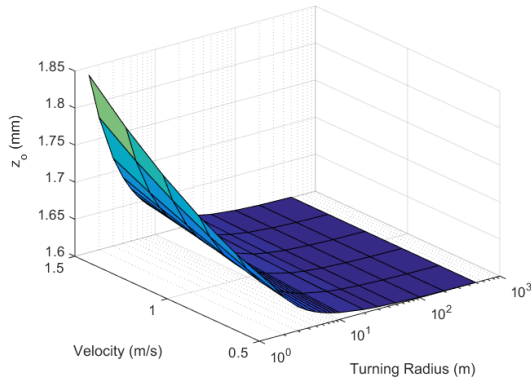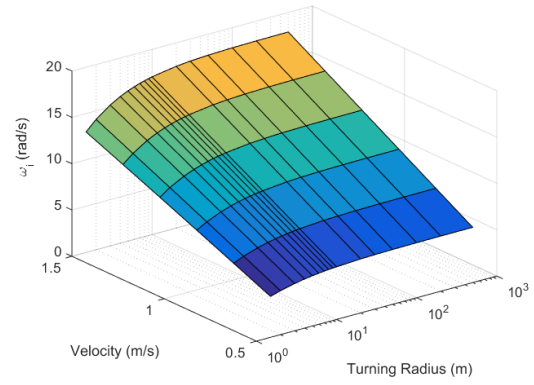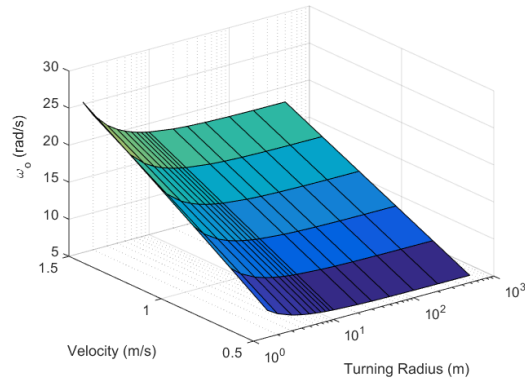
On Clay Soil

Figure 4.4 The solutions of a wheeled SUGV in skid steering on clay soil
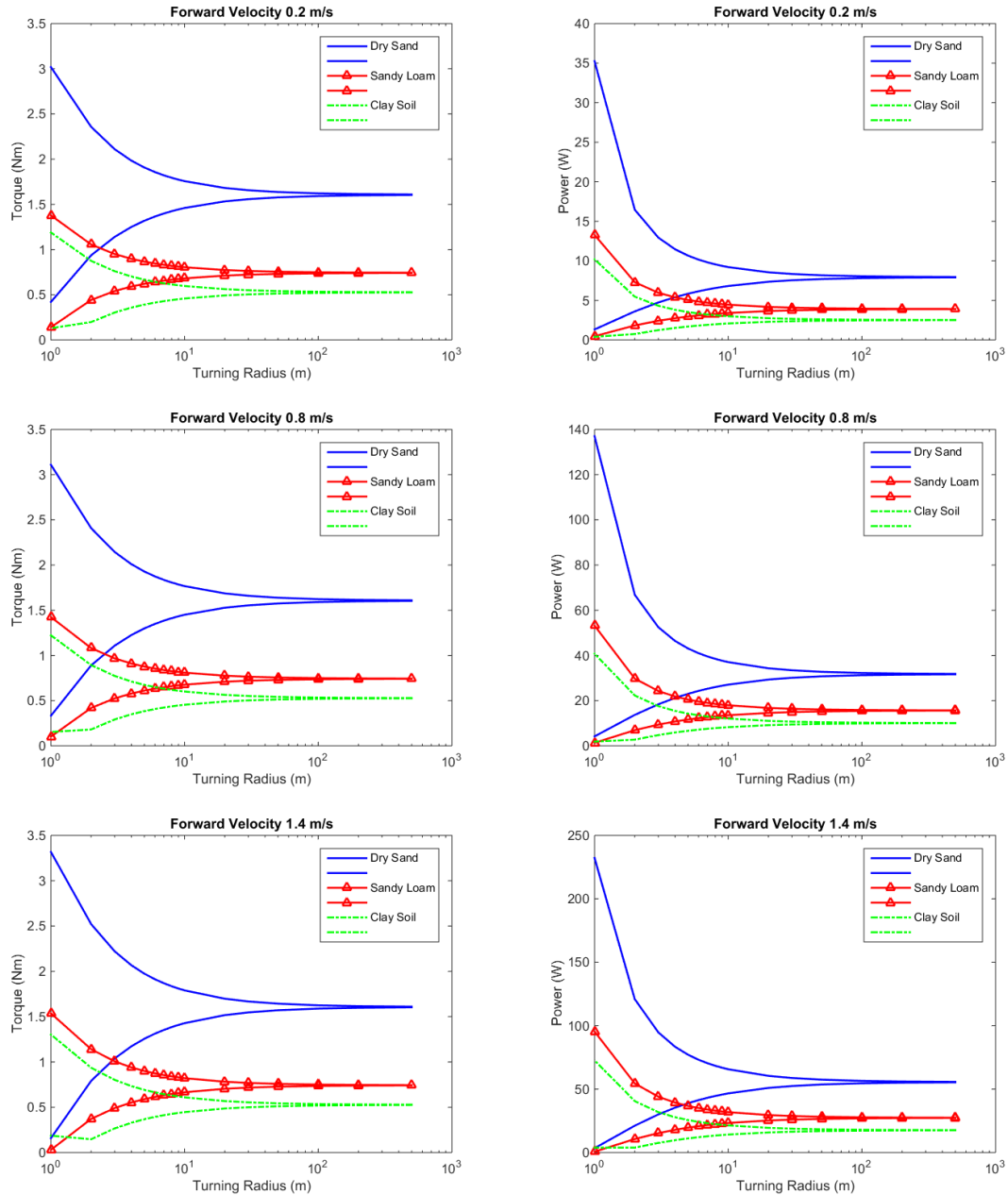
Figure 4.5 Torque and power on the outside and inside wheel shaft under various vehicle forward velocity and on 3 kinds of terrain

4.3 Summary

Beginning with Wong's general theory of skid steering on tracked vehicles, a skid steering model for wheeled SUGVs on deformable terrains was developed in this chapter. Numerical methods to achieve solutions in steady state were also presented. This model characterized the torque and power consumption of the outside and inside drive train under

different forward velocities and turning radii. Both Wong's skid steering model for tracked SUGVs developed in Chapter 3 and the skid steering model for wheeled SUGVs in this chapter are useful for the development of power management or power-conscious control systems by estimating the torque and power limit of the mobile robot driving on deformable terrains. However, the computation speeds need improvement. The average computation time for one solution is 1.88 seconds for the tracked vehicle model and 19.05 seconds for the wheeled vehicle model on a 4.4GHz core i7 desktop with 16GB DRAM. In order to improve the computation speeds, a simplified approach of skid steering on deformable terrains is required and a fast computation skid steering model for tracked SUGVs is developed in Chapter 5.

CHAPTER 5

A Fast Computation Skid Steering Model for Tracked SUGVs

Computation speed is very important for iterative vehicle design studies and embedded controls. In Chapters 3 and 4, skid steering models for tracked and wheeled SUGVs were developed based on Wong's theory. The numerical approach (Newton-Raphson method) used to solve the two models is too slow. In this chapter, a fast computation skid steering model for tracked SUGVs was developed. This model separated the overall solution process into computation-intensive and computation-light parts which made it possible to use the developed model in some cases that were not possible before.

5.1 The fast computation model

The basic idea of the fast computation model is that skid steering equations for tracked SUGVs mentioned in Chapter 3 can be separated into two parts: computation-intensive part (shear displacement - shear stress distribution on the track) and computation-light part (vehicle dynamic equations). Solving them together is time consuming. However, solving them separately will be much faster. For the computation-light part, we define 2 variables which are thrust on the outer track F_{xo} and thrust on the inner track F_{xi} instead of using s_0, ω_o and ω_i. As a result, the original equations from Chapter 3 reduce to two equations: longitudinal force balance and moment balance equation around z-axis. The reason is that the thrusts on outer and inner tracks directly relate to the torques on the sprocket and power consumption. For the computation-intensive part, 2 maps (offset of turning center s_0 and equivalent skid steering resistance coefficient μ_t) are first computed and stored in tables. The new set of equations is then:

$$F_{xo} + F_{xi} = \frac{mv^2}{R}\sin\beta + R_{to} + R_{ti}$$

$$(F_{xo} - F_{xi})\frac{B}{2} - (R_{to} - R_{ti})\frac{B}{2} + s_0\cos\beta\frac{mv^2}{R} = WL\mu_t \tag{5.1}$$

The skid steering resistance coefficient μ_t is defined as $\mu_t = (M_{To} + M_{Ti})/mgL$ where M_{To} and M_{Ti} are moments of turning resistance due to lateral force on the outer and inner track. And $\beta = \tan^{-1}(s_0/R)$. The two maps μ_t and s_0 in

Figure 5.1 can be generated from the previous chapters.

Solutions for outer track thrust F_{xo} and inner track thrust F_{xi} can then be obtained from

$$F_{xo} = \frac{A_1 + A_2}{2}$$

$$F_{xi} = \frac{A_1 - A_2}{2}$$

$$A_1 = \frac{mv^2}{R}\sin\beta + R_{to} + R_{ti} \tag{5.2}$$

$$A_2 = \left(WL\mu_t + (R_{to} + R_{ti})\frac{B}{2} - s_0\cos\beta\frac{mv^2}{R}\right)\frac{2}{B}$$

For solving the angular velocity of the sprocket ω_o and ω_i, single track-terrain interaction model is used to calculate its slip ratio with a corresponding tractive effort $F_{xo,i}$.

$$F_{xo,i} = (Ac + \sigma_{o,i}\tan\phi)\left[1 - \frac{K}{sL}(1 - e^{-sL/K})\right] \tag{5.3}$$

where $\sigma_{o,i}$ is the pressure on the outside and inside of the track and s is slip ratio on either outside or inside track.
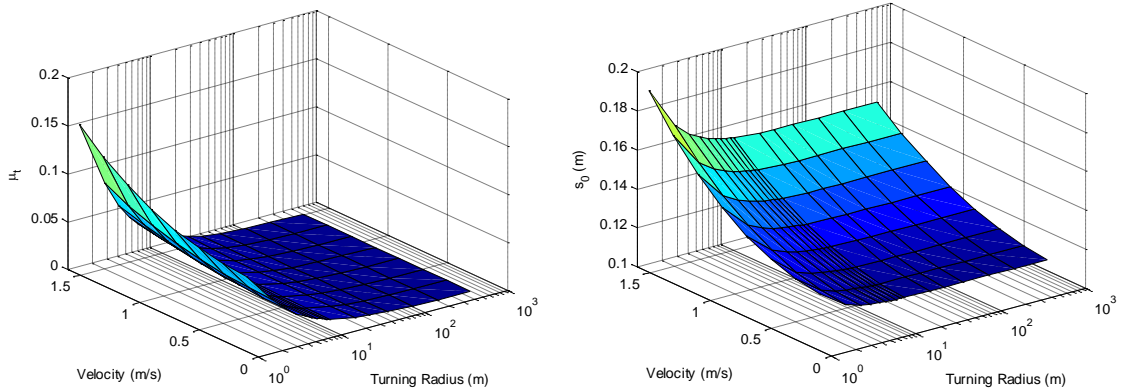
Figure 5.1 The two pre-generated maps of μ_t and s_0

5.2 The comparison between the fast computation model and Wong's model

Using the same parameters used in Chapter 3, we obtain the results of the simplified model as shown in Figure 5.2 with the comparison of the model in chapter 3.
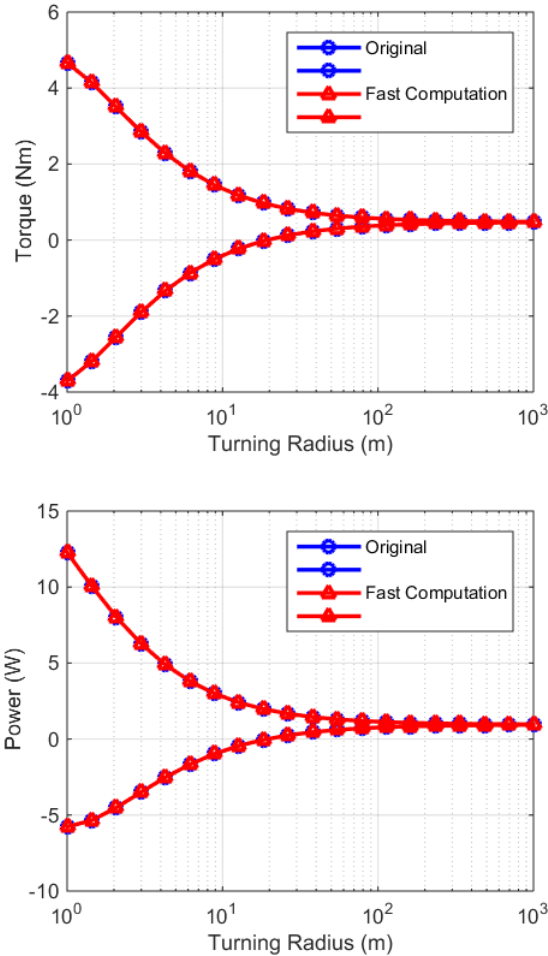
Figure 5.2 Sprocket torque and power consumption comparison between the original track model and the fast computation model

From Figure 5.2 we can see that the fast computation model produces results very similar to the original model developed in chapter 3. The computation time is reduced by a factor of 3,000 based on an Intel i7 quad-core 4.4GHz 16GB Ram desktop. However, there is slight difference on torque and power consumption when the turning radius is small. The explanation is that when the turning radius is small, the tractive effort generated on the contact surface comes from both lateral and longitudinal shear displacement. But in the simplified model the calculation of lateral and longitudinal shear displacement is

eliminated, thus making the longitudinal tractive effort larger than that of the original model with the same slip ratio.

This model is useful for the controller in the real world with the assumption that slight change in the vehicle parameters or the soil values will not alter the two pre-generated maps a lot. Figure 5.3 and Figure 5.4 show the comparison of torque and power consumption between the fast computation model and the original model with slight change in the tread of the vehicle and the soil shear modulus K respectively.
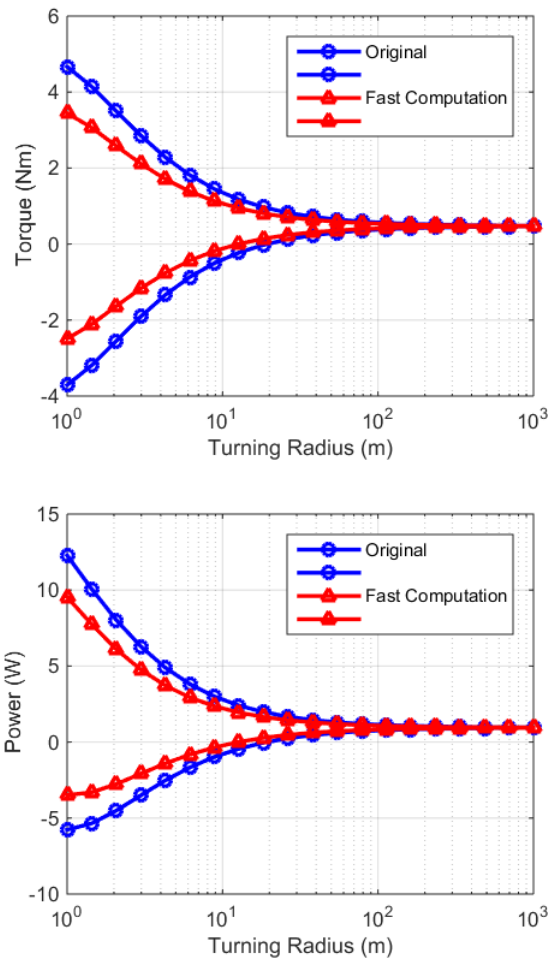
Figure 5.3 Sprocket torque and power comparison between the original model and the fast computation model with tread of the vehicle changing from 0.4 m to 0.6 m
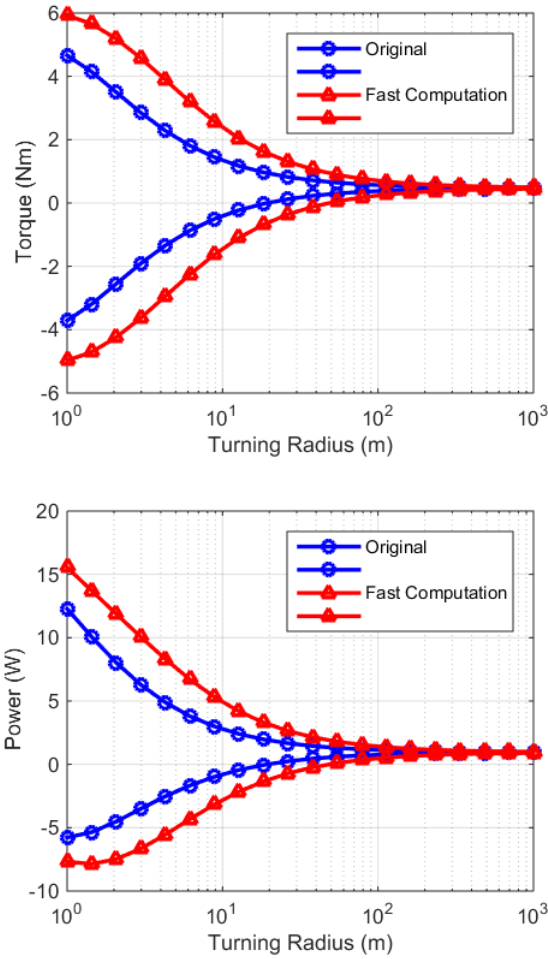
Figure 5.4 Sprocket torque and power comparison between the original model and the
fast computation model with soil K value changing from 0.075m to 0.04m

From Figure 5.3 and Figure 5.4, we can see that the changes in the tread of the
vehicle and soil shear modulus K lead to large errors between the original model and the
fast computation model. In the small radius turning case, these errors can go to almost 40%.
This means that the changes of the tread of the vehicle or the soil shear modulus value are
critical in the change of sprocket torque and power consumption. The fast computation
model with un-updated μ_t and s_0 maps cannot represent the real case. From these graphs
we can draw a conclusion that the fast computation model is not robust enough for the
change of the vehicle or the soil.

5.3 Summary

A fast computation skid steering model for tracked SUGVs was developed in this chapter by separating the governing equations into computation-intensive and computation-light parts. This fast computation model can be useful for both real-time applications, and for robotic design and sizing, when a large number of design parameters are looped through. The computation efficiency of this model greatly improved in contrast with Wong's model in Chapter 3. However, there emerged another concern, the robustness. This fast computation skid steering model for tracked SUGVs is only useful when there are two pre-generated maps for μ_t and s_0 which are the coefficient of lateral friction and the offset of the turning center. And any change in the vehicle parameter or terrain value will alter this map. In order to overcome the robustness problem of this fast computation model while maintaining high computation speed, a new finite element skid steering (FESS) model for both tracked and wheeled SUGVs in steady state on deformable terrains is developed and explained in Chapter 6.

CHAPTER 6
Finite Element Skid Steering (FESS) Model

In Chapter 3, three widely used skid steering models on tracked vehicles were analyzed. Although all of these models are capable of estimating mobility and power consumption on skid steering, they all have some drawbacks, either in terms of model accuracy and range of fidelity, or in computation speed. In Chapter 4, Wong's skid steering model was extended to wheeled vehicles, further considering the radial wheel-terrain contact surface and the coupling effect between slip ratio and sinkage. In this chapter, a universal skid steering model, the finite element skid steering (FESS) model on deformable terrains, was developed. It addressed the drawbacks of the previous models identified above by developing a new approach to calculate the shear displacement and with techniques such as discretizing the contact surface and quadratic approach of the normal and shear stress at the contact surface. Moreover, one of the features of this model is that it combines the track and wheel cases and can be applied to study the skid steering behavior of both wheeled and tracked vehicles.

6.1 Another look at the shear displacement

In the theory of terramechanics, the soil is usually assumed to be acting as a group of cantilever beams, while the running gear (either track or wheel) is assumed to be rigid. When the running gear contacts the soil, it is assumed that points on the running gear stick to the top of the soil and when there is relative shear velocity between the running gear and soil, shear displacement accumulates with time. Furthermore, shear stress grows with the shear displacement. When the shear displacement reaches a certain value, the soil fails and for most of the terrains, shear stress is saturated at that point.

In the previous chapters, we learned that shear displacement is very important in the skid steering modeling. However, it is difficult to calculate shear displacement in skid

74

steering due to the coupling effect of longitudinal and lateral directions. Wong proposed a method discussed in Chapter 3 (Eq. (3.8) - Eq. (3.11)) to calculate shear displacement. Although it is accurate, yet it is slow in computation. The FESS model in this chapter finds an alternative way to calculate the shear displacement that is both fast and accurate.

When a vehicle skid steers, there are two types of movements for any point on the contact surface. One is the relative movement occurring along the track or the wheel. The other is the carrying movement of the vehicle. Take the track model as an example. This kinetics is shown in Figure 6.1. For a specific point (x, y) in the global frame (X, Y) on the contact surface between the track and the soil, the point starts the contact from the front end of the track. And if the current time is labeled as $t = 0$, then for the point (x, y) it starts to contact the soil at $t = -T$, represented by dashed lines on Figure 6.1. The front end of the track is marked as point (x_0, y_0). Thus the distance between (x, y) and (x_0, y_0) is the shear displacement for point (x, y).
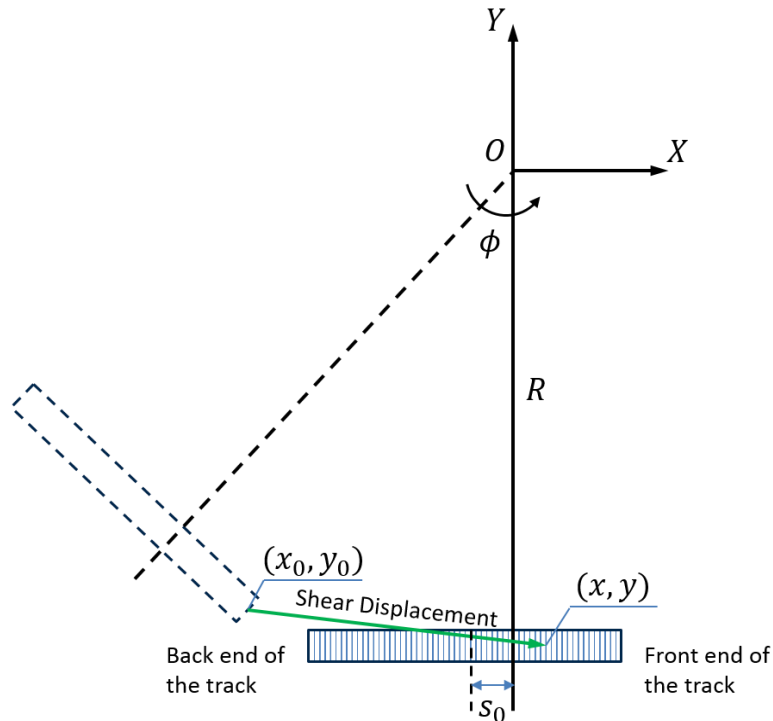
Figure 6.1 The kinetics of a track moving on the soil

The relative movement can be described by the following equation

$$\begin{bmatrix} x \\ y \end{bmatrix} = \begin{bmatrix} \dfrac{L}{2} - s_0 - \omega r t \\ -R \end{bmatrix} \qquad (6.1)$$

75

where L is the track length, s_0 is the offset of the turning center, ω is the angular velocity of the sprocket, r is the radius of the sprocket, and R is the turning radius of the track.

The carrying movement can be described in the following equation

$$\begin{bmatrix} x_0 \\ y_0 \end{bmatrix} = \begin{bmatrix} \cos\phi & \sin\phi \\ -\sin\phi & \cos\phi \end{bmatrix} \begin{bmatrix} \frac{L}{2} - s_0 \\ -R \end{bmatrix} \tag{6.2}$$

where ϕ is the turning angle for the vehicle.

ϕ is calculated from the following

$$\phi = \dot{\phi} \cdot t \tag{6.3}$$

where $\dot{\phi}$ is the yaw rate of the vehicle.

The magnitude of the shear displacement in the global frame for a point (x, y) on the contact surface is described as

$$J = \left\| \begin{bmatrix} x \\ y \end{bmatrix} - \begin{bmatrix} x_0 \\ y_0 \end{bmatrix} \right\| \tag{6.4}$$

$J_x = x - x_0$ and $J_y = y - y_0$ are the shear displacements in the x and y directions, respectively.

6.2 Discretizing the track-terrain contact surface

To accelerate the calculation speed, the track-terrain contact surface can be discretized, i.e. we can evenly divide the contact surface along the track into n segments. Thus the step time can be defined with the movement of each segment.

$$\Delta t = \frac{L}{n\omega r} \tag{6.5}$$

Figure 6.2 shows an example of the shear displacement of a track in Wong's model at the contact surface. It can be seen from this figure that both longitudinal and lateral shear displacements vary little on the lateral direction of the track. Thus we sample the shear displacement only on the center line of the track. Therefore the shear displacement of the kth element ($k \in [0, n]$) on the outside and inside tracks can be written as

$$J_o(k) = \left\| \begin{bmatrix} \frac{L}{2} - s_0 - \frac{kL}{n} \\ -R - \frac{B}{2} \end{bmatrix} - \begin{bmatrix} \cos\frac{k\dot{\phi}L}{n\omega_o r} & \sin\frac{k\dot{\phi}L}{n\omega_o r} \\ -\sin\frac{k\dot{\phi}L}{n\omega_o r} & \cos\frac{k\dot{\phi}L}{n\omega_o r} \end{bmatrix} \begin{bmatrix} \frac{L}{2} - s_0 \\ -R - \frac{B}{2} \end{bmatrix} \right\| \tag{6.6}$$

76

$$J_i(k) = \left\| \begin{bmatrix} \frac{L}{2} - s_0 - \frac{kL}{n} \\ -R + \frac{B}{2} \end{bmatrix} - \begin{bmatrix} \cos\frac{k\dot{\phi}L}{n\omega_i r} & \sin\frac{k\dot{\phi}L}{n\omega_i r} \\ -\sin\frac{k\dot{\phi}L}{n\omega_i r} & \cos\frac{k\dot{\phi}L}{n\omega_i r} \end{bmatrix} \begin{bmatrix} \frac{L}{2} - s_0 \\ -R + \frac{B}{2} \end{bmatrix} \right\|$$
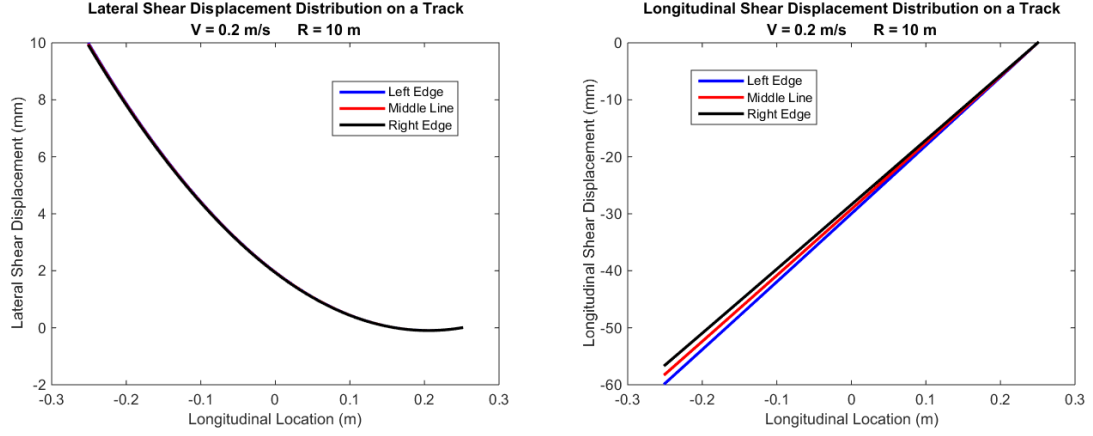
Figure 6.2 An example of the shear displacement of a track at the contact surface

According to the shear stress-shear displacement relationship explained in Chapter 2, the shear stress on the contact surface is

$$\tau_{xo}(k) = \tau_{omax}\left(1 - e^{-\frac{J_o(k)}{K}}\right)\frac{J_{xo}}{J_o}$$

$$\tau_{yo}(k) = \tau_{omax}\left(1 - e^{-\frac{J_o(k)}{K}}\right)\frac{J_{yo}}{J_o}$$

$$\tau_{xi}(k) = \tau_{imax}\left(1 - e^{-\frac{J_i(k)}{K}}\right)\frac{J_{xi}}{J_i} \tag{6.7}$$

$$\tau_{yi}(k) = \tau_{imax}\left(1 - e^{-\frac{J_i(k)}{K}}\right)\frac{J_{yi}}{J_i}$$

The longitudinal and lateral forces and moments are calculated based on trapezoidal numerical integration of the shear stress on each element. Once all the forces and moments at the contact surface have been calculated, the same Newton-Raphson numerical method described in Chapter 3 is used and the unknown variables $(s_0, \omega_o, \omega_i)$ and the dynamics of the skid steering system can then be solved.

6.3 Discretizing the wheel-terrain contact surface

When the FESS model is used for a wheeled vehicle, the only major difference from the tracked vehicle model is the contact area. In the tracked vehicle model, we assume a flat contact surface and uniform normal pressure, while in the wheeled vehicle model the contact surface is radial and the normal pressure is not uniformly distributed. Because of the complexity of the radial contact surface and non-uniform normal pressure, sinkage and slip ratio are coupled together. We assume that the effect of slip ratio on the contact area and normal and shear stresses is small. Thus the slip ratio and sinkage are decoupled. To simplify the shear displacement calculation, it is assumed that the contact surface is flat but still has non-uniform normal pressure and shear stress according to the radial contact surface. Some research has been done recently on the simplification of the contact surface pressure. Shibly (2005) and Jia (2012) have developed simplified single wheel-terrain interaction models to lower the computation burden [45] [47]. In Shibly's model the normal and shear stress on the contact surface are assumed to be linear. Jia uses the quadratic approximation method for both normal and shear stresses to significantly improve the model accuracy compared with Shibly's model. In this study, the quadratic approximation for normal stress is used in the skid steering model for wheeled SUGVs.

6.3.1 Quadratic approximation for normal stress

In the wheel-terrain interaction case, three angles are introduced in Chapter 2, which are the front contact angle θ_f, the rear exit angle θ_r, and the angle corresponding to the maximum normal stress θ_m. In the quadratic approximation, two new angles are introduced, which are the front medium angle θ_{fm} and the rear medium angle θ_{rm}. These two angles can be computed as

$$\theta_{fm} = \frac{\theta_f + \theta_m}{2} \qquad \theta_{rm} = \frac{\theta_r + \theta_m}{2} \qquad (6.8)$$

The quadratic form of the normal stress can be derived as

$$\tilde{\sigma}(\theta) = a_i\theta^2 + b_i\theta + c_i \quad (\theta_i^l \leq \theta \leq \theta_i^u) \qquad (6.9)$$

with

$$\begin{bmatrix} a_i \\ b_i \\ c_i \end{bmatrix} = \begin{bmatrix} \theta_m^2 & \theta_m & 1 \\ \theta_{im}^2 & \theta_{im} & 1 \\ \theta_i^2 & \theta_i & 1 \end{bmatrix}^{-1} \begin{bmatrix} \sigma_m \\ \sigma_{im} \\ \sigma_i \end{bmatrix} \tag{6.10}$$

$$\left(\begin{matrix} i = f, r \\ \theta_r^l = \theta_r; \quad \theta_r^u = \theta_f^l = \theta_m; \quad \theta_f^u = \theta_f \end{matrix} \right)$$

where the subscript i indicates the front or rear region.

The transformation between the x-axis on the skid steering motion plane and the θ-axis on the single wheel can be written as

$$x = r \sin \theta \mp \frac{wb}{2} - s_0 \tag{6.11}$$

where r is the wheel radius, wb is the wheel base, s_0 is the offset of the turning center, and $\mp$ represents the rear or the front wheel.

6.4 The FESS model for tracked and wheeled SUGVs

The new skid steering model for both tracked and wheeled SUGVs in steady state on deformable terrains is developed. The overview of the structure is shown in Figure 6.3 below.

A given mission profile (cycle profile, including turning radius R, forward velocity V, terrain parameters, etc., and vehicle parameters, including wheel or track configuration, mass, size, etc.) is the input of the FESS Model. In the FESS Model, the first step is to determine the vertical load on each side of the drivetrain. This can be done using Eq. (6.12), shown below. It is assumed that the center of gravity collocates with the center of the vehicle. L_o is the load on the outside of the vehicle, L_i is the load on the inside of the vehicle, and h is the height of the center of gravity.
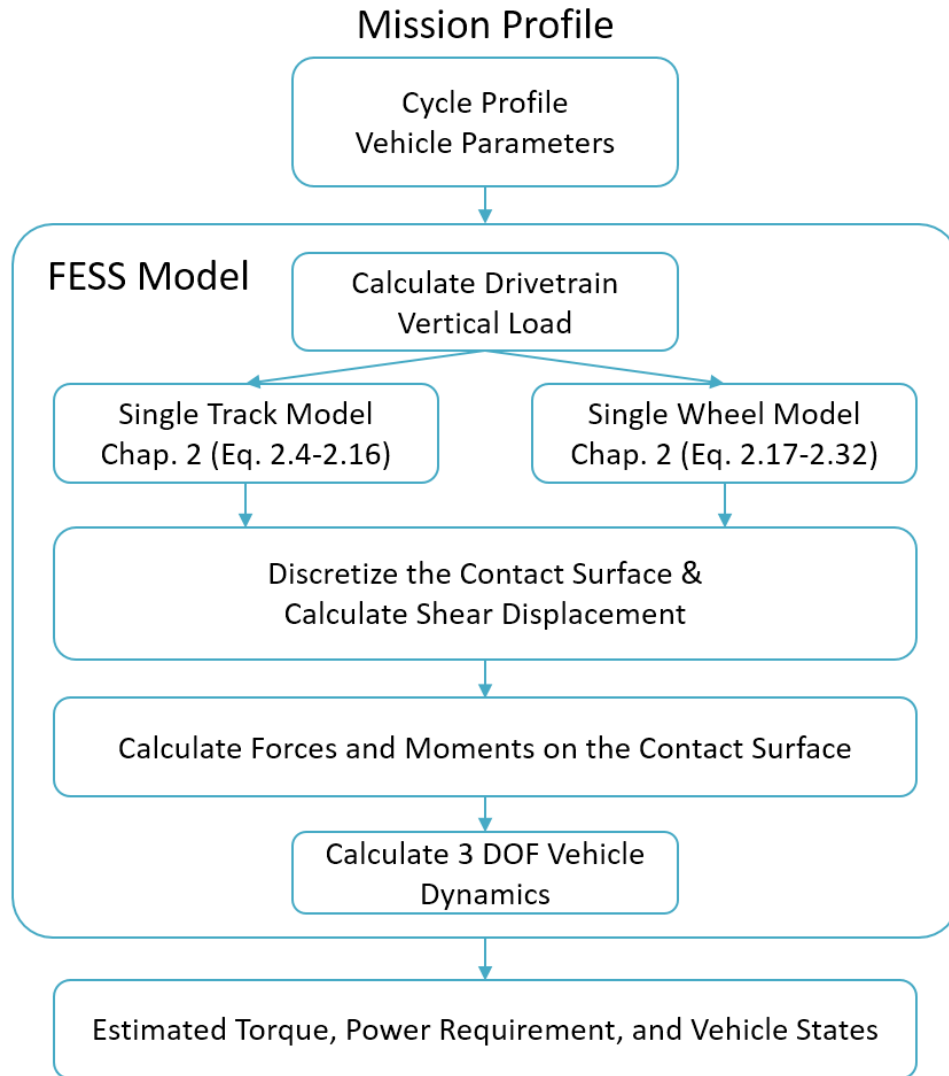
Figure 6.3 Overview structure of the FESS Model

$$L_o = \frac{W}{2} + \frac{mV^2}{BR}h$$

$$L_i = \frac{W}{2} - \frac{mV^2}{BR}h$$
(6.12)

The second step in the FESS Model is using either the single track-terrain interaction model or the single wheel-terrain interaction model developed in Chapter 2 to calculate the normal pressure and compaction resistance for the tracked configuration or the normal pressure and the entry and exit angles and compaction resistance for the wheeled configuration. For the tracked configuration, the pressure on the outside and inside tracks can be calculated with $p_o = L_o/(bL)$ and $p_i = L_i/(bL)$, if uniform pressure is assumed.

The track compaction resistance can be calculated using Eq. (2.10). For the wheeled configuration the load on each wheel is input into the single wheel model. The corresponding front contact angle θ_f, the rear exit angle θ_r, and the medium angle θ_m and wheel compaction resistance can be determined from Eq. (2.28). The calculation of normal stress on the contact surface is approximated by the quadratic equation in Eq. (6.10) for fast computation.

The third step in the FESS Model is discretizing the contact surface and calculating shear displacement by using Eq. (6.4). The forth step is calculating the shear stress with shear displacement and results from single track-terrain model and single wheel-terrain model. The fifth step is integrating the shear stress on the contact surface and inputting them into the 3 degrees of freedom vehicle dynamics model (Eq. (3.18)). With the Newton-Raphson iteration method, the problem in steady state is solved.

Figure 6.4 and Figure 6.5 are two example solution sets of s_0, ω_o and ω_i with the same parameters used in Chapter 3 and Chapter 4.
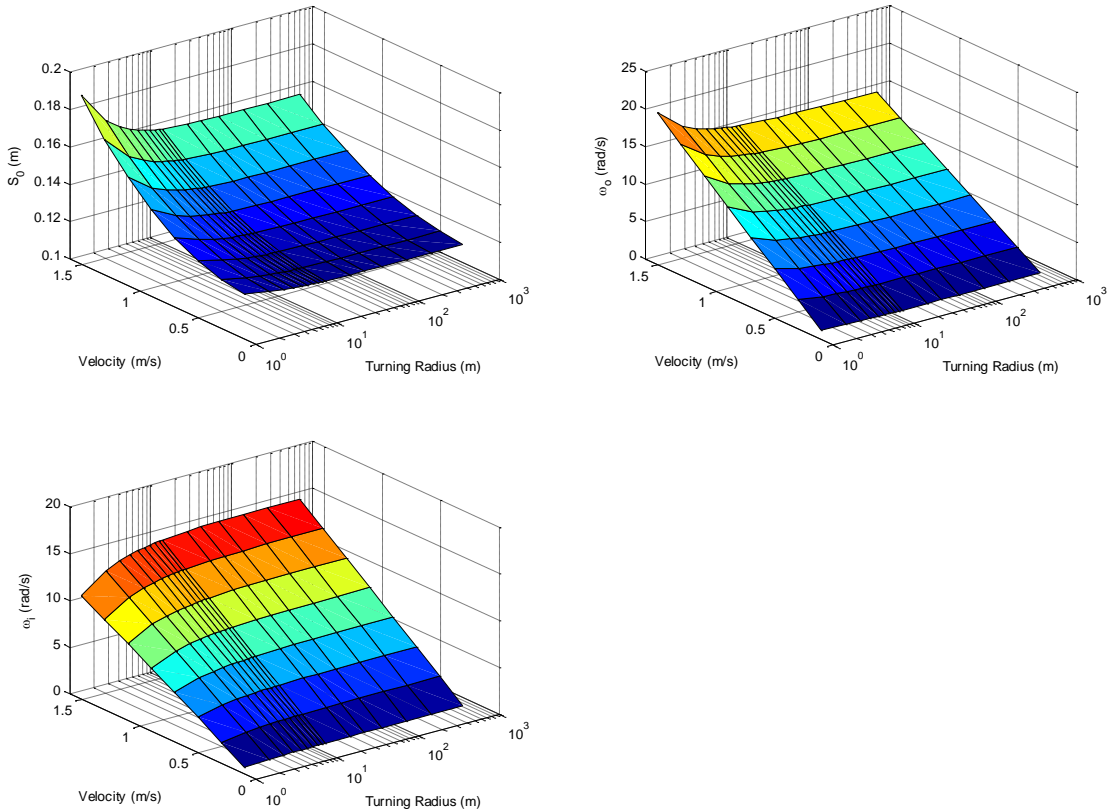
Figure 6.4 Solutions of s_0, ω_o and ω_i in the FESS track model
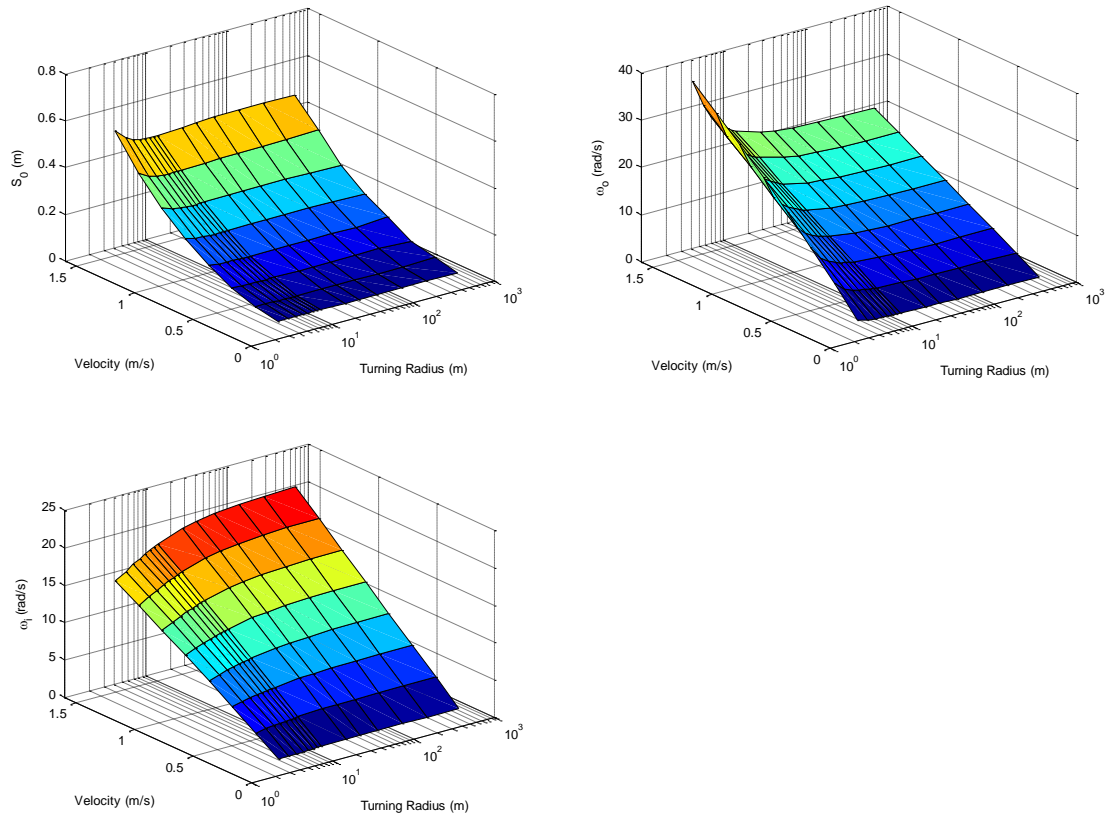
Figure 6.5 Solutions of s_0, ω_o and ω_i in the FESS wheel model

Compared with Wong's model for tracked SUGVs in Chapter 3, the solving time has been drastically reduced. For the track cases, the solving time for 8×16 solving points is reduced from 244.8 seconds (Wong's Track Model) to 3.1 seconds (FESS Model), while for the wheel cases, the solving time for 8×16 solving points is reduced from 2777.2 seconds (Model in Chapter 4) to 14.3 seconds (FESS Model). Figure 6.6 to Figure 6.11 show the differences between Wong's track model and the FESS track model, and between the wheel model developed in Chapter 4 and the FESS wheel model.
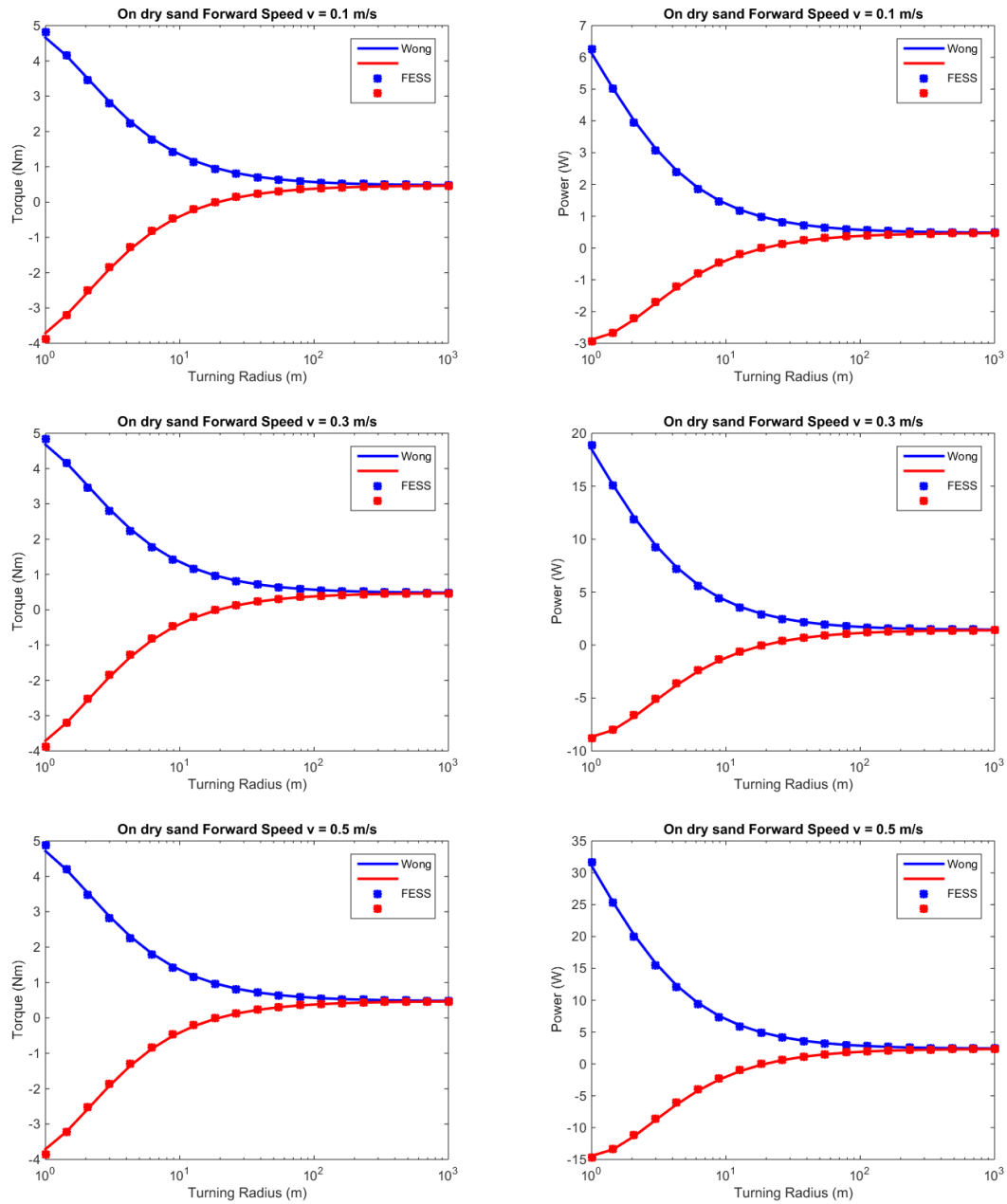
Figure 6.6 Sprocket torque and power consumption comparison between the Wong track model and the FESS track model on dry sand

83
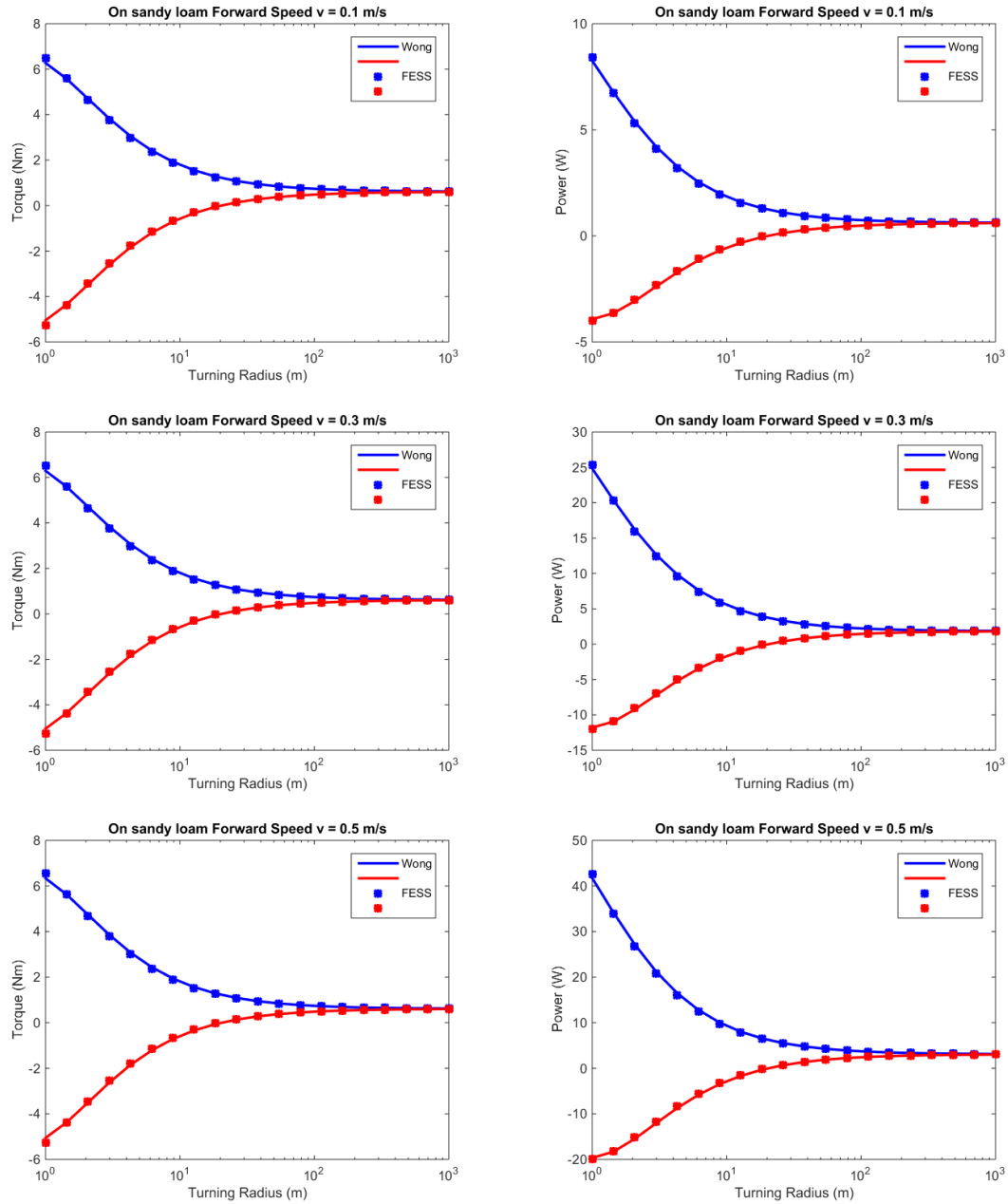
Figure 6.7 Sprocket torque and power consumption comparison between the Wong track model and the FESS track model on sandy loam
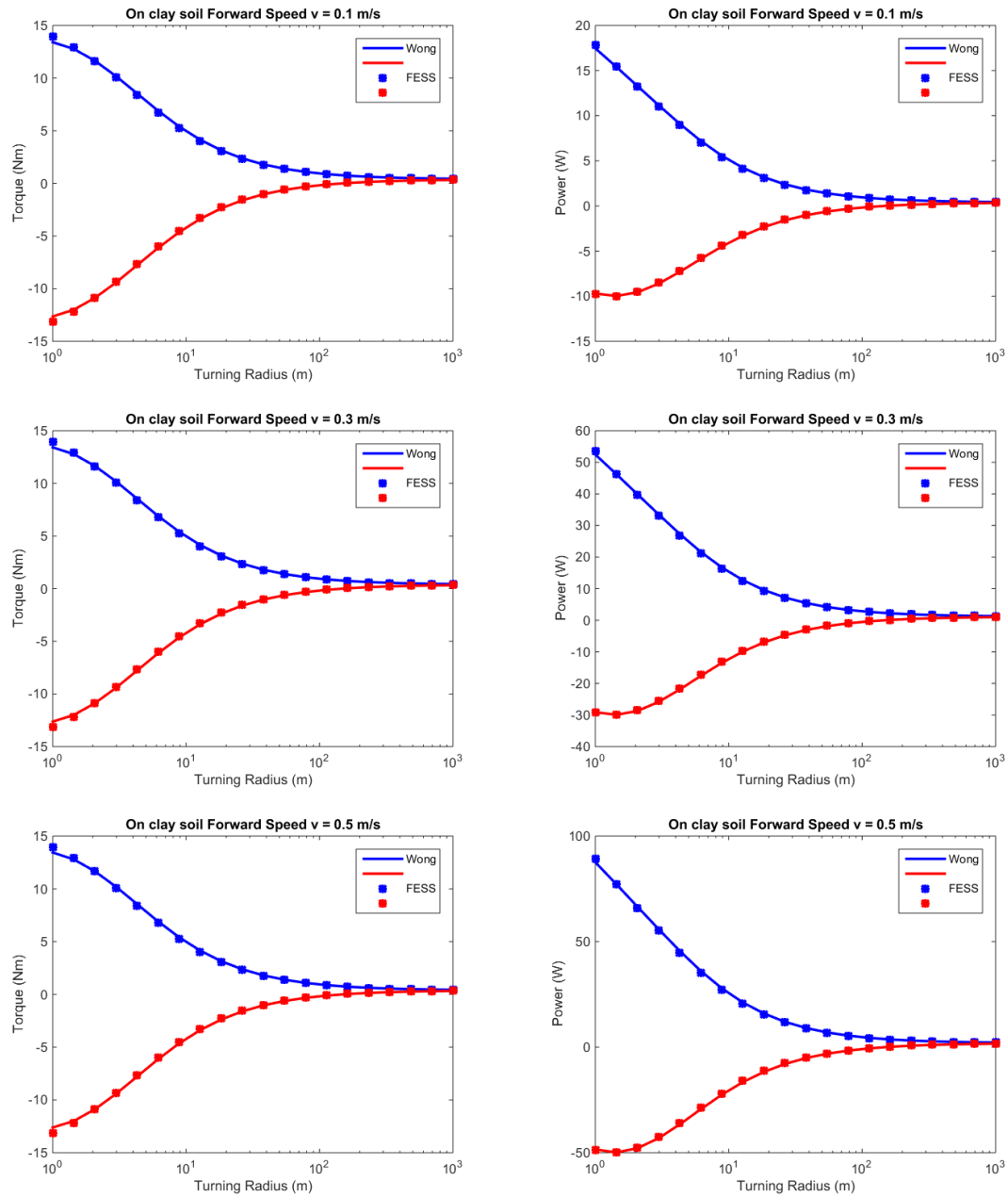
Figure 6.8 Sprocket torque and power consumption comparison between the Wong track model and the FESS track model on clay soil
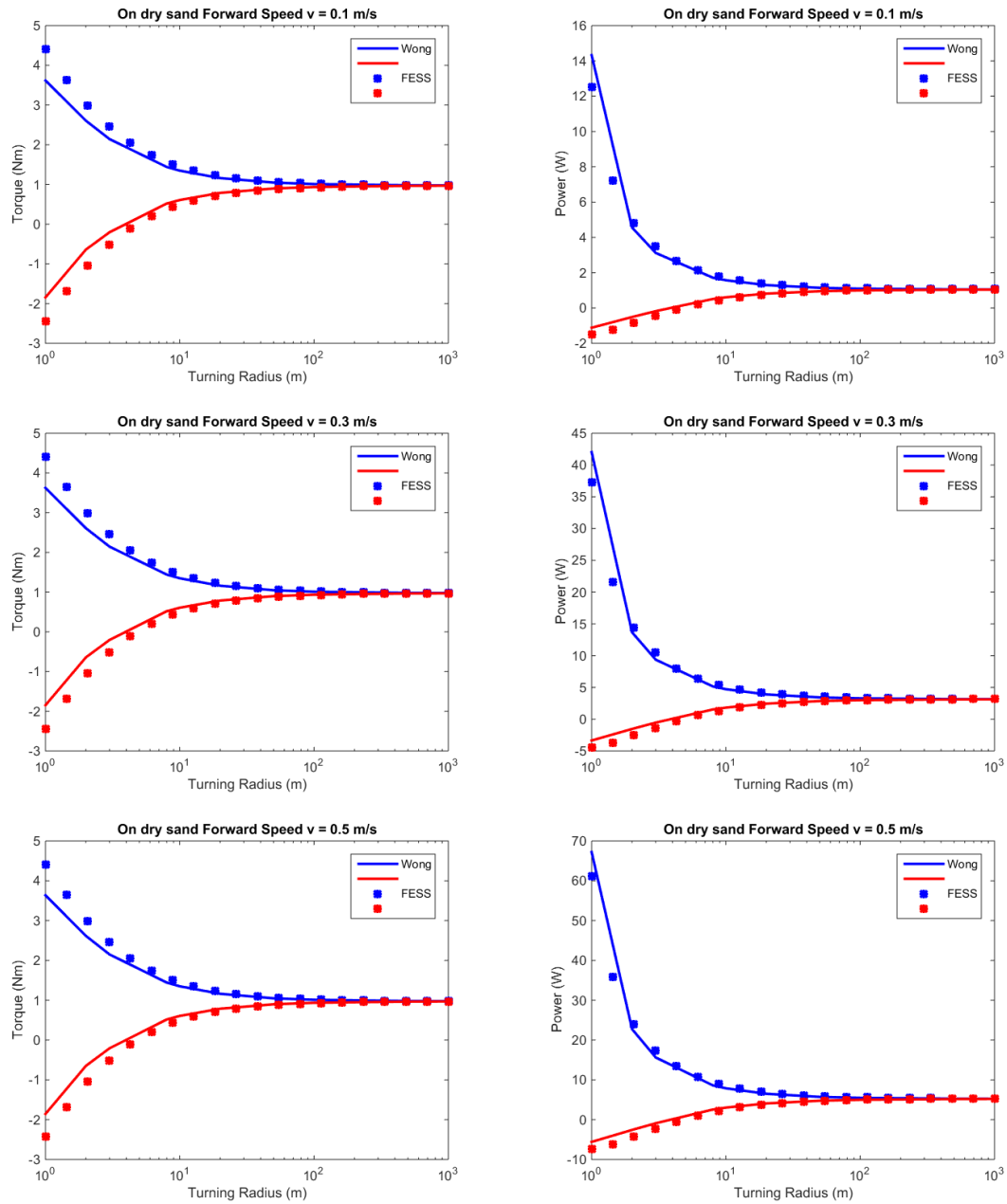
Figure 6.9 Sprocket torque and power consumption comparison between the Wong wheel model and the FESS wheel model on dry sand
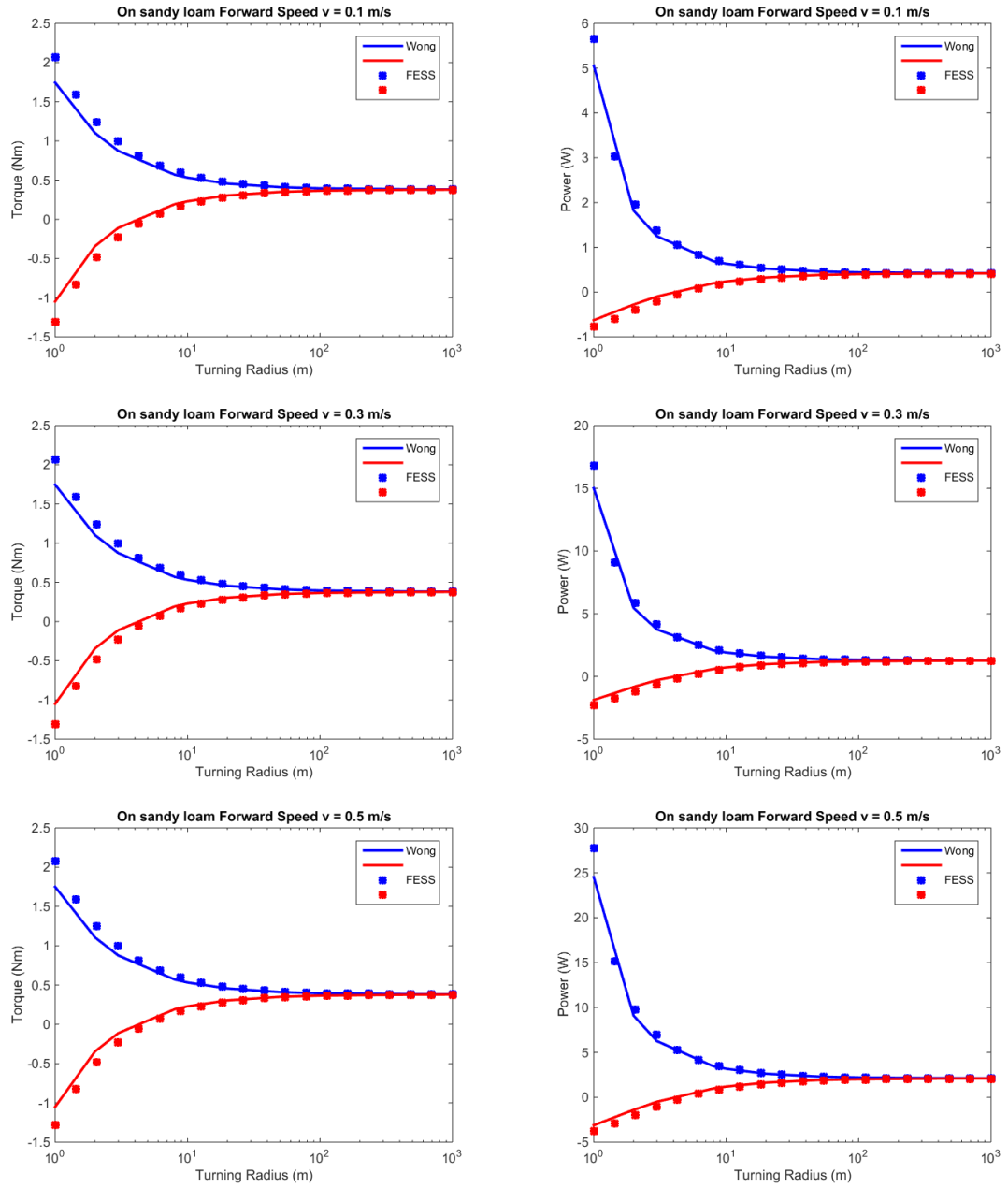
Figure 6.10 Sprocket torque and power consumption comparison between the Wong wheel model and the FESS wheel model on sandy loam
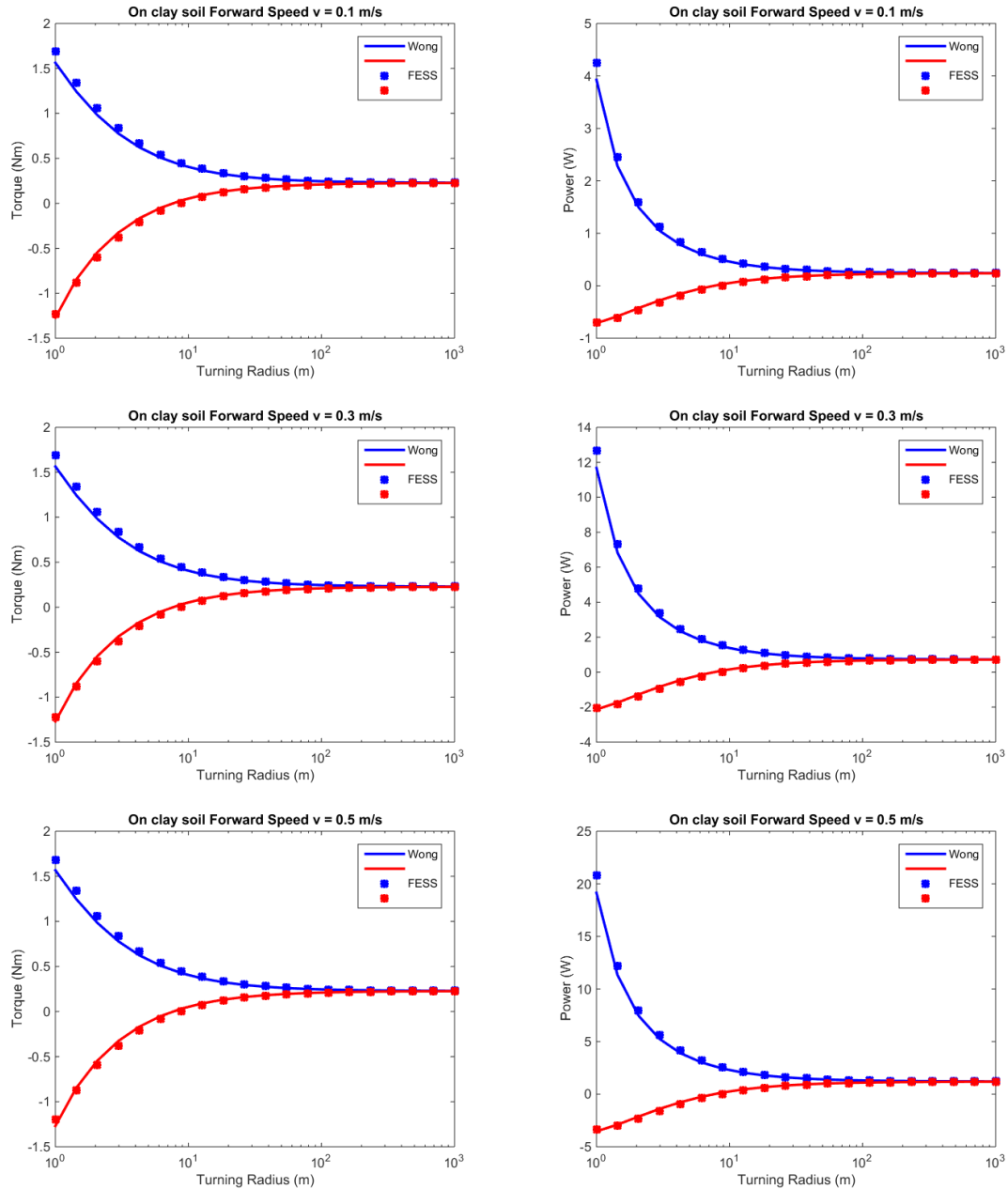
Figure 6.11 Sprocket torque and power consumption comparison between the Wong wheel model and the FESS wheel model on clay soil

From Figure 6.6 to Figure 6.8, it can be seen that the FESS model in the tracked configuration matches Wong's track model in torque and power consumption estimation on all 3 soils. From Figure 6.9 to Figure 6.11, it can be seen that the FESS model in the wheeled configuration is close to the wheel model developed in Chapter 4 at big turning radii on all 3 soils. However, with small turning radii these two models have small differences on torque and power value. The reason is the differences in the assumptions of

the model. In the FESS wheel model the contact area is assumed to be flat, which is an approximation that we think is responsible for the small difference in model outputs.

The average computation time for the track case and wheel case is 0.37 second and 1.68 seconds respectively based on an Intel core i7 4 GHz CPU with 16GB ram. The sampling rate of the onboard controllers that use Steeds or ICR models ranges from 5 Hz to 1000 Hz [37] [38] [39] [41] [49]. Although the computation speed of the FESS model is still not fast enough for onboard applications, the FESS model shows its big improvement of the computation efficiency over the Wong's method.

Possible improvements of the calculation speed of the FESS model includes better solving method and further simplification of the normal and shear stress calculation on the contact surface, especially for the wheel-terrain interaction. The FESS model uses Newton-Raphson numerical method to solve the vehicle dynamics. Faster numerical methods will be definitely beneficial in improving calculation efficiency. The current calculation of the normal and shear stress of the vehicle-terrain interaction, especially for the wheel case, is still complicated. Further simplification of these calculations with appropriate assumptions for SUGVs can increase the computation speed of the vehicle-terrain interaction. If the closed form solution of the system can be found, it will drastically increase the computation speed and achieve comparable computation efficiency against Steeds or ICR models.

6.5 Summary

In this chapter, a finite element skid steering (FESS) model was developed, which could be used for both tracked and wheeled SUGVs. Similar to Wong's model, the FESS model considered the shear displacement on the contact surface, and the shear stress was calculated by the shear stress-shear displacement relationship studied in Chapter 2. This model proposed a new method to analyze shear displacement and simplifications at the contact surface, both of which drastically helped to increase the computation speed over that of Wong's model. Simulations indicated that the difference between the results of the FESS model and Wong's model was small. Experiments were performed to validate the FESS model for both tracked and wheeled SUGVs in the following chapter.

CHAPTER 7

Test Robot and Experimental Validation

In Chapter 6, a new skid steering model (FESS Model) for both tracked and wheeled SUGVs was developed. It demonstrated faster computation speed than Wong's model but had comparable accuracy. In this chapter, a 6-wheel-drive wheel/track interchangeable SUGV was designed and built as a test robot to validate the FESS Model. This chapter was organized as follows. Section 7.1 described the design and the fabrication of the test robot. Section 7.2 described measuring the internal power consumption of the test robot. Section 7.3 described the design and results of the field experiments.

7.1 The 6-wheel-drive track/wheel interchangeable skid steering SUGV

In order to validate the FESS model, a 6-wheel-drive track-wheel interchangeable skid steering SUGV, shown in Figure 7.1, is designed and built.
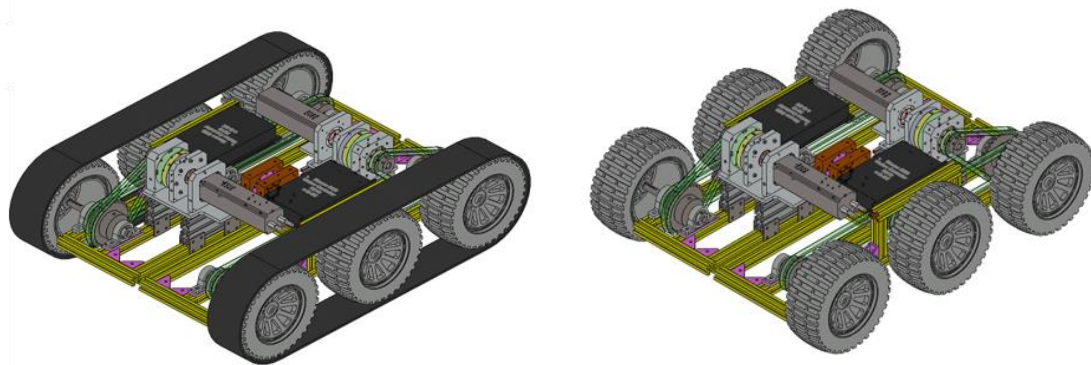
Figure 7.1 The 6-Wheel-Drive Track-Wheel Interchangeable Skid Steering SUGV

7.1.1 Mechanical system

The test robot can be tracked or wheeled interchangeably. The chassis has 6 wheels. If the sprockets and tracks are installed, it becomes a tracked vehicle. If wheels are installed on the axles, it becomes a wheeled vehicle. The powertrain and chassis structure are shown

in Figure 7.2. The chassis is made of aluminum frames, which helps to reduce the weight. Moreover, the aluminum frames are easy to machine and assemble. The total operating weight of this SUGV is around 30 kg. It is 650 mm in length and 500 mm in width.

This SUGV is equipped with two Maxon EC-45 300-Watt motors with DES 70/10 controllers to drive the left and right sides separately. All output shafts on the same side are connected by chain to achieve all-wheel-drive. Therefore, all the wheels on each side have the same angular speed and almost the same slip ratio. The gear-train reduction ratio is 12:1, achieved by a 4.8:1 high efficiency planetary gear and 2.5:1 roller-sprockets. The reason to use roller-chains instead of timing belts is the higher reliability and higher efficiency of roller-chains. The two motors and their gear trains are installed symmetrically, and the CG of the vehicle is on the centerline of the vehicle.
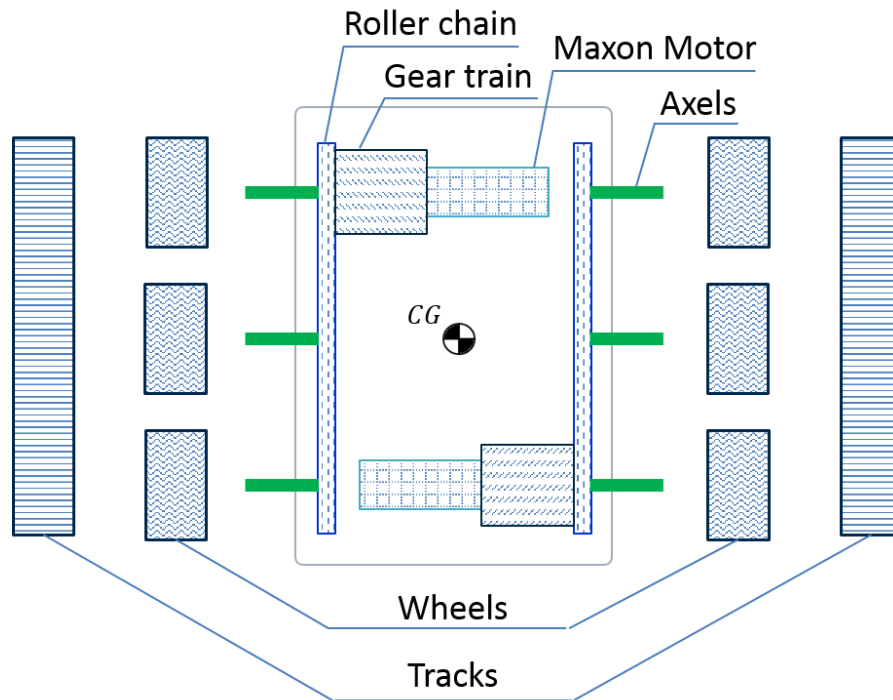
Figure 7.2 Powertrain and chassis structure of the test robot

The wheels and tracks are shown in Figure 7.3. We use HPI BAJA wheel sets, which are suitable for off-road driving. The tracks are made of standard rubber with grouser on the surface and the sprockets are made of rigid plastic. Both configurations have the same width and radius.
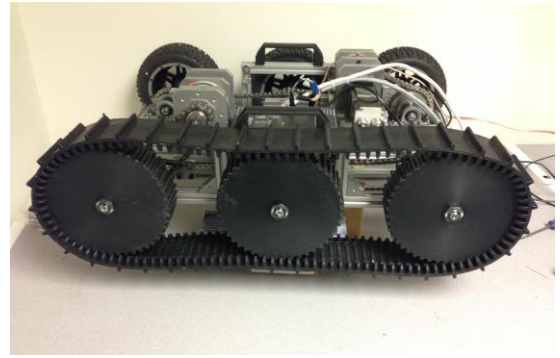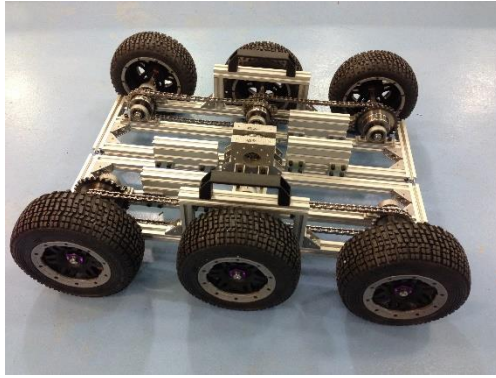
Figure 7.3 HPI BAJA wheel sets and track sprocket sets

The chassis of the vehicle consists of two separate aluminum frames connected by a pan-cake suspension system, highlighted by a red circle in Figure 7.4. This suspension is chosen for its mechanical simplicity compared with independent suspension on each axle. Although this suspension is not independent, it separates left and right drive-train on the ground, as shown in Figure 7.5. When the left side of the drive-train drives over an obstacle, the right drive-train can still maintain good contact with the ground.
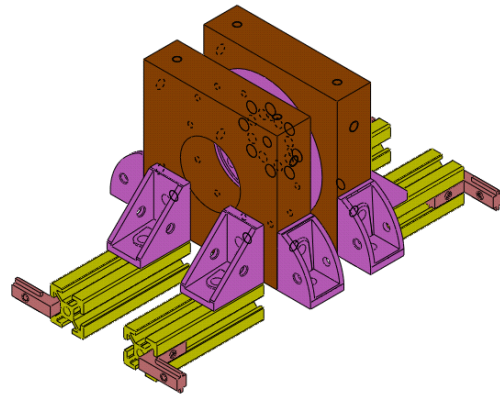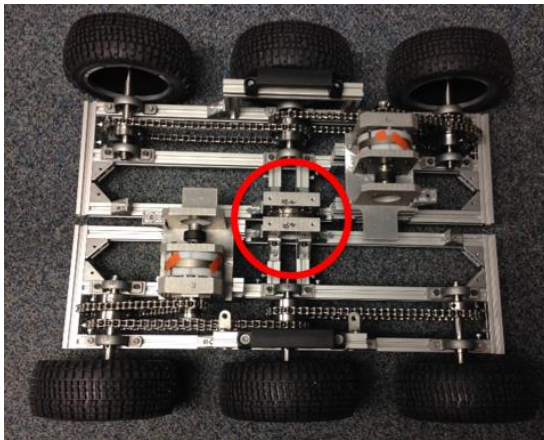
Figure 7.4 Pan-cake suspension system

Because this SUGV was designed to turn through skid steering, different speed commands are sent to the two motors to generate yaw motions.
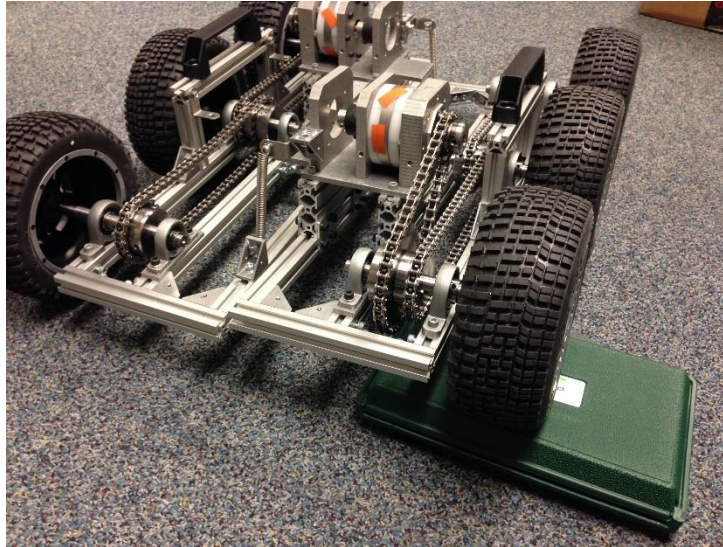
Figure 7.5 The SUGV drives over an obstacle

7.1.2 Electrical system

The structure of the electrical system is shown in Figure 7.6. The parts in the square labeled as SUGV are the elements installed on the test robot. The power needed by the test robot is provided by an on-board battery pack, which consists of two ZIPPY 5000 mAh batteries (one is shown in Figure 7.7). A single battery consists of 6 cells and weighs at 772 grams. The maximum discharge rate is 25 c. The power bus of the test robot is highlighted by the orange dashed window in Figure 7.6. It is protected by a 20A fuse. It also has a switch and an emergency stop on the power bus. The on-board computer serves as a central control unit and data transfer station. It communicates with two MAXON DES 70/10 amplifiers via USB to RS232 adapters. The control program is installed in the on-board computer, which is accessed remotely by another computer in the local network.
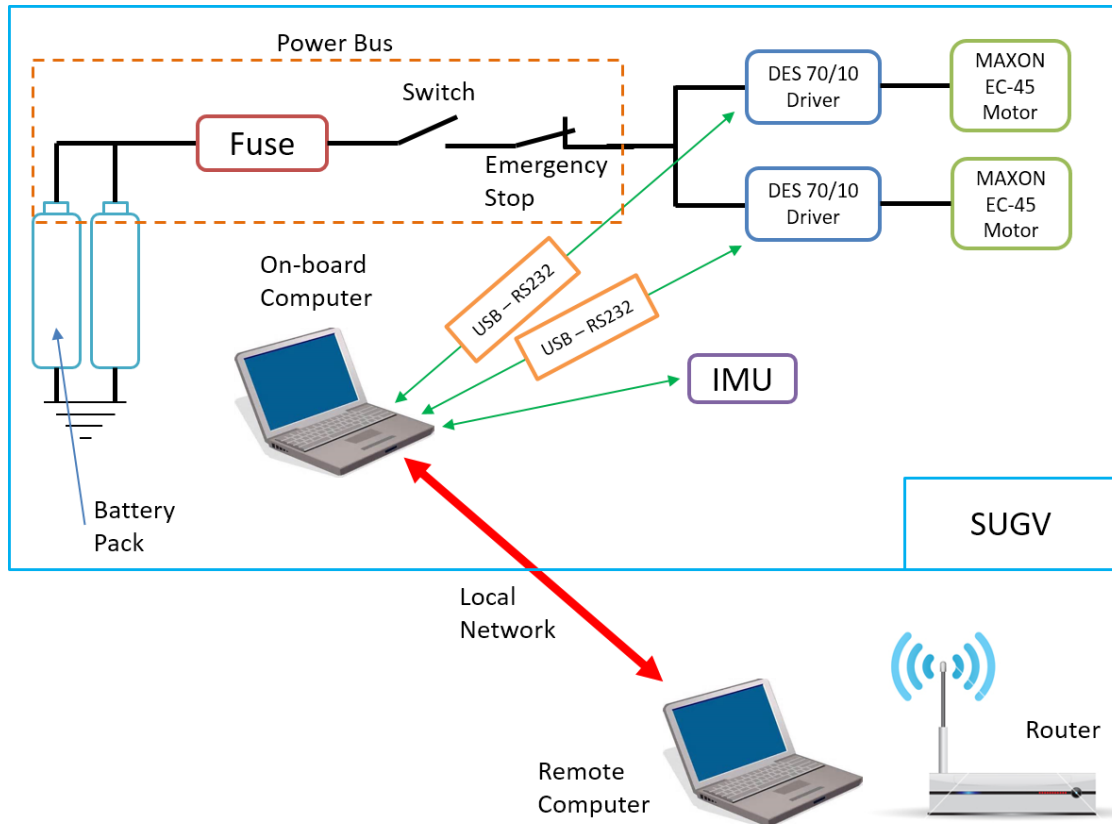
Figure 7.6 The electrical system of the test robot

Figure 7.7 ZIPPY 5000 high discharge Li-Polymer battery

The MAXON DES 70/10 (Digital EC Servo Amplifier) is an efficient digital servo amplifier with sinusoidal current commutation for the control of the EC (Electronic Commutation) motors, shown in Figure 7.8. The maximum output is rated at 70 volts and 10 amps (700 watts). This amplifier is 4-Q ready, which means that it can absorb power from the motor when the vehicle is performing regenerative braking. The detailed specifications of this driver are listed in Appendix A.

Figure 7.8 The DES 70/10 driver

The MAXON EC-45 motor, shown in Figure 7.9, is a brushless DC motor. It is electronically commutated, which provides long life and reliability. It has a 4-pole neodymium magnet providing high torque without a gearhead. The motor has a square cross section of 45mm sides, a length of 155 mm, and a weight of 1,130 g. The continuous output power is 300 watts, and the maximum speed is 10,000 RPM. The detailed specifications of this motor are listed in Appendix B. The motor is equipped with an encoder with the resolution of 2048 pulse per revolution.

Figure 7.9 The MAXON EC-45 motor

7.1.3 Software

The software in the on-board computer consists of 4 parts: communication setup, case setting, test data display, and data saving. The software layout is shown in Figure 7.10. The communication setup part specifies the COM setup and Baud rate setting between the USB ports on the on-board computer and the serial ports on the drivers. When the connections are successfully established, the software will show "Ready" in green. Otherwise it will show "Not Ready" in red. The case setting part has two subcategories: Case Mode and Free Mode. In the case mode, forward velocity and yaw rate are the inputs,

and the test robot will perform these commands. In the free mode, the inputs are the Up, Right, Left, and Down keystrokes on the keyboard as direction commands for the test robot, and the test robot will behave as a remote controlled vehicle. The test data display part displays the two motors' speeds and currents. After each test, "Save data and close" button saves the test data in a csv file and close the program.
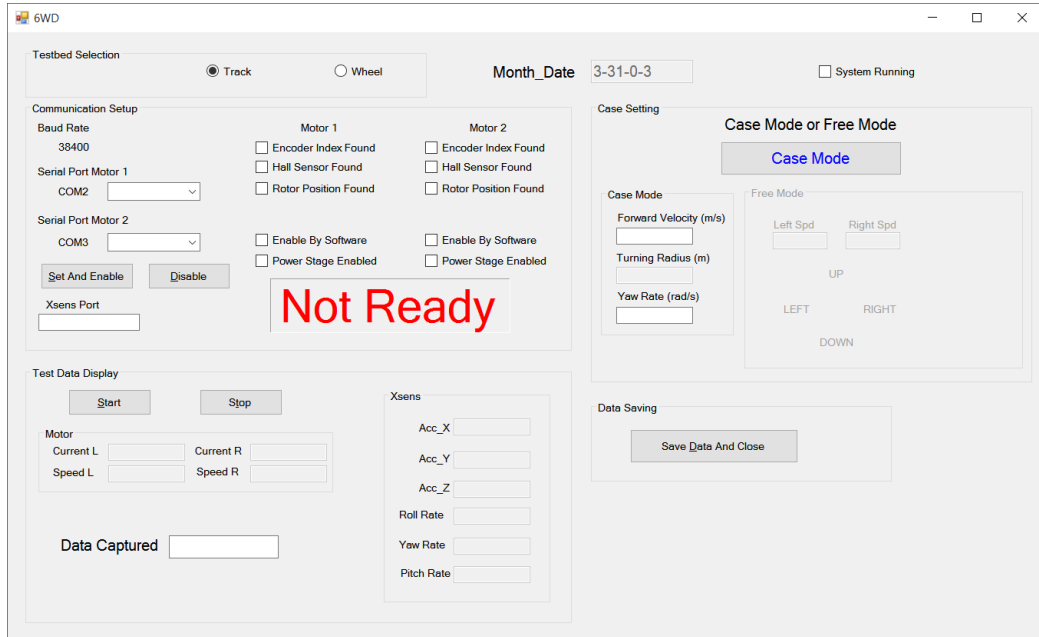
Figure 7.10 The 6-Wheel-Drive test robot control software

7.2 Internal resistance of the powertrain and its power consumption

This section discussed a series of experiments that were conducted to measure the internal resistance and the power consumption of each component in the powertrain as a reference to validate the FESS model.

7.2.1 The motor

The first set of experiments measured the internal resistance and power consumption of the 2 MAXON EC-45 motors. These two motors were removed from the test robot. Different speed commands were sent to the controller and the motors spun without load. Currents and rotational speeds were measured. The internal resistance (in the unit of Newton) due to friction and damping of the mechanical part was calculated. This relationship can be expressed by the following equation

96

$$K_t i = b\omega + c \tag{7.1}$$

where K_t is the motor constant (in the unit of Nm/Amp), i is the current, b is the viscous damping constant, ω is the rotational speed, and c is the coulomb friction constant. The power consumption of the motor without load is expressed in Eq. (7.2).

$$P = b\omega^2 + c\omega \tag{7.2}$$

Once motor currents and rotational speeds were measured, constants b and c were curve fitted. The experiment results are shown in Figure 7.12 and Figure 7.13. Constants b and c are listed in Table 7.1.

7.2.2 The transmission

Internal resistance in the transmission comes from the viscous damping and the coulomb friction in both gear-train and roller-chain. To measure these coefficients, two sets of experiments were conducted. The first set of the experiments measured the internal resistance and the power consumption of the gear-train. The motors were assembled on the chassis together with the gear-train while the roller chain and the wheels or the tracks were removed. The second set of experiments measured the internal resistance and the power consumption of the roller-chain. The motors were assembled on the chassis together with the gear-train and the roller-chain while the wheels or the tracks were removed. The equations are governed by Eq. (7.3).

$$T = K_t i - b\omega - c = b_g\omega + c_g$$
$$P = K_t i\omega - b\omega^2 - c\omega = b_g\omega^2 + c_g\omega$$
$$T = K_t i - b\omega - c - b_g\omega - c_g = b_r\omega + c_r \tag{7.3}$$
$$P = K_t i\omega - b\omega^2 - c\omega - b_g\omega^2 - c_g\omega = b_r\omega^2 + c_r\omega$$

T is the internal resistance, P is the power consumption, i is the motor current, ω is the motor rotational speed, b_g and c_g, are the viscous damping constant and coulomb friction constant of the gear-train respectively, and b_r and c_r are the viscous friction constant and coulomb friction constant of the roller-chain respectively. Once motor currents and rotational speeds were measured, constants b_g, c_g, b_r, and c_r were curve fitted. The experiment results are shown in Figure 7.12 and Figure 7.13. Constants b_g, c_g, b_r, and c_r are listed in Table 7.1.

7.2.3 The running gear

The internal resistance of the running gear is dependent on the terrain-gear (track or wheel) and its design. For the track configuration, the internal resistance is caused by the viscous damping and the coulomb friction of sprockets rolling on the track, mechanical losses caused by the flexing of the rubber belt tracks, and other factors. It is very hard, if not impossible, to accurately model the internal resistance of track systems. However, it can also be approximated by the viscous damping constant (b_t) and coulomb friction constant (c_t), as is expressed by Eq. (7.4), where T is the internal resistance, P is the power consumption, and ω is the rotational speed of the sprockets.

$$T = K_t i - b\omega - c - b_g\omega - c_g - b_r\omega - c_r = b_{track}\omega + c_{track}$$

$$P = K_t i\omega - b\omega^2 - c\omega - b_g\omega^2 - c_g\omega - b_r\omega^2 - c_r\omega = b_t\omega^2 + c_t\omega$$

(7.4)

In this dissertation, it is assumed for the wheel configuration that the wheel is much harder than the terrain, and thus that deformation happens primarily on the soil. As a result, the energy is dissipated primarily on the deformation of the soil, as modeled in Chapter 2. Thus in this dissertation, it is assumed that there is no energy loss due to wheel deformation.

For both configurations in this test robot, the connection between the running gear (sprockets and wheels) and the axle are pins, hex hubs and hex nuts, as shown in Figure 7.11. It is assumed that there is no mechanical loss between the running gear and axle.
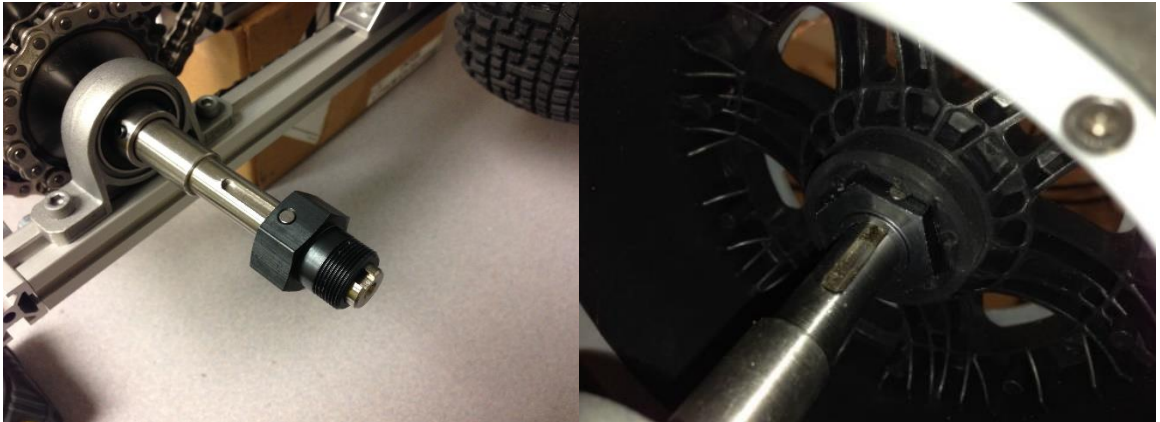
Figure 7.11 Pin, Hex hub and hex nut for the connection between the running gear and the axle

To measure the internal resistance and power consumption of the track system, sprockets and tracks were assembled on the vehicle. The experiments were conducted with the test robot on a jack stand; consequently, there is no load from vehicle-terrain interaction.

Various speed commands were sent to the test robot. Speeds and currents were measured. Constants b_t and c_t were curve fitted.

Experiment results are shown in Figure 7.12 and Figure 7.13. Solid circles are the experiment data, while solid lines are the curve fitted results. It should be stated here that the torque and power consumption were measured from the motor current and rotational speed. Thus the difference between these sets of experiment data is the corresponding part's internal resistance and power consumption. For example, the differences between the red circles and the blue circles are the internal resistance and the power consumption of the gearbox with respect to different motor rotational speeds. It can be seen that the track configuration has a much larger internal resistance and power consumption than the wheel configuration. Moreover, there is slight difference between Motor 1 (left drivetrain) and Motor 2 (right drivetrain). The differences were considered in the field experiments, discussed in Section 7.3, to validate the FESS model. The corresponding fitted coefficients of Motor 1 (left drivetrain) and Motor 2 (right drivetrain) are shown in Table 7.1.
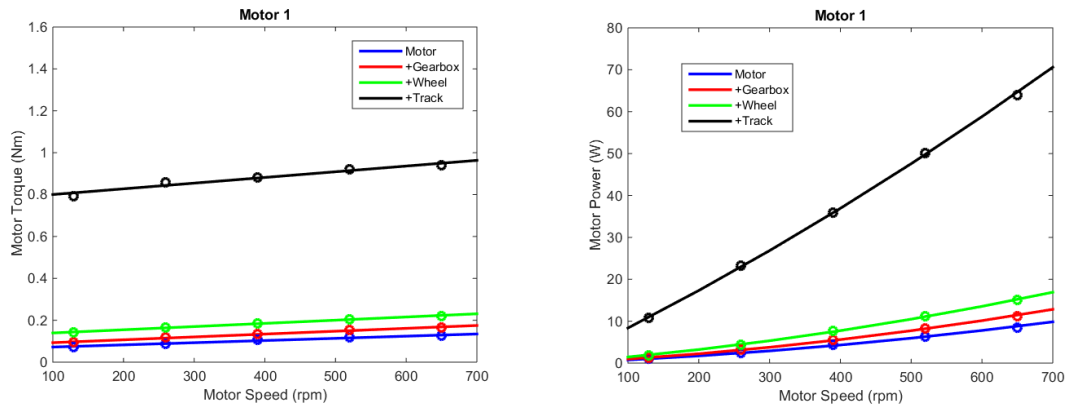
Figure 7.12 Internal resistance and power consumption of Motor 1
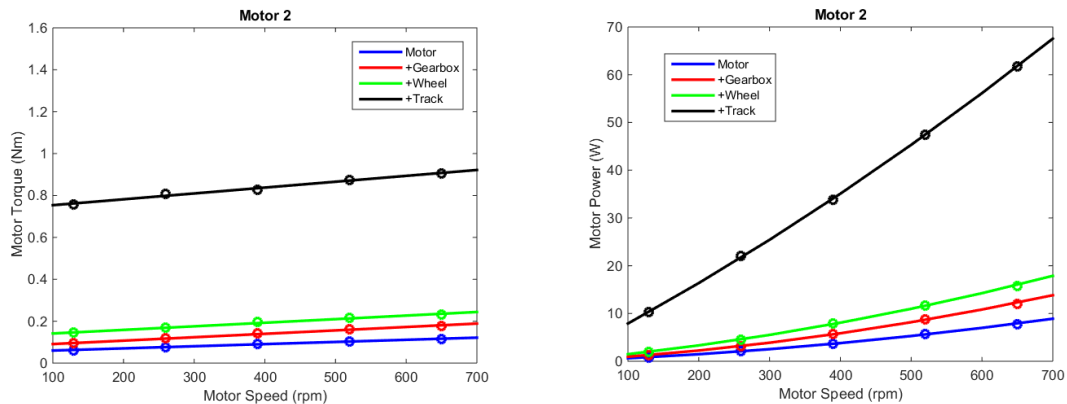
Figure 7.13 Internal resistance and power consumption of Motor 2

Table 7.1 Coefficients of the internal resistance of each part in the powertrain

Left Drivetrain	a, a_g, a_c, a_t	b, b_g, b_c, b_t	Right Drivetrain	a, a_g, a_c, a_t	b, b_g, b_c, b_t
Motor	0.0001	0.0617	Motor	0.0001	0.0499
Gear-train	0.00008	0.0177	Gear-train	0.00009	0.0248
Roller-chain	0.0001	0.0448	Roller-chain	0.0001	0.0497
Track	0.00012	0.6489	Track	0.00013	0.6314

Take 500 rpm running speed of the motor as an example. Figure 7.14 illustrates the relationship among each powertrain part's average power consumption for the track configuration. It can be seen that resistance and its corresponding power consumption between the track and sprocket dominates the internal power loss for this test robot.
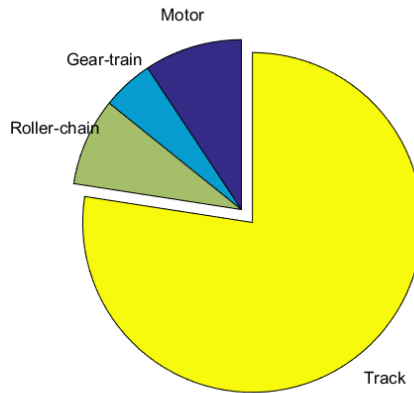
Figure 7.14 An example of the relationship between each powertrain part's average power consumption of the track configuration

7.3 Experiments to validate the FESS model

In Chapter 6, the FESS model was developed for both tracked and wheeled SUGVs running on deformable terrains. In the previous section, internal power consumption of the test robot was measured. In this section, skid steering experiments of the test robot running on dry sand were conducted to validate the FESS model. Motor speeds, motor currents, and vehicle states were measured.

7.3.1 The experiment site

The experiments were conducted in a sand bin in an indoor environment. The sand bin is a part of the Geotechnical Laboratory Facilities in the Civil and Environmental Engineering Department at the University of Michigan. The sand bin, shown in Figure 7.15, is a circular area with a diameter of around 5 meters. The main reason for choosing this indoor sand bin instead of an outdoor sandy area (e.g. sand volleyball beach) is that the sand conditions of this indoor sand bin could be maintained and controlled throughout the experiments. For an outdoor sandy area, the moisture, compactness of the sand, and level of the surface are vulnerable to environmental conditions, such as weather, precipitation, temperature, and wind.

Figure 7.15 The sand bin

The experimental setup is illustrated in Figure 7.16. The sand was smoothed and flattened before each experiment. We used a camera to capture the vehicle states, which will be explained in details in the next section.
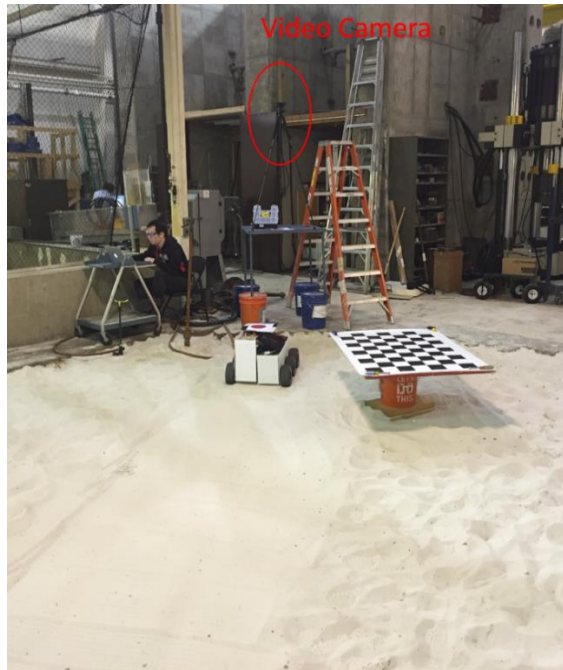
Figure 7.16 The experimental setup

7.3.2 The sand properties

Athena Grizi prepared the specimen and conducted the measurements of the sand properties with a standard ShearTrac II system from the Geocomp Co. The device was also a part of the Geotechnical Laboratory Facilities in the Civil and Environmental Engineering Department at the University of Michigan and the experimental setup are shown in Figure 7.17 and Figure 7.18 respectively. The sand is maintained dry throughout the experiments. The sand properties are shown in Table 7.2.
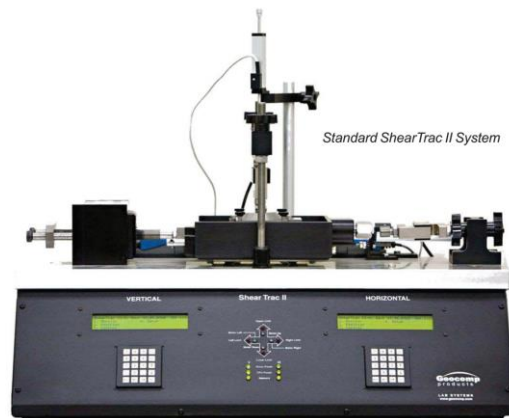
Figure 7.17 The standard ShearTrac II system
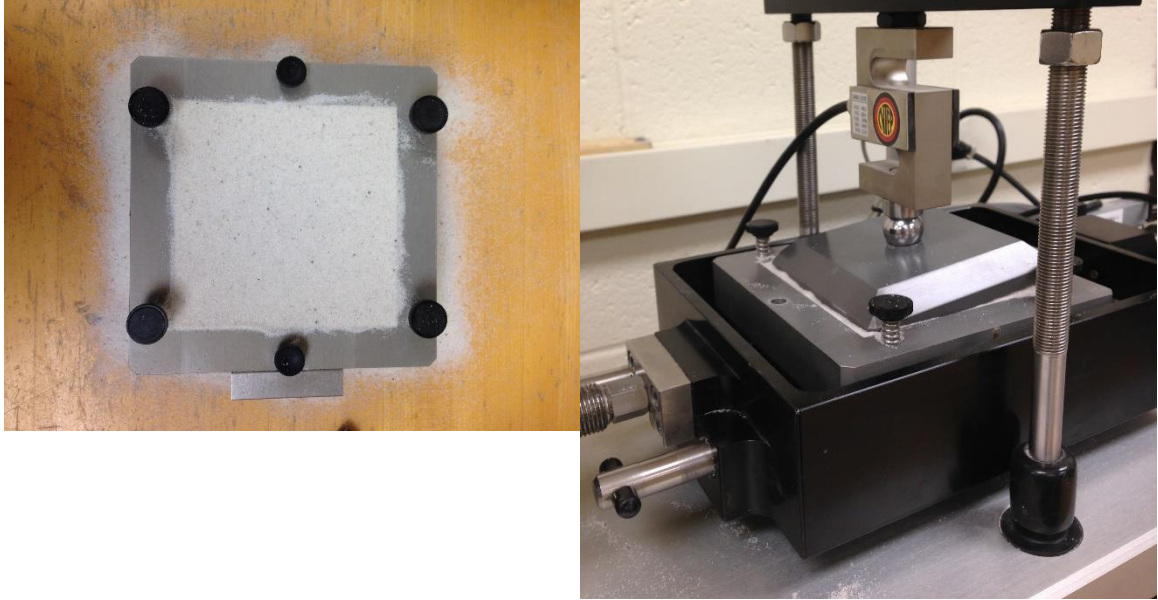
Figure 7.18 The experimental setup

Table 7.2 The sand properties

	Dry Sand in the Sand Bin
n	1.08
c (Pa)	200
ϕ (°)	27
k_c (N/m^{n+1})	1000
k_ϕ (N/m^{n+2})	1528600
K (m)	0.024

7.3.3 The motion capture method

Since our experiments were conducted in an indoor environment, GPS systems, although widely used for on-road vehicles, are not appropriate to accurately measure the vehicle speed and vehicle position to calculate the curvature of the trace. Moreover, low cost GPS systems has unacceptable accuracy for the purpose of our experiments. Instead, we use a camera system to capture the motion of the vehicle. The camera system can achieve accuracy in millimeters. Since the test robot is assumed to do plane motion, only one camera is required. The camera used in our experiments is a webcam from Logitech,

shown in Figure 7.19. This camera's resolution is 1920 x 1080, and is capable of recording videos at 30 frames per second.

Figure 7.19 Logitech C920 webcam

The motion capture method usually involves three processes: camera calibration, motion capture, and image processing.

Section A.   Camera Calibration

Camera calibration is the process of estimating the parameters of the lens and the image sensor of the camera. These camera parameters are used to correct for lens distortion, measure the size of an object in the real world, or determine the location of the camera in the scene. Using the pinhole camera model, the relationship among the 3-D object, the camera, and the 2-D image can be explained in Figure 7.20.
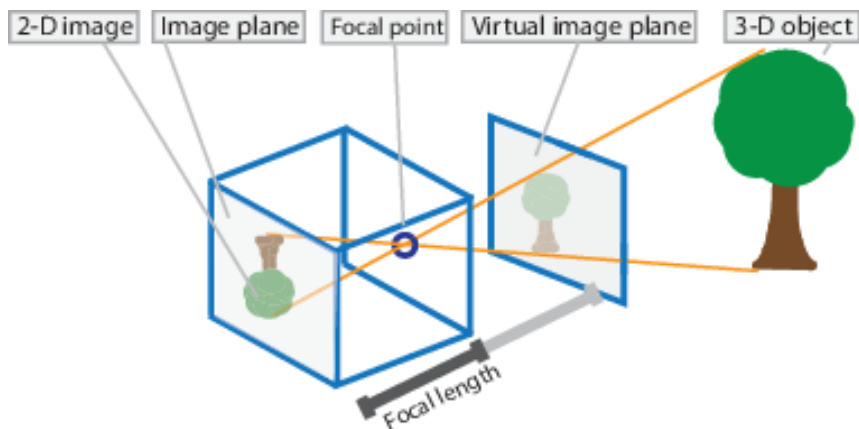
Figure 7.20 Pinhole camera model

The pinhole camera parameters are represented in a 4-by-3 matrix called the camera matrix. This matrix maps the 3-D world scene onto the image plane. The camera matrix is calculated by the calibration algorithm using the extrinsic and intrinsic parameters. The

extrinsic parameters represent the location of the camera in the 3-D scene. The intrinsic parameters represent the optical center and focal length of the camera. The equation to explain this relationship is shown below.

$$w[x \; y \; 1] = [X \; Y \; Z \; 1]P \tag{7.5}$$

In Eq. (7.5), w is the scaling factor of the image, $[x \; y \; 1]$ are the coordinates of an image point, $[X \; Y \; Z \; 1]$ are the coordinates of a corresponding world point, and P is the camera matrix, which is explained in the equation below.

$$P = \begin{bmatrix} R \\ T \end{bmatrix} K \tag{7.6}$$

In Eq. (7.6), $[R \; T]'$ is the extrinsic matrix, R is the rotation matrix, T is the translation matrix, and K is the intrinsic matrix. The world points are transformed to the camera coordinates using the extrinsic matrix. The camera coordinates are mapped into the pixel coordinates using the intrinsic matrix. This relationship is shown in Figure 7.21.
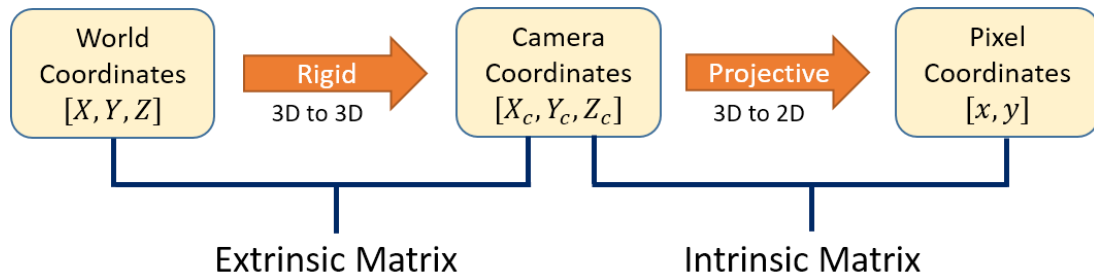
Figure 7.21 World coordinates vs. camera coordinates vs. pixel coordinates

Since an ideal pinhole camera model does not account for lens distortion, the camera matrix must include radial and tangential lens distortion to represent a real camera. Radial distortion occurs when light rays bend more near the edges of a lens than they do at its optical center.
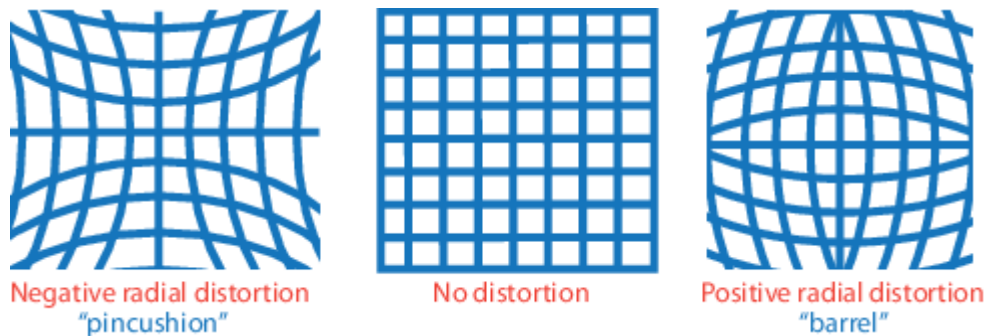
Figure 7.22 Lens distortion [50]

The radial distortion can be modeled as the following equation. The distorted points are denoted as $(x_{distorted}, y_{distorted})$.

$$
\begin{aligned}
x_{distorted} &= x(1 + k_1 r^2 + k_2 r^4 + k_3 r^6) \\
y_{distorted} &= y(1 + k_1 r^2 + k_2 r^4 + k_3 r^6) \\
r^2 &= x^2 + y^2
\end{aligned}
\tag{7.7}
$$

In this equation, x and y are undistorted pixel locations in the normalized pixel coordinates which are calculated from pixel coordinates by translating to the optical center and dividing by the focal length in pixels. x and y are dimensionless. k_1, k_2, and k_3 are radial distortion coefficients of the lens. Typically two coefficients (k_1, k_2) are sufficient for calibration. Only for very wide-angle lenses, 3 coefficients (including k_3) are necessary [50].

Tangential distortion occurs when the lens and the pixel plane are not parallel. This can be illustrated in Figure 7.23. Since the Logitech webcam does not suffer from tangential distortion, it is not explained here.
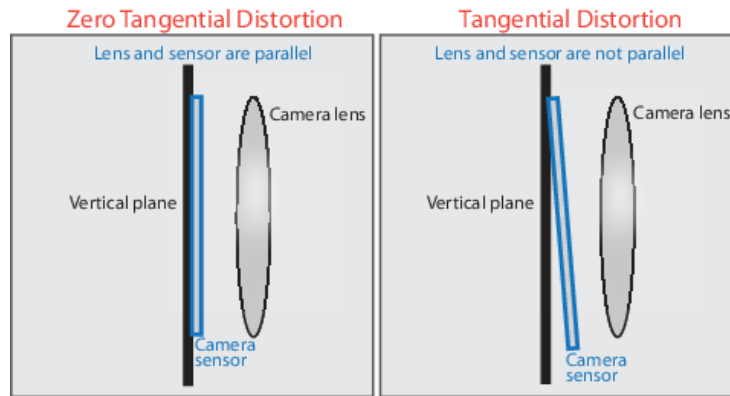
Figure 7.23 Tangential distortion [50]

We used the Matlab Single Camera Calibrator Application to calibrate the Logitech C920 webcam. We used a black checkered board printed on a 3-by-4 foot poster as the reference, shown in Figure 7.24. Each checkerboard square measures 109 millimeters per side. Eight pictures, shown in Figure 7.25 were taken to cover most of the lens and image sensor area.
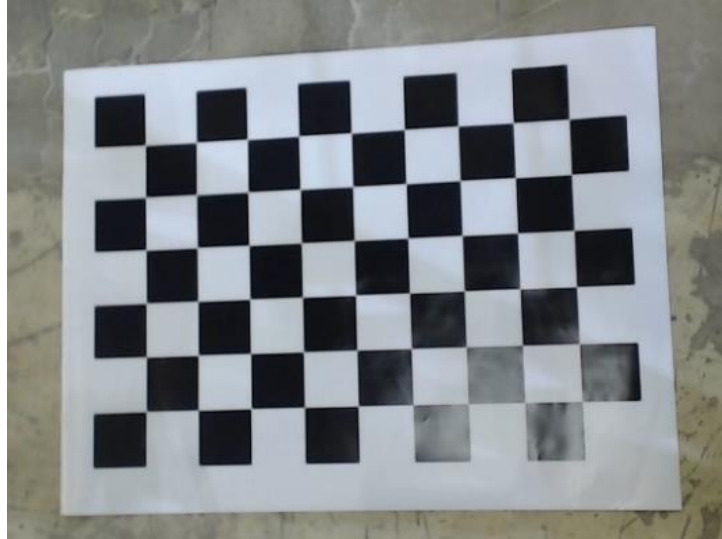
Figure 7.24 The black checkered board

Figure 7.25 The eight pictures

After calibration, the intrinsic matrix, the distortion coefficients, and other camera parameters were stored in the system. Figure 7.26 and Figure 7.27 show the results of the camera calibration.
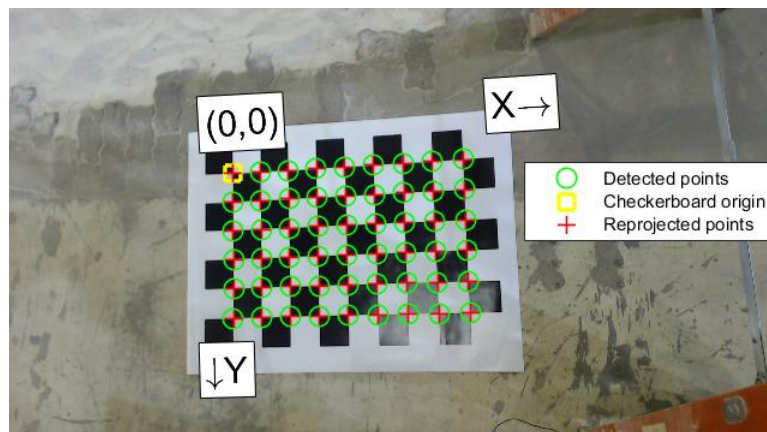
Figure 7.26 An example of detected points vs. re-projected points
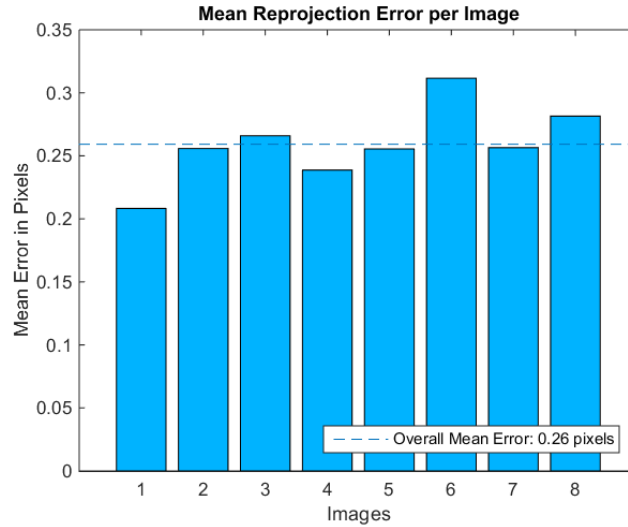
Figure 7.27 Mean re-projection error per image

Section B.   Motion Capture

The second process was shooting the video with the Logitech C920 during the experiments. The video was taken at 30 frames per second and was sampled at 5 Hz to generate a series of images, illustrated in Figure 7.28.

Figure 7.28 Sample the video at 5 Hz

Section C.   Image Processing

The third process was processing the images to extrapolate the position of the vehicle in each image to calculate the turning radius and forward velocity. This task is not trivial. We achieved this task in four steps.

The first step was undistorting the images using the camera parameters, described in Section A. Figure 7.29 shows an example of an original image vs. an undistorted image. It can be seen in the black frame around the undistorted image that the radial distortion has been corrected with the help of the reference (the black checkered board).

Original Image   Undistorted Image

Figure 7.29 Original image vs. undistorted image

The second step was detecting the vehicle. This is achieved by detecting a target on the vehicle. A solid red circle was used as the target. Since there is only one camera, field depth cannot be captured. Thus it is very important to make sure that the reference (the black checkered board) is on the same plane as the target. We used a level meter, shown in Figure 7.30, and a ruler to achieve that.

Figure 7.30 The level meter

In order to detect the solid red circle in each image, we used two color spaces to isolate it from the background. One color space is the RGB color space (where R stands for red, G stands for green, and B stands for blue). The other is the HSV color space (where H stands for hue, S stands for saturation, and V stands for value). These two color spaces are illustrated in Figure 7.31. We displayed the image in both the RGB color space and the HSV color space, shown in Figure 7.32, and we then set thresholds for the RGB channels in the RGB color space and threshold for saturation in the HSV color space to filter out the solid red circle. After this step, the undistorted image becomes a binary image in black and white. The target solid red circle was in white, as shown in Figure 7.33.

109

RGB Color Space   HSV Color Space
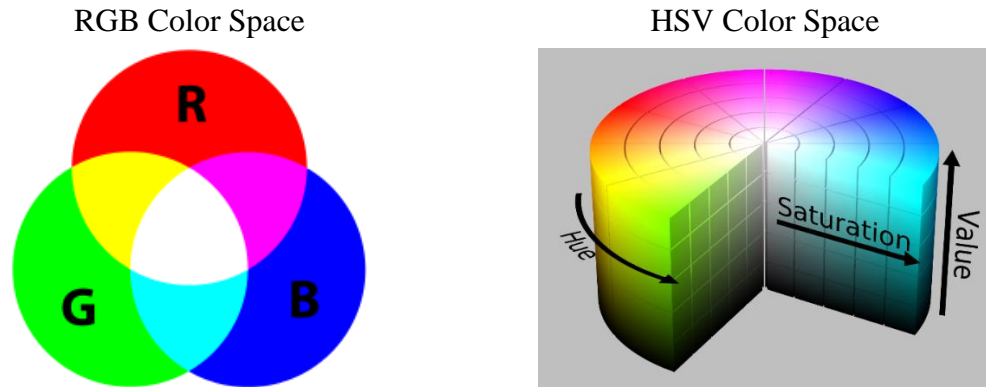
Figure 7.31 RGB color space and HSV color space
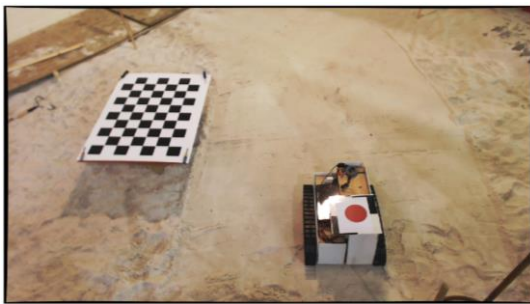
Image in the RGB Color Space   Image in the HSV Color Space
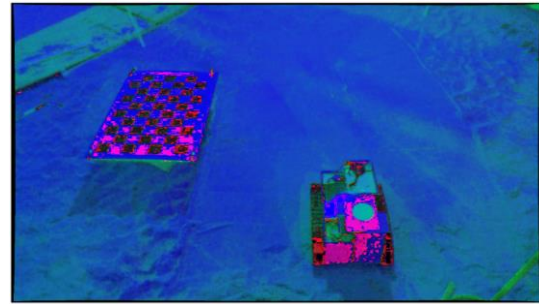
Figure 7.32 Image in the RGB color space and the HSV color space

Figure 7.33 The binary image after filtering

The third step was extrapolating the white target from the binary image. The blobanalysis method was used to achieve that. The blobanalysis method computes the

statistics for connected regions in a binary image. The details of this method can be found in [51].

Once the target was extrapolated from the binary image, the fourth step was calculating the coordinates of the target in the real world with the help of the intrinsic and extrinsic matrices of the camera, obtained in the previous section. The result is shown in Figure 7.34. The diameter of the circle was calculated from the image as 144.30 mm, while the real measurement of the circle was 144.00 mm. The very small discrepancy demonstrates the great accuracy of this method.

These four steps were applied for all the images sampled from the video, and the center of the target in the world coordinates of each image was stored to calculate the turning radius and the forward velocity of the vehicle.
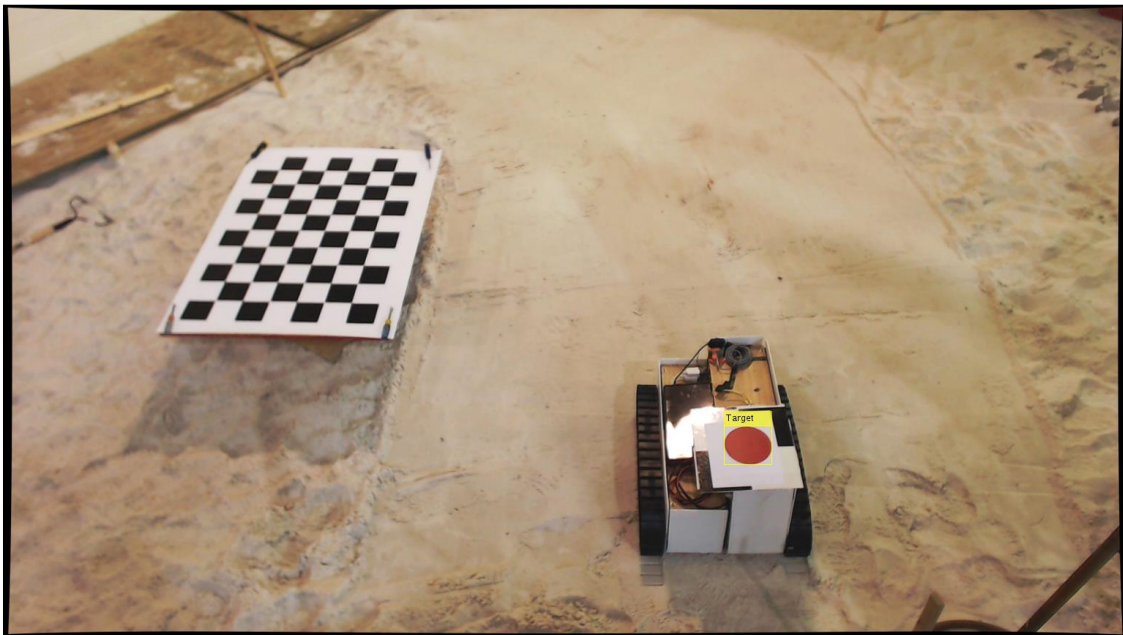
Figure 7.34 The detected target

Once each image of an experiment set was analyzed and the center of the target in the world coordinates was stored, the turning radius and the average forward velocity of the test robot could be calculated by solving a least square problem. Since the test robot was commanded to follow a constant turning radius, the trace of the test robot was assumed to be a circle. Thus, the least square problem of this circle can be written as Eq. (7.8), where x and y are the coordinates of the center of the target in the world coordinates and a, b, c, and d are the coefficients to be determined.

$$a(x^2 + y^2) + bx + cy + d = 0 \qquad (7.8)$$

The Singular Value Decomposition (SVD) method was used to solve this problem. The center of the circle (x_c, y_c) was expressed as Eq. (7.9), and the radius of the circle r was expressed as Eq. (7.10).

$$x_c = -\frac{b}{2a} \quad y_c = -\frac{c}{2a} \qquad (7.9)$$

$$(7.10)$$

$$r = \sqrt{x_c^2 + y_c^2 - \frac{d}{a}}$$

Figure 7.35 shows an example of the trace of the test robot measured by the motion capture system vs. the curve fitted circle. The calculated turning radius is 1.83 meters and the average forward velocity is 0.09 m/s. All the other experimental data and the corresponding curve fitted circles are shown in Appendices D.
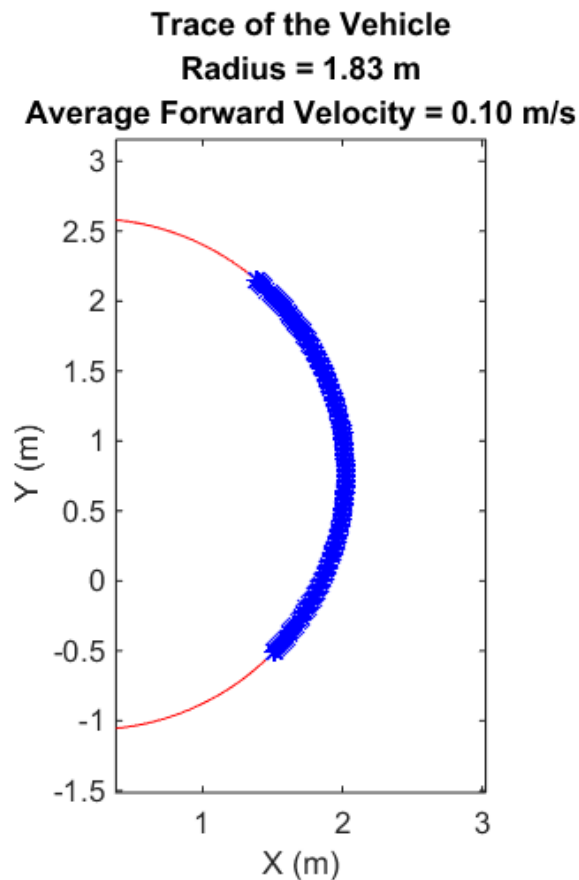
Figure 7.35 An example of the trace of the test robot vs. the curve fitted circle

7.3.4 Power consumption of skid steering on dry sand

Skid steering experiments of the test robot were conducted on dry sand, shown in Figure 7.16. There were three configurations of the test robot: 4-wheel, 6-wheel, and track, illustrated in Figure 7.36. Various forward velocity and yaw rate commands were sent to the test robot. Table 7.3 shows the experimental sets which consist of two groups. The commanded forward velocities are 0.1 m/s and 0.2 m/s. The command yaw rates range from 0 (straight running) to 0.35 rad/s. It should be stated here that skid steering tests failed (cells with no entry in Table 7.3), when the turning radius was small. Because of the large sinkage, the test robot got stuck in the sand, as shown in Figure 7.37. For each combination represented in the table, currents and speeds of the motors were measured, and real forward velocity and turning radius of the vehicle were calculated from the motion capture system.

Table 7.3 Experimental sets

		Yaw Rate (rad/s)										
		0	0.01	0.02	0.04	0.08	0.1	0.15	0.2	0.25	0.3	0.35
Forward Velocity (m/s)	0.1	✓	✓	✓	✓	✓	✓	✓	✓			
	0.2	✓	✓	✓	✓	✓	✓	✓	✓	✓	✓	✓

Figure 7.36 The three configurations of the test robot
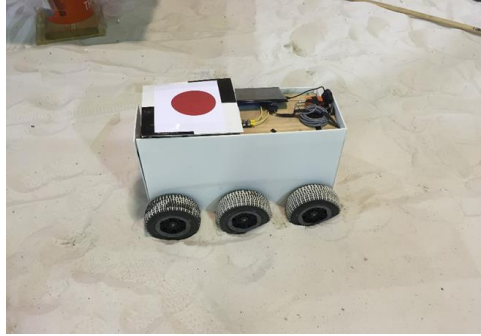
Figure 7.37 The test robot got stuck in the sand when the turning radius is small

Once each image from the experiments was analyzed and the corresponding vehicle states (turning radius and average forward velocity) were calculated, Figure 7.38 shows the comparison between experimental results and commands for the turning radius. The title of each figure shows the configuration of the test robot (4-Wheel, 6-Wheel, or Track) and the average forward velocity from the experiments. The figures in the left column represent those experiments with commanded forward velocity at 0.1 m/s, while the right column of the figures represent those experiments with commanded forward velocity at 0.2 m/s. In these figures, the first experiment set is going straight. Thus the commanded turning radius is infinity and is not plotted on the graph. It can be seen that there can be large discrepancies between the commanded turning radius and the real turning radius, especially when the turning radius is large. The actual turning radius and the forward velocity calculated from the experiments were used to validate the FESS model.

The experiment results for torque and power consumption on the left and right axles vs. those of the simulation results from the FESS model are shown in Figure 7.39, Figure 7.40, and Figure 7.41, representing 4-wheel, 6-wheel, and track configuration respectively. For each figure, there are four plots. The plots in the left column are for torque comparison, while the plots in the right column are for power consumption comparison. The plots in the upper row are at forward velocity = 0.1 m/s, while the plots in the lower row are at forward velocity = 0.2 m/s. The circles with error bars are the experimental data, while the solid and the dashed lines are simulation results. Since the real forward velocities calculated from the experiments are not constants, the simulation results are in a range. The dashed lines are the simulation results for the lower bound of the forward velocity, while the solid lines are those for the upper bound of the forward velocity. It can be seen from the three figures that torques on the axles are not sensitive to the forward velocity.

114
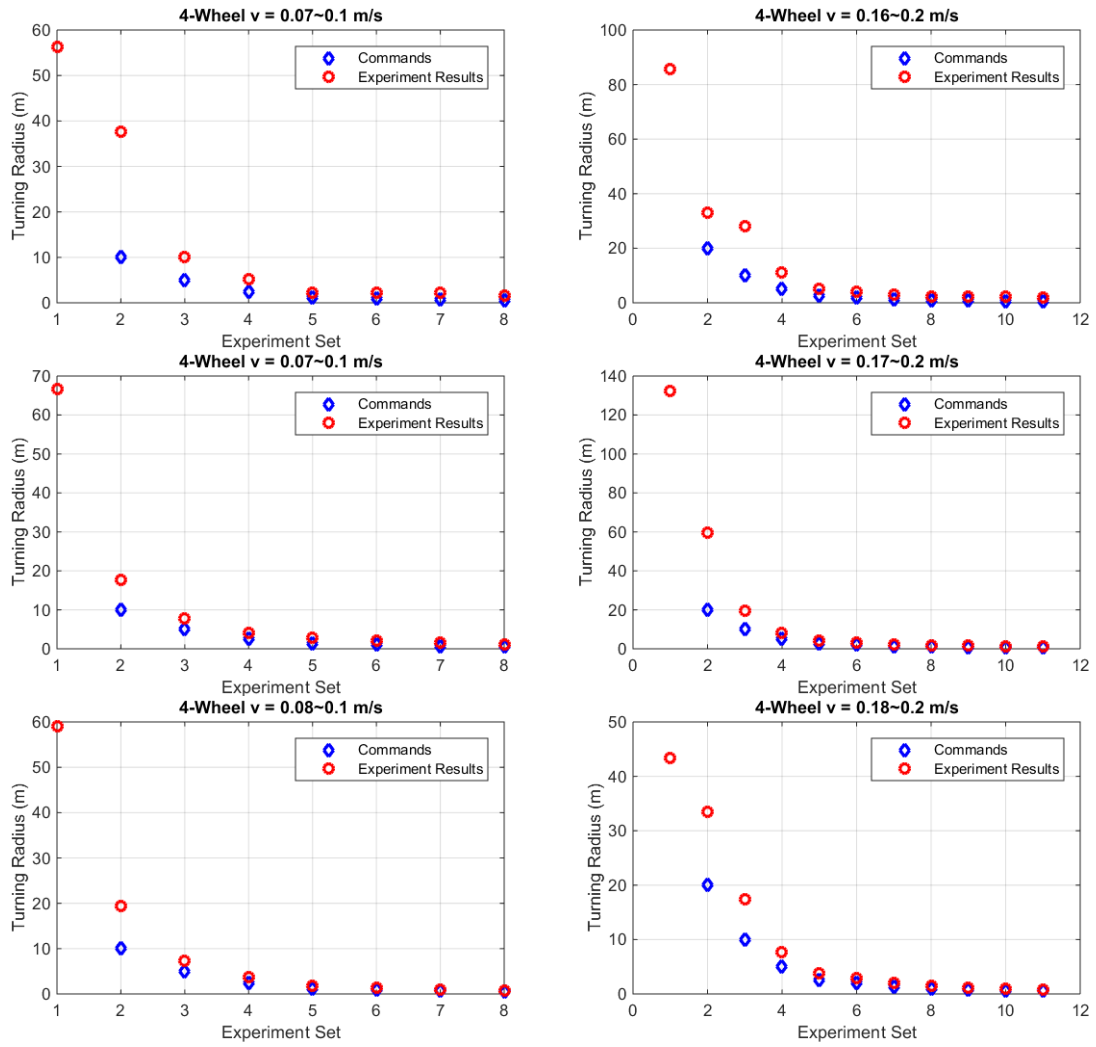
Figure 7.38 Experiment turning radius vs. commanded turning radius
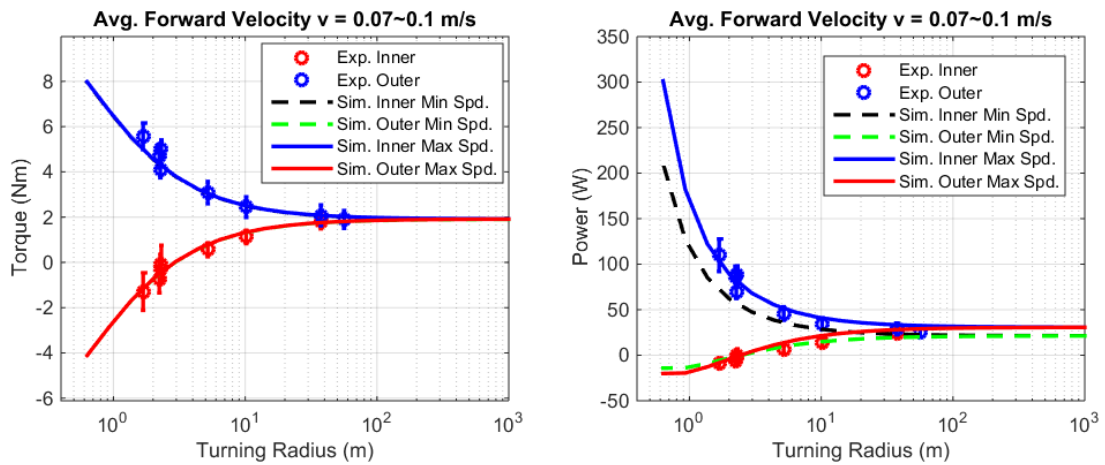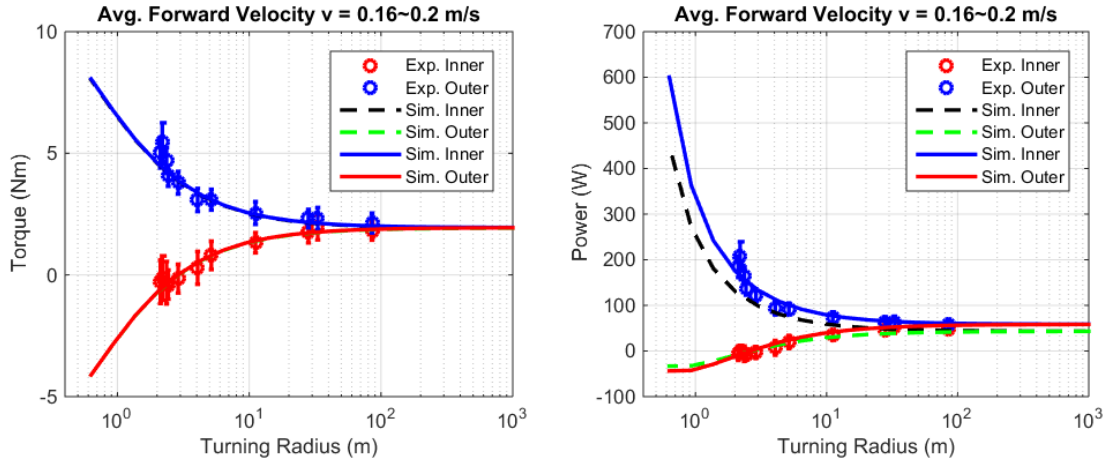
Figure 7.39 Experiment results (4-wheel configuration) vs. simulation results of the FESS model
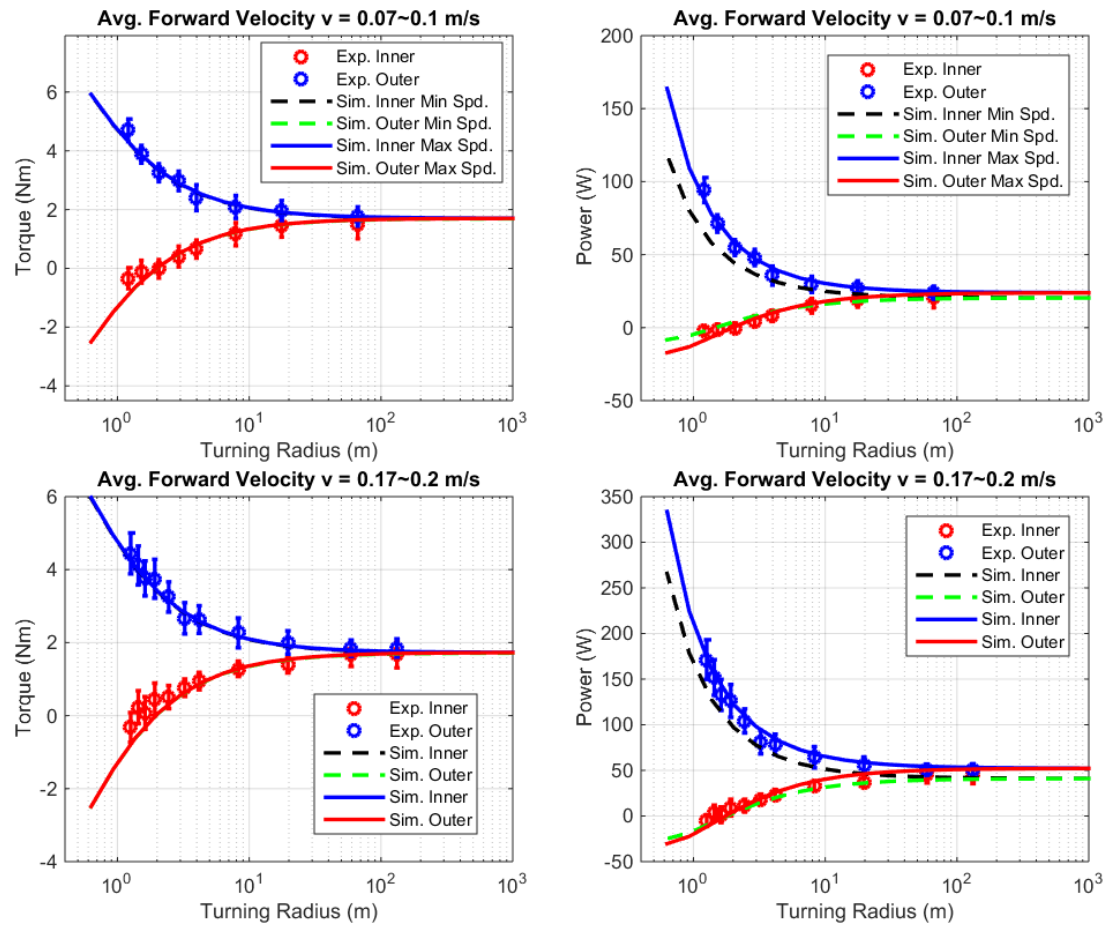
Figure 7.40 Experiment results (6-wheel configuration) vs. simulation results of the FESS model
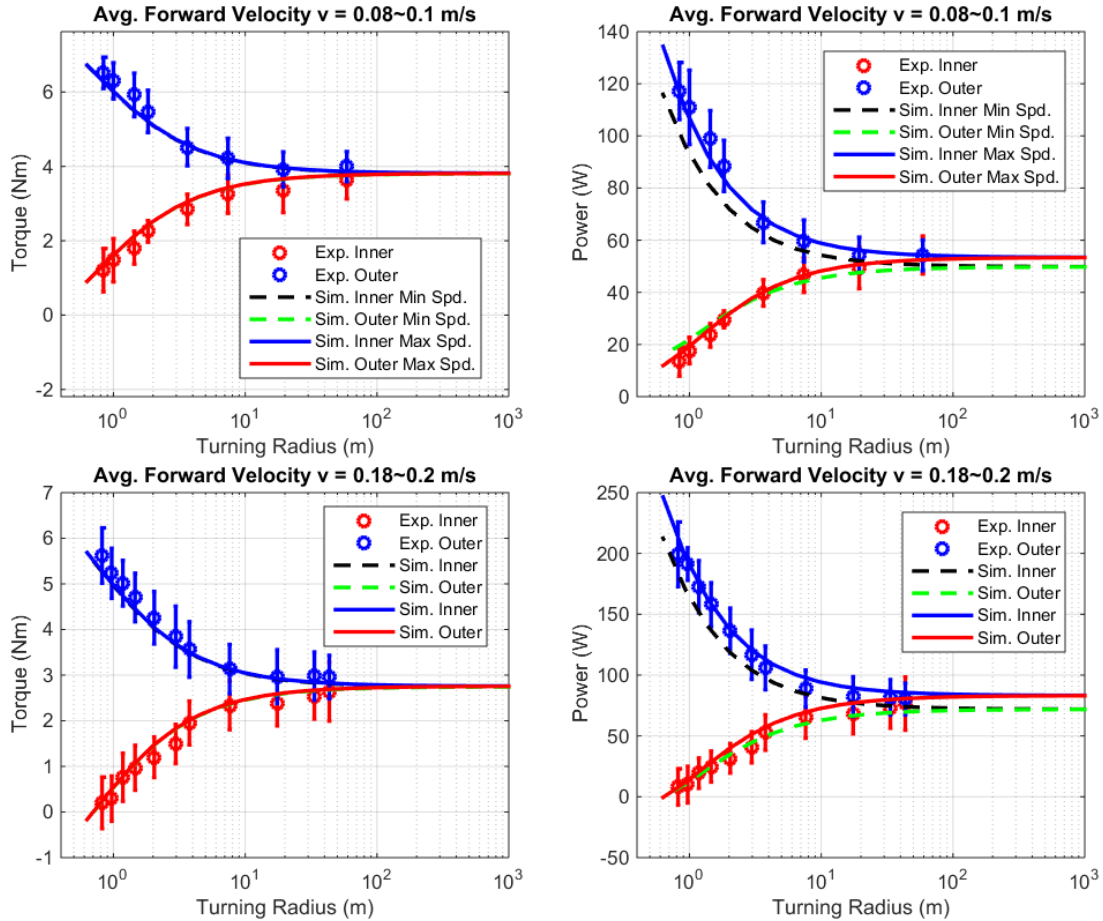
Figure 7.41 Experiment results (track configuration) vs. simulation results of the FESS model

Overall, it can be seen from the figures that the simulated torque and power consumption of the FESS model are validated by the experiments. For the track configuration, the error bars of the experiment data for both torque and power consumption are larger than those for the wheel configurations. This is because of the repeated bending of the tracks during the experiments and the resulted oscillation of the track tension. Moreover, we observed during the experiments that sand got into the gaps between the tracks and the sprockets, which further increased the oscillation of the track tension, resulting in larger fluctuation of the motor torque and motor power consumption.

7.4 Summary

In this chapter, the design and building of the 6-wheel-drive track-wheel interchangeable test robot was described. Key vehicle states (average forward velocity and

turning radius) were calculated by using a motion capture system. Skid steering experiments of the test robot with three configurations (4-wheel, 6-wheel, and track) on dry sand were conducted to validate the FESS model. The FESS model results are found to be largely within the uncertainties of the experimental data.

CHAPTER 8
Track vs. Wheel

The compare-and-contrast of tracked SUGVs versus wheeled SUGVs for off-road operations is a subject of continuous study. Although a number of experimental studies in evaluating the performance of specific tracked vehicles have been performed, relatively few simulation studies on this subject have been reported in the open literature. A comprehensive comparison including propulsion performance, handling, reliability, maintainability, etc. is beyond the scope of this study. We focused on only two aspects: power consumption and mobility. In this chapter, two case studies were conducted based on an SUGV that has a similar size to the Packbot.

8.1 A case study of an SUGV patrolling an area

Patrolling an area is a common task for an SUGV; possible missions include monitoring a boarder, searching for explosives or chemicals, or even performing surveillance of a battle front. In this section, a Packbot-sized SUGV is assumed to be on a mine detection mission. Power consumption and mobility of this SUGV, using three designs: tracked, 4-wheel, and 6-wheel configurations, are compared. Figure 8.1 shows the area to be covered and the blue line is the pre-generated path. The area to be covered measures 15 by 22 meters and is covered with dry sand. The path is composed of two parts: driving straight and turning. The turning radius is 1 meter. A typical Packbot from the iRobot Co. is shown in Figure 8.2. The Packbot only has the track configuration. However, in this case study, two imaginary Packbots with 4-wheel and 6-wheel configurations respectively are studied. The imaginary wheeled Packbots are shown in Figure 8.3. Because the original Packbot is a military vehicle, information about its powertrain design and specifications are not open to the public. Thus the powertrain design and specifications from the test robot, described in Chapter 7, is used in the simulations. And the internal

119

resistance coefficients obtained from the experiments are used. This assumption is reasonable, because the dimensions and weight of the original Packbot are similar to those of the test robot. Moreover, to enable a fair comparison among these three configurations, all of these simulated SUGVs share the same weight, CG height, tread of the vehicle. These SUGVs' simulation parameters are listed in Table 8.1. Parameters of the terrain (sandy soil) are listed in Table 8.2.
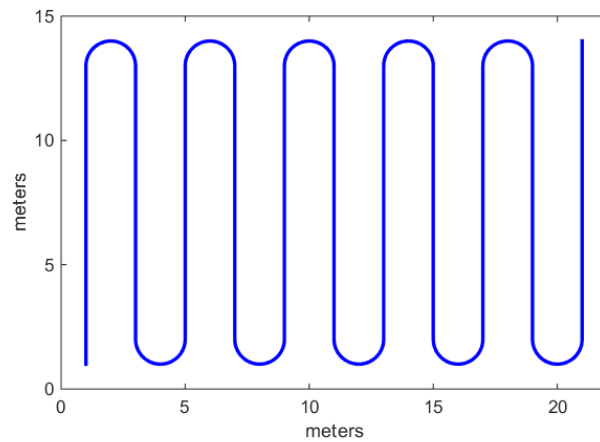
Figure 8.1 The area to be covered and the corresponding mission path

Figure 8.2 The Packbot from the iRobot Co.

4-Wheel Packbot   6-Wheel Packbot
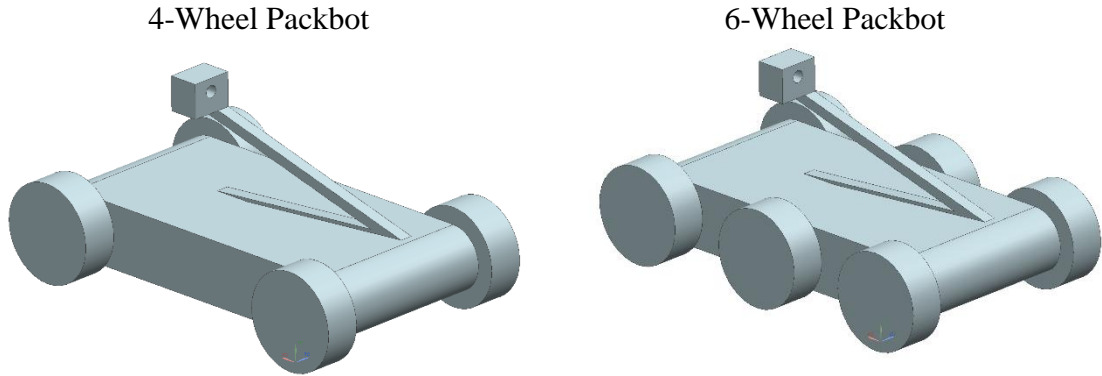
Figure 8.3 The imaginary Packbots with 4-Wheel and 6-Wheel configurations

Table 8.1 Packbots' simulation parameters

Chassis Parameters	
Mass (kg)	15.8
CG Height (m)	0.08
Tread of the Vehicle (m)	0.4
Track Parameters	
Track Length (m)	0.7
Track Width (m)	0.074
Sprocket Radius (m)	0.1
Axle Base (m)	0.35
Wheel parameters	
Wheel Width (m)	0.074
Wheel Radius (m)	0.1
Wheel Base (4-Wheel) (m)	0.7
Wheel Base (6-Wheel) (m)	0.35

Table 8.2 Parameters for the simulation terrain

	Sandy Soil
n	1.1
c (Pa)	1000
ϕ (°)	30
k_c (N/m^{n+1})	900
k_ϕ (N/m^{n+2})	1523400
K (m)	0.025

Source: [45]

The forward velocity of the SUGVs in this mission is set as a constant value of 0.2 m/s. The total mission distance is 154.4 meters, 20% (31.4 meters) is turning, while 80% (123.0 meters) is driving straight.
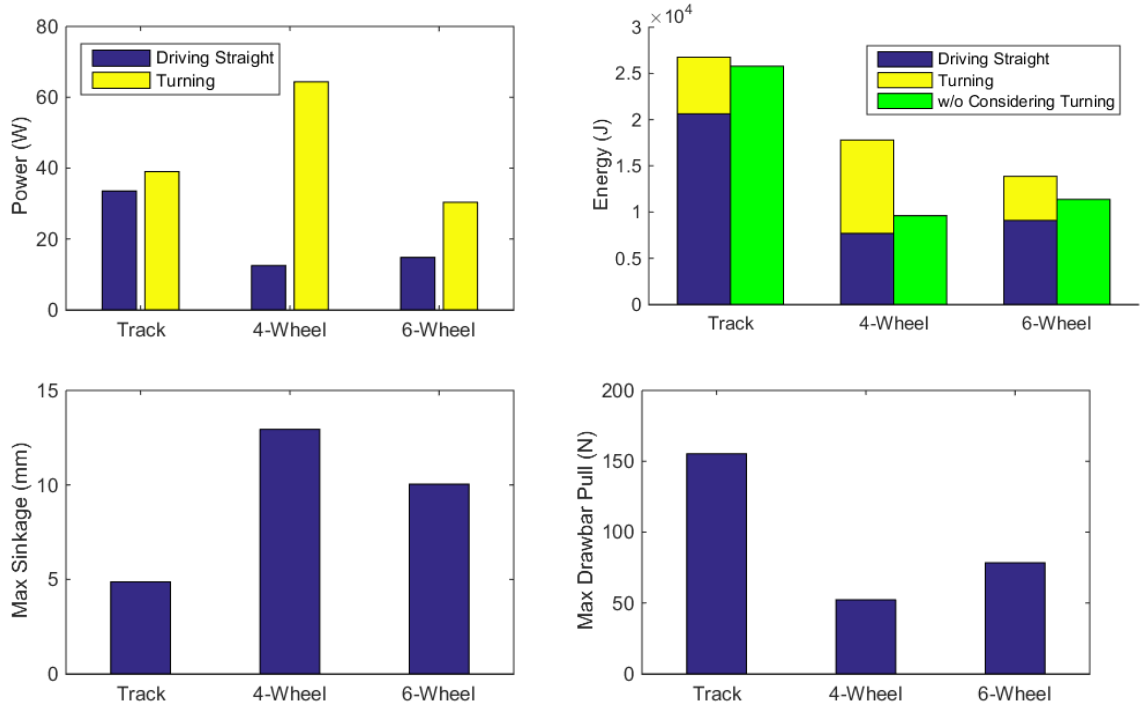
Figure 8.4 The power consumption, energy consumption, maximum sinkage, and maximum drawbar pull of the three configurations

Figure 8.4 shows the simulation results of the SUGVs in three configurations in this mission. It can be seen that while driving straight, the tracked design uses more power (34 W) than wheeled designs, while during turning, the 4-wheeled design needs more power (62 W) than the tracked design. For the tracked design, power consumption increases less than 20% (from 34 W to 40 W). For the 4-wheeled design, power consumption increases more than 400% (from 12 W to 62 W). Over the whole mission, the tracked design requires the largest total energy consumption (2.7×10^4 J), while the 6-wheeled design is most efficient (1.4×10^4 J). For the tracked Packbot, energy consumption during turning is just a little more than only 0.6×10^4 J. For the 4-wheeled design, however, more than half of the energy is consumed during turning. If someone estimates the energy consumption without considering skid steering but treating turning as straight driving, there are underestimates, especially large for the wheeled SUGVs. In terms of mobility, the tracked design has the lowest sinkage (5 mm) and largest drawbar pull (151 N). The 4-wheeled design has the worst mobility, with highest sinkage (13 mm) and lowest drawbar pull (51 N).

Figure 8.5 shows the ratio of the energy consumption between internal energy consumption and energy consumption due to the vehicle-terrain interaction in the three configurations. It can be seen that for the tracked design, 85% of the total energy is consumed internally, while for the 4-wheeled design, 66% of the total energy is consumed due to the vehicle-terrain interaction. The 6-wheeled design falls in between: 52% of the total energy is consumed internally, while 48% of the total energy is consumed due to vehicle-terrain interaction. These ratios, together with the fact that internal power consumption does not differ much between driving straight and turning, explain the small difference of the power consumption between driving straight and turning for the tracked design and the large difference of the power consumption between driving straight and turning for the 4-wheeled design.
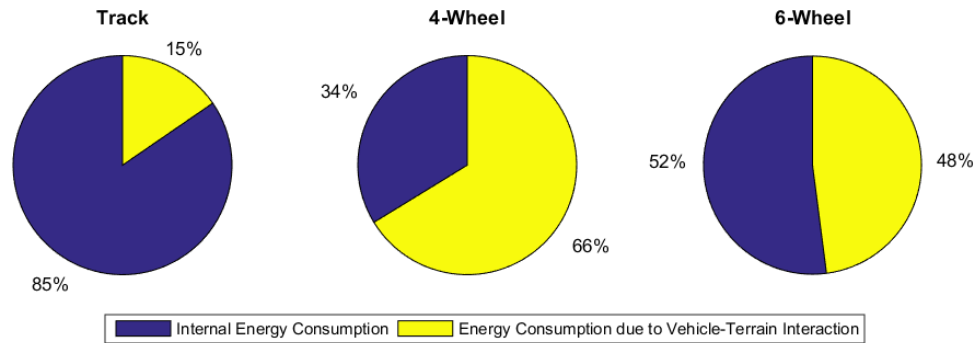
Figure 8.5 The ratio of the energy consumption between internal energy consumption and energy consumption due to the vehicle-terrain interaction

Based on this case study, skid steering must be considered in the power consumption calculation for SUGVs, especially for wheeled SUGVs. Furthermore, the 6-wheeled design displays advantages over the 4-wheeled design in terms of power/energy consumption and mobility, since the 6-wheel configuration has the larger drawbar pull, smaller sinkage and lower power/energy consumption. When the 6-wheel configuration is compared with the track configuration, however, there is a clear trade-off. While the track configuration has lower sinkage and larger drawbar pull, and thus better mobility, it consumes more power and energy than the 6-wheel configuration.

8.2 A case study of an SUGV searching and retrieving

The search and retrieve problem is also a common task for SUGVs. In this type of tasks, an SUGV typically travels from one waypoint to another and comes back. The specific path is not pre-defined, which is different from the previous case study. Depending on the terrain conditions and the command from the remote-operator, the SUGV may have to take sharp turns.

In this case study, the SUGV is assumed to travel from a starting point to a target point and brings back a package to the starting point for inspection. The weight of the package 10 kg. We use a segment of the Mars Rover Curiosity's path on Mars as a reference and smooth the curve to create the path profile for the simulation. The SUGV is again the Packbot, described in Section 8.1. Figure 8.6 shows the path profile. As was mentioned above, this mission contains two trips: to the target point and come back along the same path. The only difference in the two trips is the total weight of the vehicle. The total travel distance is 271.95 meters. Figure 8.7 shows the turning radius of this path profile. The minimum turning radius of this path is 0.5 meter. A constant forward velocity of 0.5 m/s is used in the simulation. The mission is repeated twice on two different soils. One soil is the sandy soil, a soft soil, the same soil in the previous case study. The other soil is the LETE sand, a hard soil, according to Wong [10]. The properties of the LETE sand is defined in Table 8.3.

Mars Rover Curiosity's Path   Path Profile of the SUGV

Source:
http://curiosityrover.com/rovermap1.html
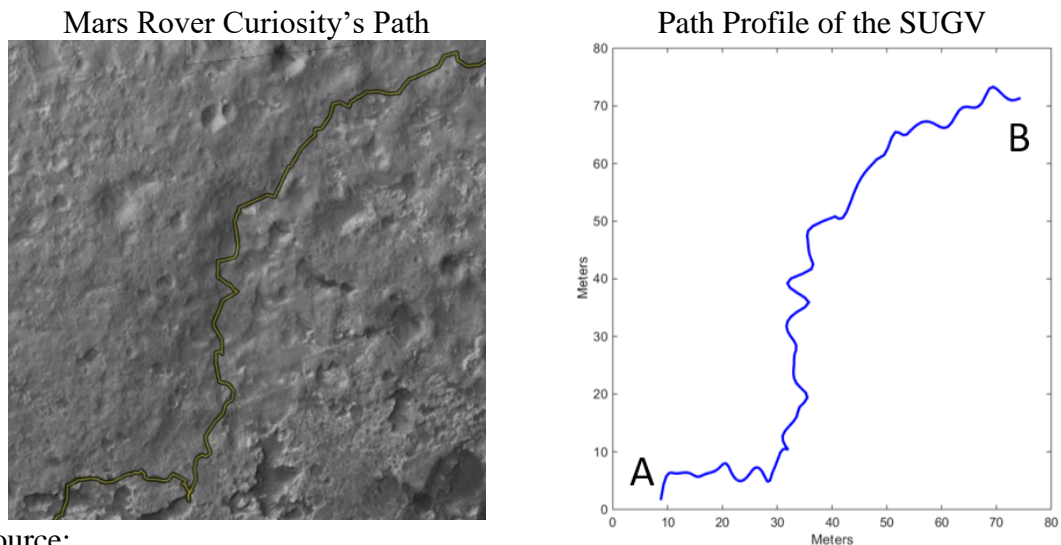
Figure 8.6 The path of the SUGV searching and retrieving

124
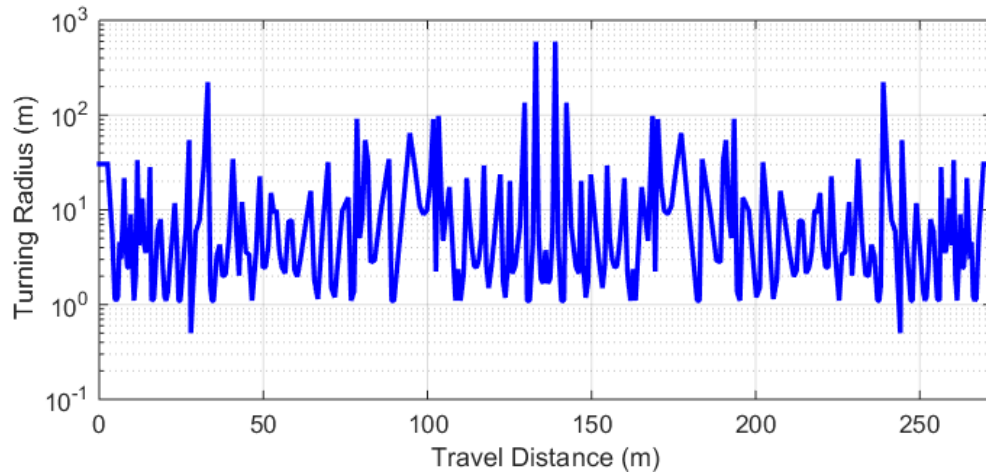
Figure 8.7 The turning radius of the path

Table 8.3 Parameters for the simulation terrain

	LETE Sand
n	0.79
c (Pa)	1300
ϕ (°)	31.1
k_c (N/m^{n+1})	102000
k_ϕ (N/m^{n+2})	5301000
K (m)	0.005

Source: [10]

Figure 8.8 to Figure 8.11 are the simulation results. Figure 8.8 shows the power consumption on two soils vs. the distance travelled. It can be seen from this figure that the wheeled SUGVs are more sensitive to soils than the tracked SUGV. The power consumption of the wheeled SUGVs reduces sharply on the hard soil than on the soft soil, while different soils have little effect of power consumption on tracked SUGVs. Moreover, power consumption increases sharply for the 4-wheeled SUGV at sharp turns. If the powertrain cannot provide the required power, the robot may get stuck in the sand or fail to follow the path. In many cases, this means mission failure, which should be avoided in any situations. Furthermore, the payload of the vehicle also affects the power consumption. It can be seen that in the return trip, the power consumption of all three designs increases, compared with the forward trip. This is because higher payload results in higher sinkage and higher terrain load. The wheeled design is more sensitive to load variation because of the much smaller contact areas.
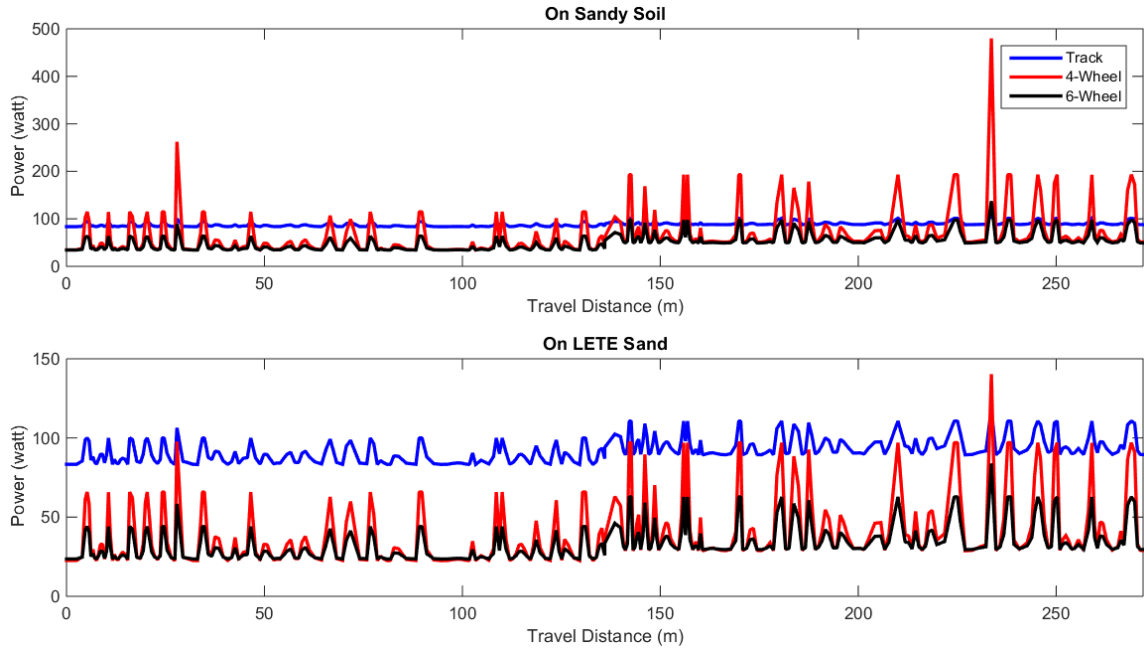
Figure 8.8 The power consumption in the search and retrieve problem
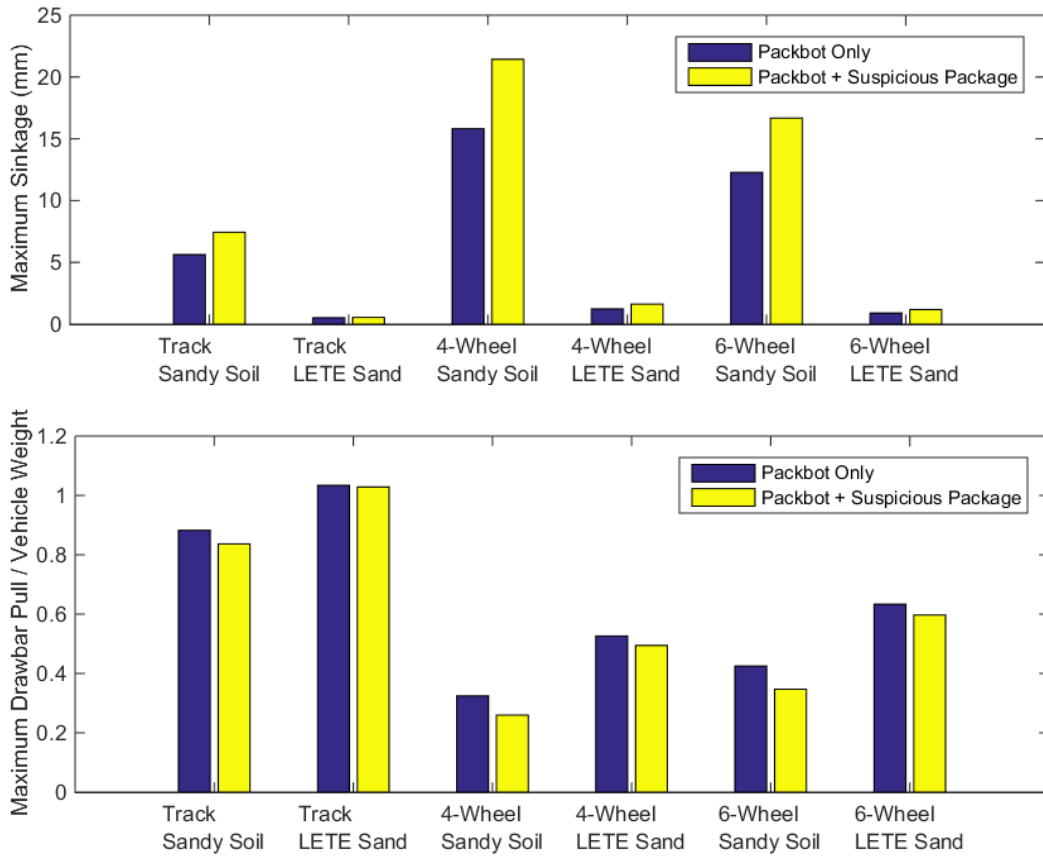
Figure 8.9 The mobility of the SUGVs in the search and retrieve problem

126
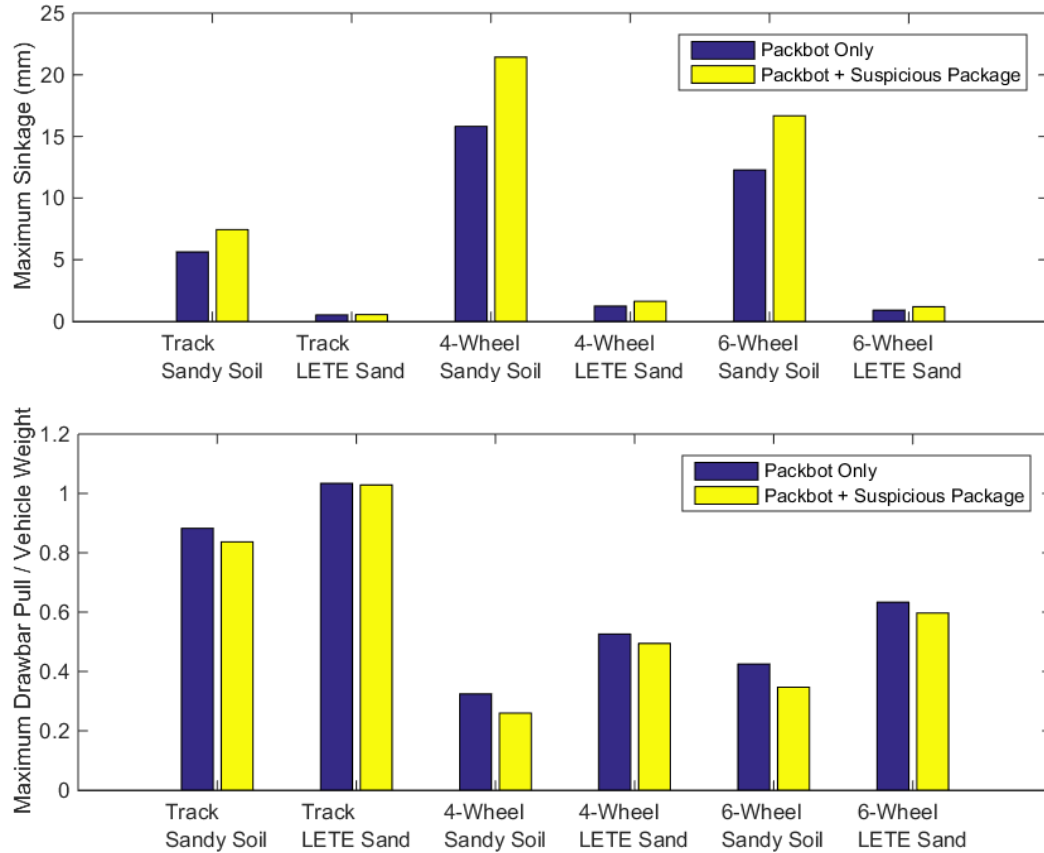
Figure 8.9 shows the mobility comparison of the three SUGVs on two soils. We choose the ratio of the maximum drawbar pull over the vehicle weight, and sinkage, as the two mobility indices. The larger the drawbar pull to the vehicle weight ratio is, the better the mobility is. On the other hand, smaller sinkage corresponds to better mobility. It can be seen for all the three configurations that the harder soil leads to better mobility, and higher payload leads to worse mobility. The impact of soils and payloads to the tracked design is the lowest. This is because the tracked design has larger contact surface. Not surprisingly, the tracked SUGV has better mobility than the wheeled SUGVs.

Figure 8.10 shows the total energy consumption of the three designs on two soils. It can be seen that the tracked SUGV consumes more energy than the wheeled SUGVs, and the 6-wheel SUGV consumes less energy than the 4-wheel SUGV. Moreover, the tracked SUGV consumes more energy on LETE sand than on sandy soil, while the two wheeled SUGVs consume less. That is because of the increase of the turning resistant moment during turning. For the tracked design this increase outweighs the decrease of the compaction resistance. However, for the wheeled designs this increase is smaller than the

decrease of the compaction resistance. Figure 8.11 shows the ratio of the energy consumption between internal energy consumption and energy consumption due to the vehicle-terrain interaction. The ratios of these three configurations on sandy soil and LETE sand are 84:16 vs. 81:19 for the tracked Packbot, 28:72 vs. 40:60 for the 4-wheeled Packbot, 35:65 vs. 49:51 for the 6-wheeled Packbot. The decrease of the percentage of the internal energy consumption for the tracked SUGV and the increase of this percentage for the wheeled SUGVs also explain the facts on Figure 8.10.
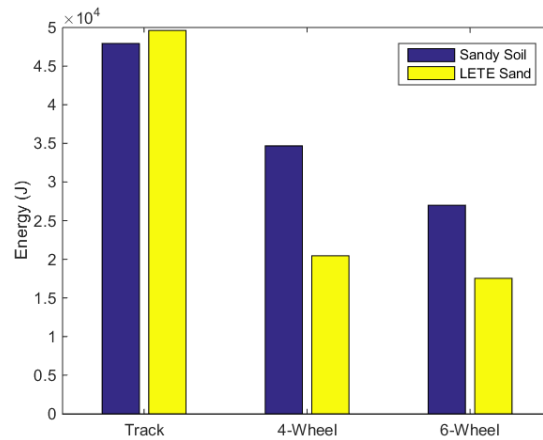
Figure 8.10 The energy consumption of the Packbot in the search and retrieve problem
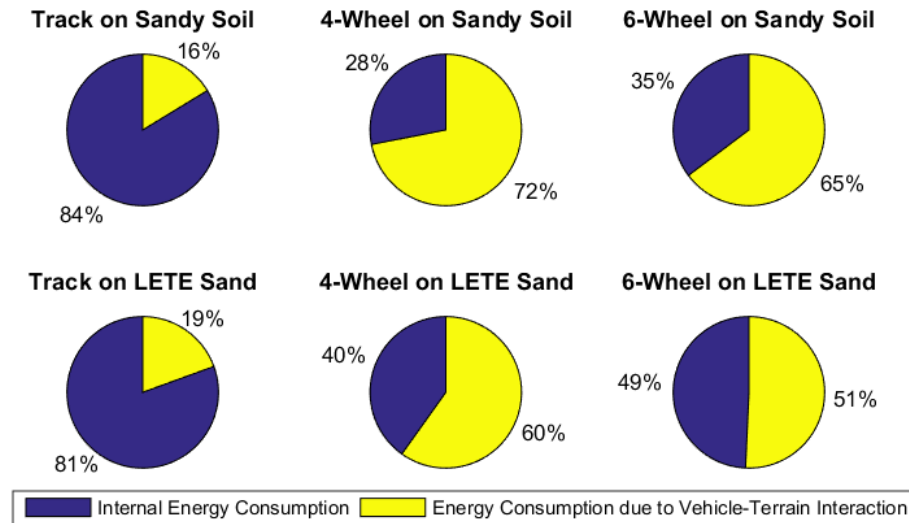
Figure 8.11 The ratio of the energy consumption between internal energy consumption and energy consumption due to the vehicle-terrain interaction

We also studied the sensitivity of soil parameters on the influence of the energy consumption and mobility of the SUGVs. We changed 2% of all the soil parameters of the sandy soil (1% increase and 1% decrease) and conducted the simulations on the three

configurations. Figure 8.12 shows the simulation results. For example, +1% soil parameters' change results in -0.01%, +0.68%, and +0.57% change of total energy, +1.27%, +1.46%, and +1.56% change of drawbar pull performance, and +2.51%, 2.41%, and 2.60% change of sinkage for the track design, 4-wheel design, and 6-wheel design respectively. We further analyzed the sensitivity of each soil parameter on energy consumption and mobility, shown in Figure 8.13, Figure 8.14, and Figure 8.15.
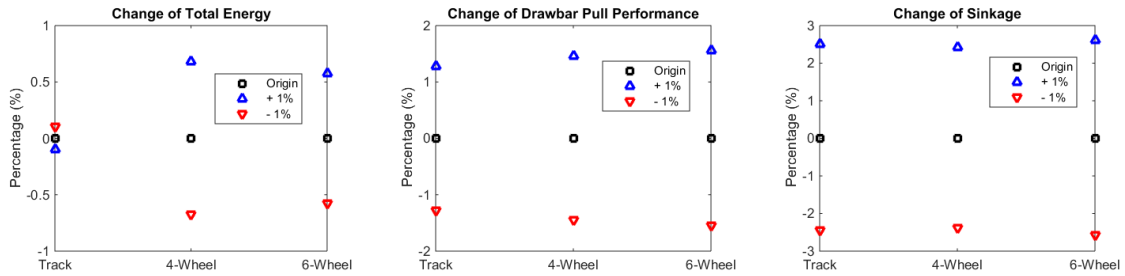
Figure 8.12 The sensitivity of soil parameters on total energy consumption, drawbar pull performance, and sinkage
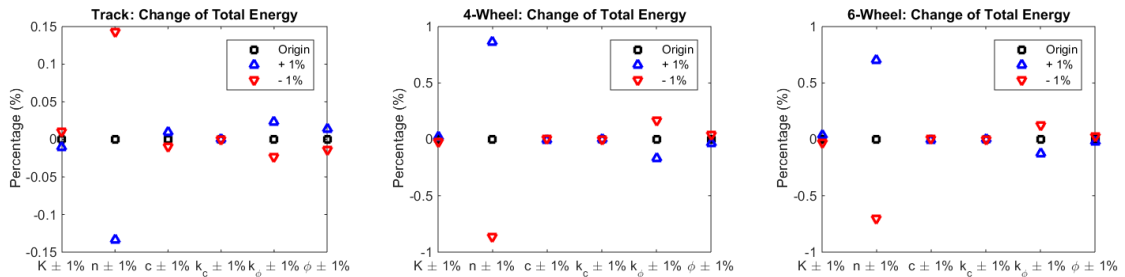
Figure 8.13 The sensitivity of soil parameters on total energy consumption
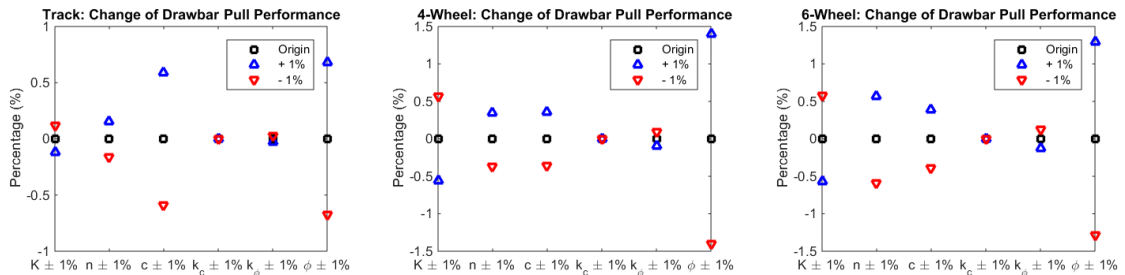
Figure 8.14 The sensitivity of soil parameters on drawbar pull performance
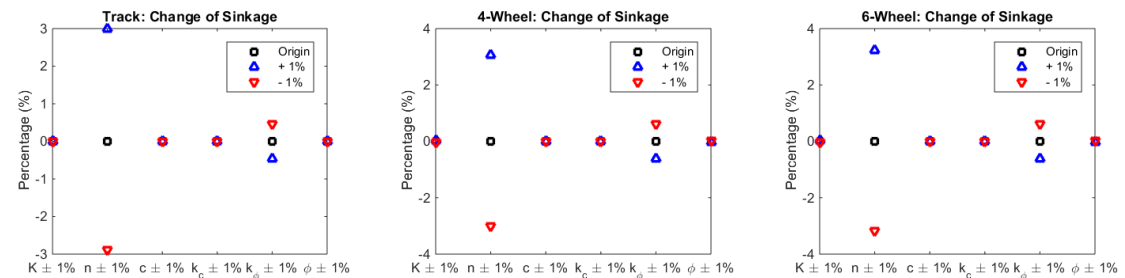
Figure 8.15 The sensitivity of soil parameters on sinkage

It can be seen in the energy graphs that soil parameter n has the highest sensitivity (e.g. +1% increase results in -0.13%, +0.86%, +0.7% change of total energy for the track, 4-wheel, and 6-wheel designs respectively), while k_c has the lowest (less than ±0.01% for all three designs). When n is larger, the soil is softer. The different trends of the energy consumption of the track and wheel designs further prove the conclusion that track design consumes more energy on harder terrains, while wheel designs consume less. For the drawbar pull performance, soil internal friction angle ϕ has the highest sensitivity (e.g. +1% increase results in +0.72%, +1.48%, and +1.28% change of drawbar pull performance for the track, 4-wheel, and 6-wheel designs respectively), because the increase of angle ϕ directly increases the maximum shear stress on the contact surface. Moreover, the drawbar pull performance of the track design is more sensitive to the soil cohesion c than the wheel designs, because of the larger contact area of the track design. For the sinkage, soil parameter n also dominates the sensitivity on all the three configurations (e.g. +1% increase results in +2.98%, +3.12%, ++3.18% change of sinkage for the track, 4-wheel, and 6-wheel designs respectively). When the soil is softer, vehicles have larger sinkage, indicating worse mobility.

Based on this case study, it can be seen that soil and payload significantly affect both the power consumption and mobility of all the three designs. All the three designs achieve better mobility on hard soil than on soft soil. However, the tracked SUGV consumes more energy on hard soil than on soft soil, while the wheeled SUGVs consume less. The wheel designs are more sensitive to soil than track designs. The 6-wheeled Packbot performs better than the 4-wheeled Packbot (smaller sinkage, larger drawbar pull, and smaller energy consumption). Comparing the tracked SUGV and the 6-wheeled SUGV, the former has better mobility, while the latter consumes less amount of energy and power consumption. Overall, the tracked Packbot is suitable for tasks that are on soft soils and considers mobility over power/energy consumption, while the 6-wheeled Packbot is suitable for tasks that are on hard soils and energy consumption is the top priority.

8.3 General discussion on tracked and wheeled SUGVs

In this section, a general design comparison on the power consumption and mobility, between tracked and wheeled SUGVs is conducted. We examine two driving maneuvers: driving straight at a constant forward velocity of 0.2 m/s, and skid steering at a constant turning radius of 2 m and forward velocity of 0.2m/s.

We study the same three configurations (track, 4-wheel, or 6-wheel), with three levels of key parameter values in vehicle mass, track/wheel width, sprocket/wheel radius, track length/wheel base, and tread of the vehicle. Thus there are $3^6 = 729$ total design candidates. The values of the design parameters in this simulation are listed in Table 8.4. These are typical values for SUGVs. The internal resistance coefficients of the test robot are again used, which are assumed to stay unchanged with robot parameters (but of course they change with the configurations).

Table 8.4 Parameters used in design study of Section 8.3

Design Parameters	Values
Configuration of the drivetrain	Track, 4-Wheel, 6-Wheel
Vehicle mass (kg)	10, 20, 30
Track / wheel width (m)	0.05, 0.125, 0.2
Sprocket / wheel radius (m)	0.08, 0.1, 0.12
Track length / wheel base (m)	0.5, 0.7, 0.9
Tread of the vehicle (m)	0.3, 0.4, 0.5

The simulation results are plotted on a power consumption vs. mobility graph. The X-axis is the ratio between the maximum drawbar pull over the vehicle weight, indicating the mobility, and the Y-axis is the power consumption. Figure 8.16 and Figure 8.17 show the simulation results for these designs. There are fewer points in Figure 8.16 than in Figure 8.17. The reason is that in the driving straight condition, wheel base and tread of the vehicle have no effects on the power consumption and mobility for wheeled SUGVs. And tread of the vehicle has no effects on the power consumption and mobility for tracked SUGVs.

In the straight-driving condition, most of the track designs consume more power than both wheel designs, and 6-wheel designs consume more power than 4-wheel design.

However, in the sharp turning condition, some of the wheel designs, especially the 4-wheel designs, consume more power than the track designs. If there is mobility concerns, or when the operating conditions involve a lot of sharp turning, track designs might provide more reliable performance over the wheeled designs.
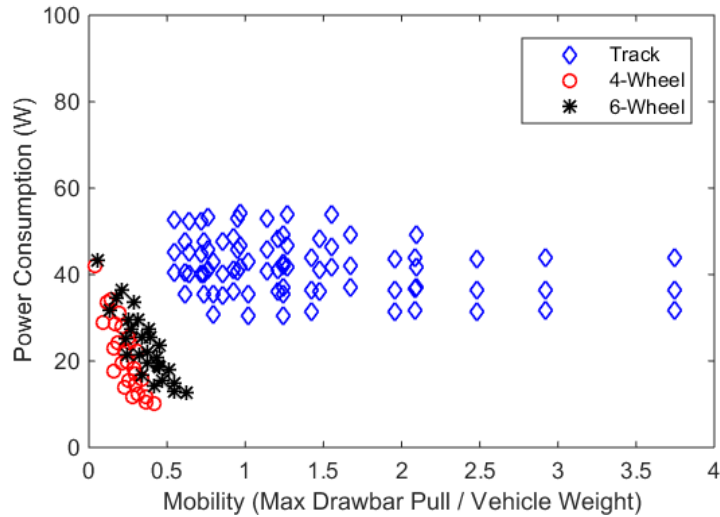
Figure 8.16 Performance of the designs while driving straight
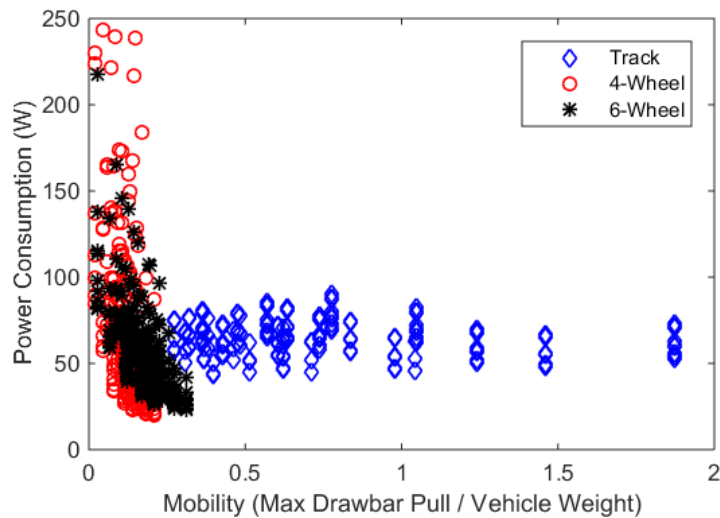
Figure 8.17 Performance of the designs while turning

Among the 729 design candidates, the best design in each configuration is plotted in Figure 8.18. The parameters of each design are listed in Table 8.5.

It can be seen that for both tracked and wheeled configurations, the best designs use the lightest vehicle mass, widest track/wheel width, largest vehicle tread, and largest sprocket/wheel radius. This is because lighter vehicle mass leads to lower sinkage and

resistances, and better mobility. Wider track/wheel width helps to increase the contact area, resulting in larger drawbar pull and better mobility. Larger vehicle tread helps to increase the turning moment for given thrust forces, reducing the power consumption during turning.

Larger sprocket/wheel radius corresponds to slower wheel rotational speed for a given forward velocity. Lower rotational speed leads to lower internal power consumption. It should be noted here that the wheel radius cannot be too large, because when the wheel radius is large, large torque on the axle is required to satisfy the thrust force. In order to provide large axle torque, transmission with large reduction ratio is required. That will drastically reduce the efficiency of the transmission, resulting in larger power consumption of the whole system.

The only parameter that affects track/wheel vehicles differently is the track length/wheel base. For tracked SUGVs, longer track length leads to larger contact area and larger shear displacement at the contact surface, with larger drawbar pull as a result. Longer track, however, increases the turning resistance moment, resulting in higher skid steering power consumption. Simulation results show that the gain in mobility outweighs the increase in power consumption. For wheeled SUGVs, especially in the skid steering maneuver, shorter wheel base reduces power consumption, because of a smaller turning resistance moment. The wheel base has no effect on the drawbar pull performance. Thus tracked SUGVs should use longer tracks, while wheeled SUGVs should use a shorter wheel base.

Figure 8.18 The three best designs

Table 8.5 The parameters of the superior designs

	Track	4-Wheel	6-Wheel
Vehicle Mass (kg)	10	10	10

Track or Wheel Width (m)	0.2	0.2	0.2
Sprocket or Wheel Radius (m)	0.12	0.12	0.12
Track Length or Wheel Base (m)	0.9	0.5	0.5
Vehicle Tread (m)	0.5	0.5	0.5

8.4 Summary

In this chapter, tracked and wheeled SUGVs are compared, with the focus on power consumption and mobility. Two case studies (patrolling an area and search and retrieve problems) were conducted by analyzing three configurations (track, 4-wheel, and 6-wheel). Subsequently, a general design comparison was also presented. The best design in each configuration was selected and analyzed.

It was found that track design has better mobility, while in most cases the wheel system consumes less power and energy. If power/energy consumption is the top priority of a mission and on hard soils, then the 6-wheel design may be selected over the track design, and if on soft soils and the mobility is the top priority, then the track design may be more appropriate. It should be stated that this comparison between track and wheel on SUGVs only includes power consumption and mobility; a thorough comparison may consider other factors, such as reliability, maintainability, cost, safety, etc.

CHAPTER 9
Conclusions and Future Work

9.1 Conclusions

This dissertation focused on the power consumption modeling for both tracked and wheeled SUGVs running off-road. The primary objective is to develop an accurate and fast power consumption model for both tracked and wheeled SUGVs that helps to improve system design and control in terms of power consumption and mobility.

As discussed in Chapter 1, skid steering is widely used on SUGVs because of its simplicity, robustness, and reliability. However, skid steering can consume large amounts of power due to the unavoidable slip between the running gear and terrain. Thus any accurate power consumption model of SUGVs must include skid steering models. The modeling of skid steering is non-trivial because of the track/wheel-terrain interaction and the distributed nature of the shear stress along the contact area. This dissertation primarily addressed the development of skid steering models for both tracked and wheeled SUGVs.

In Chapter 2, terramechanics knowledge was briefly introduced and single track/wheel-terrain interaction models were reviewed and discussed. These models described the relationship among pressure, sinkage, and compaction resistance, and that among slip ratio, shear displacement, and shear stress. The inputs to the models were forward velocity, track/wheel rotational speed, and normal load, and the outputs were the forces and moments at the contact surface and the torque on the axle. These models served as the knowledge base for the vehicle-terrain interaction.

In Chapter 3, the skid steering mechanism was studied and analyzed. Three widely used skid steering models on tracked vehicles (Steeds' model, Wong's model, and the ICR model) were reviewed and compared and their strengths and weaknesses were discussed. Closed form solutions can be obtained in both Steeds' and the ICR models. For Wong's

model (3 DOF: slip ratio of the outer and inner drivetrain and the offset of the turning center), we used the Newton-Raphson numerical method to obtain the steady-state solution. Simulations of these three models on tracked vehicles were conducted and results were compared and analyzed. Wong's model was shown to be the most accurate among these three, yet it is complicated and has high computation requirement. Steeds' and the ICR models were shown to be superior in computation efficiency, yet their accuracy is inadequate.

In Chapter 4, we extended Wong's skid steering model for tracked vehicles to wheeled vehicles. A 5 DOF skid steering model for wheeled vehicles was developed, in contrast to Wong's 3 DOF skid steering model for tracked vehicles. We considered the sinkage of the outer and inner drivetrains as the two additional unknown variables, since the sinkage can affect slip ratio in steady state and vice versa. Two more equations (vertical force balance and roll moment balance) were used to solve the steady-state solution. The Newton-Raphson numerical method was again used.

In Chapter 5, we focused on speeding up the computation. A fast computation skid steering model for tracked vehicles was developed. The fast computation model separates the computation-intensive part (track-terrain interaction) from the computation-light part (vehicle 3 DOF dynamics). Look-up maps for the computation-intensive part were pre-generated offline. Although this model drastically improves the computation speed, it is not robust against variations in vehicle parameters or soil properties.

To overcome the robustness problems, a new skid steering model, the Finite Element Skid Steering (FESS) model was developed in Chapter 6. This model combined both tracked and wheeled vehicle cases and achieved improved computation efficiency by formulating a new method to calculate the shear displacement along the discretized contact surface. Quadratic approximation of the normal shear stress at the wheel-terrain interaction surface was utilized to further improve the computation efficiency of the wheel cases. The simulation results showed high accuracy of the FESS model vs. Wong's model, while the computation speed increased about 70 times in the track cases and about 200 times in the wheel cases.

In Chapter 7, a 6-wheel-drive track/wheel interchangeable SUGV was designed and built for experimental validation of the FESS model. Experiment results showed that the

internal resistance of the track configuration is much larger than that of the wheeled configuration, and most of the energy is consumed between the track and the sprocket. Field experiments were conducted in a sand bin in an indoor environment. A camera was used to capture the vehicle motion. Each image was analyzed and the vehicle states were calculated. Torque and power consumption were measured to validate against the FESS model. Results indicated high accuracy of the FESS model.

In Chapter 8, the tradeoff between track and wheel designs for SUGVs running off-road was addressed. Using the FESS model, the power consumption and mobility were studied and compared between tracked and wheeled SUGVs. Two case studies were conducted based on an imaginary Packbot with three possible configurations (track, 4-wheel, and 6-wheel). Simulation results indicated that the 6-wheeled Packbot has advantages over the 4-wheeled Packbot with regard to power/energy consumption and mobility. However, when the 6-wheeled Packbot was compared with the tracked Packbot, it was harder to determine the better choice, since the tracked Packbot had better mobility, but consumed more power and energy than the 6-wheeled one. At last, a general design comparison in terms of the power consumption and mobility among track, 4-wheel, and 6-wheel configurations was studied. A design pool of 729 candidates was simulated. The best design in each configuration was selected and analyzed. The general conclusion regarding track vs. wheel, within the category of power consumption and mobility for an SUGV, is that if power/energy consumption is the top priority of a mission, then the 6-wheeled design may be better than the track design, and if mobility is the top priority, then the tracked design may be more appropriate. The decision between track and wheel also rests on additional considerations such as reliability, maintainability, cost, and safety.

9.2 Future work

In this dissertation, we have developed several power consumption models for tracked and wheeled SUGVs running off-road. Experiments have also been conducted. Some potential future studies are listed below:

9.2.1 Further improvement of the computation efficiency of the FESS model for onboard control purposes

Although the FESS model was found to be computationally efficient, compared with Wong's model, there is still room of improvements of the computation efficiency for onboard control purposes. Possible improvements of the calculation speed of the FESS model includes better solving method and further simplification of the normal and shear stress calculation on the contact surface, especially for the wheel-terrain interaction. Faster numerical methods will be definitely beneficial in improving calculation efficiency. Further simplification of these calculations with appropriate assumptions for SUGVs can increase the computation speed of the vehicle-terrain interaction. If the closed form solution of the system can be found, it will drastically increase the computation speed and achieve comparable computation efficiency against Steeds or ICR models.

9.2.2 Rough surface locomotion

SUGVs pose a new challenge to the terramechanics field because of their smaller size. As a matter of scale, surface profiles that are considered "smooth" for large, heavy vehicles may become "rough" for small robots. Rough terrain can in turn cause vibrations in the vehicle-terrain interaction. Both the amplitude and the frequency of these vibrations were known to not only influence the contact surface, but also the normal and shear forces developed at the interface [52] [53] [54] [55]. As a vehicle travels over rough soil, not only is the terrain profile modified by the interaction, the vibrations generated by the interaction can change the physical properties of the soil itself [54] [55]. Thus a better model to address the soil roughness can aid in better design of the vehicle, accurate power or energy estimation of the mission, and vehicle control.

9.2.3 Modeling of other steering systems on SUGVs

Although the skid steering system is widely used on SUGVs for its simplicity, robustness and reliability, other steering systems (Ackermann steering system and 4-wheel steering system) are also used on SUGVs, especially wheeled SUGVs. For example, the Mars Rover is a 6-wheeled robot with 4-wheel steering capability [56]. The power consumption, mobility, reliability, robustness, cost, safety and many other aspects of these

steering mechanisms on SUGVs should be studied, in order to provide better knowledge for SUGV design and control.

APPENDIX

A

Specifications of DES 70/10 Servoamplifier

4-Q-EC Servoamplifier Data

`CAN` `RS232` `GUI`

maxon special program

DES 50/5 4-Q-EC Servoamplifier
Digital servoamplifier with sinusoidal commutation for perfectly controlling EC motors with Hall sensors and encoder and an output of up to 250 watts.

DES 70/10 4-Q-EC Servoamplifier
Digital servoamplifier with sinusoidal commutation for perfectly controlling EC motors with Hall sensors and encoder and an output of up to 700 watts.

Operating modes		
	Speed controller, current controller	Speed controller, current controller
Electrical Data		
Operating voltage V_{CC}	12 - 50 VDC	24 - 70 VDC
Max. output voltage	0.9 x V_{CC}	0.9 x V_{CC}
Max. output current I_{max}	15 A	30 A
Continuous output current I_{cont}	5 A	10 A
Switching frequency of power stage	50 kHz	50 kHz
Max. efficiency	92 %	92 %
Band width current controller	1 kHz	1 kHz
Max. speed (1 pole pair)	25 000 rpm	25 000 rpm
Built-in motor choke per phase	160 µH / 5 A	Minimum required terminal inductance 400 µH
Input		
Set value configurable (1024 Steps)	-10…+10 V/0…+5 V	-10…+10 V/0…+5 V
"Enable"	+2.4…50 V	+2.4…50 V
Digital 1 (Switch "Monitor n" / "Monitor I")	+2.4…50 V	+2.4…50 V
Digital 2 (Switch speed- / current controller)	+2.4…50 V	+2.4…50 V
STOP	+2.4…50 V	+2.4…50 V
Encoder signals	A, A\, B, B\, I, I\ max. 1 MHz 3-channel encoder is required	A, A\, B, B\, I, I\ max. 1 MHz 3-channel encoder is required
Hall sensor signals	H1, H2, H3	H1, H2, H3
Output		
Monitor configurable	-10…+10 V/0…+5 V	-10…+10 V/0…+5 V
Status reading "Ready"	Open Collector, max. 30 V (I_L < 20 mA)	Open Collector, max. 30 V (I_L < 20 mA)
Voltage outputs		
Encoder supply voltage	+5 VDC, max. 100 mA	+5 VDC, max. 100 mA
Hall sensors supply voltage	+5 VDC, max. 50 mA	+5 VDC, max. 50 mA
Auxiliary voltage		+5 VDC, max. 20 mA
Interface		
RS232	RxD; TxD (max. 115 200 bit/s)	RxD; TxD (max. 115 200 bit/s)
CAN	high; low (max.1 Mbit/s)	high; low (max.1 Mbit/s)
Trim potentiometer	n_{max}, Offset, I_{max}, gain	n_{max}, Offset, I_{max}, gain
Indicator	Bi-colour LED, green = READY, red = ERROR	Bi-colour LED, green = READY, red = ERROR
Ambient temperature and humidity range		
Operation	-10…+45°C	-10…+45°C
Storage	-40…+85°C	-40…+85°C
No condensation	20…80%	20…80%
Mechanical Data		
Weight	Approx. 430 g	Approx. 400 g
Dimensions (L x W x H)	180 x 103 x 26 mm (see page 395)	180 x 103 x 29 mm (see page 395)
Mounting threads	Flange for M4-screws	Flange for M4-screws
Connections	See page 395	See page 395
Part Numbers		
	205679 DES 50/5, digital 4-Q-EC Servoamplifier in module housing	**228597** DES 70/10, digital 4-Q-EC Servoamplifier in module housing
Accessories		
	223774 Encoder adapter according to DIN41651 screw type terminal block **235811** DSR 70/30 Shunt regulator	**347919** Choke module 3 x 0.1 mH, 10 A **223774** Encoder adapter according to DIN41651 on screw type terminal block **235811** DSR 70/30 Shunt regulator

B

Specifications of Maxon EC-45 Motor

EC-4pole 45 □45 mm, brushless, 300 Watt, CE approved
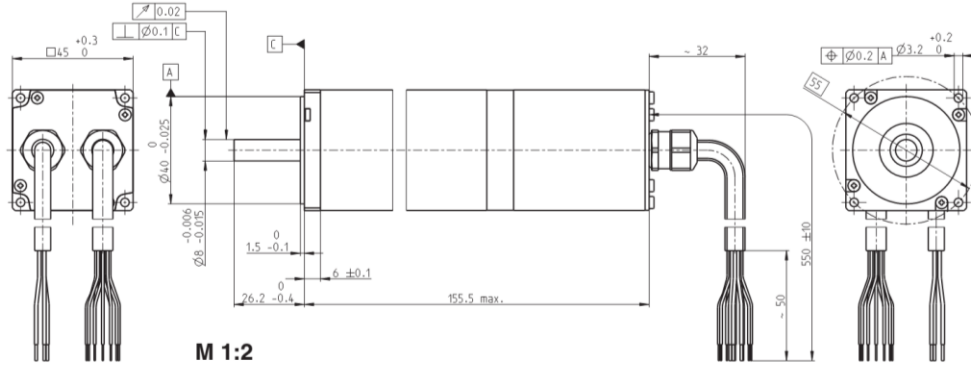
M 1:2

■ Stock program
□ Standard program
▨ Special program (on request)

Order Number

		with encoder	283150

Motor Data (provisional)

Values at nominal voltage

1	Nominal voltage	V	48.0
2	No load speed	rpm	4010
3	No load current	mA	193
4	Nominal speed	rpm	3580
5	Nominal torque (max. continuous torque)	mNm	635
6	Nominal current (max. continuous current)	A	5.61
7	Stall torque	mNm	7690
8	Starting current	A	67.6
9	Max. efficiency	%	90

Characteristics

10	Terminal resistance phase to phase	Ω	0.710
11	Terminal inductance phase to phase	mH	0.677
12	Torque constant	mNm / A	114
13	Speed constant	rpm / V	84.0
14	Speed / torque gradient	rpm / mNm	0.524
15	Mechanical time constant	ms	2.02
16	Rotor inertia	gcm²	368

Specifications

Thermal data
17 Thermal resistance housing-ambient   1.97 K / W
18 Thermal resistance winding-housing   0.718 K / W
19 Thermal time constant winding   34.3 s
20 Thermal time constant motor   1600 s
21 Ambient temperature   -10 ... +100°C
22 Max. permissible winding temperature   +125°C

Mechanical data (preloaded ball bearings)
23 Max. permissible speed   10000 rpm
24 Axial play at axial load   < 20.0 N   0 mm
                                              > 20.0 N   0.14 mm
25 Radial play   preloaded
26 Max. axial load (dynamic)   20 N
27 Max. force for press fits (static)   170 N
      (static, shaft supported)   5000 N
28 Max. radial loading, 5 mm from flange   140 N

Other specifications
29 Number of pole pairs   2
30 Number of phases   3
31 Weight of motor   1130 g
      Protection to   IP54

Values listed in the table are nominal.

Connection Motor (Cable AWG 18)
Cable 1   Motor winding 1
Cable 2   Motor winding 2
Cable 3   Motor winding 3

Option
Temperature monitoring, PTC resistance
   R 20°C < 0.3 kΩ
   R 130°C = 7.0 ... 35 kΩ

Operating Range

n [rpm]

300 W

283150

M [mNm]
i [A]

Comments

■ **Continuous operation**
In observation of above listed thermal resistance (lines 17 and 18) the maximum permissible winding temperature will be reached during continuous operation at 25°C ambient.
= Thermal limit.

□ **Short term operation**
The motor may be briefly overloaded (recurring).

— **Assigned power rating**

Integrated encoder R35i   Overview on page 16 - 21

Connection Encoder (Cable AWG 26)

green	(Pin 1)	Channel A	
yellow	(Pin 2)	Channel Ā	
red	(Pin 3)	Channel B	
blue	(Pin 4)	Channel B̄	
pink	(Pin 5)	Channel I (Index)	
grey	(Pin 6)	Channel Ī (Index)	
violet	(Pin 7)	Commutation signal S 1	
red/blue	(Pin 8)	GND 2	
black	(Pin 9)	Commutation signal S 2	
white/green	(Pin 10)	V_cc 2	
grey/pink	(Pin 11)	Commutation signal S 3	
	(Pin 12)	n.c.	
white	(Pin 13)	V_cc 1	
brown	(Pin 14)	GND 1	

Counts per turn	2048
Number of channels	3
Max. operating frequency (kHz)	200
Supply voltage	5 V ± 5 %
Output signal	RS 422
Phase shift Φ (nominal)	90°e
Logic state width s	min. 45°e
Index pulse width (nominal)	90° ± 45°
Operating temperature range	-10 ... +100°C
Moment of inertia	≤ 3.11 gcm²

Recommended Electronics:

DECS 50/5	Page 289
DEC 50/5	291
DEC Module 50/5	291
DEC 70/10	297
DES 50/5	298
DES 70/10	298
EPOS2 70/10	305
Notes	**20**

May 2010 edition / subject to change

C

Specifications of ShearTrac II

Geocomp
CORPORATION

Technologies to manage risk for infrastructure

Benefits and Features

- Choose load capacity to fit user needs up to 9 kN (2,000 lbs.)

- Total automation, control, data collection and reporting of test results

- Prepare tables and plots of report quality within minutes of completing a test

- Geo-NET compatibility lets unit be accessed and controlled over a computer network

- Generate columns of data for easy reduction using your own spreadsheet software

- Accurate displacement rate control from 0.00003 to 7.5 mm per minute (0.000001 to 0.3 inches per minute)

- Full automation of residual shear testing

- Stand alone through front keypad and LCD menu capability

Applicable Test Standards

- ASTM D3080 / T236 Direct Shear Testing of Soils under Consolidated Drained Conditions

For More Information Contact:

Rachid Hankour, Ph.D.
Vice President and Director of Lab Systems
125 Nagog Park   t 978.635.0012
Acton, MA 01720   f 978.635.0266

RH@geocomp.com

Direct Residual Shear
ShearTrac II

Standard ShearTrac II System
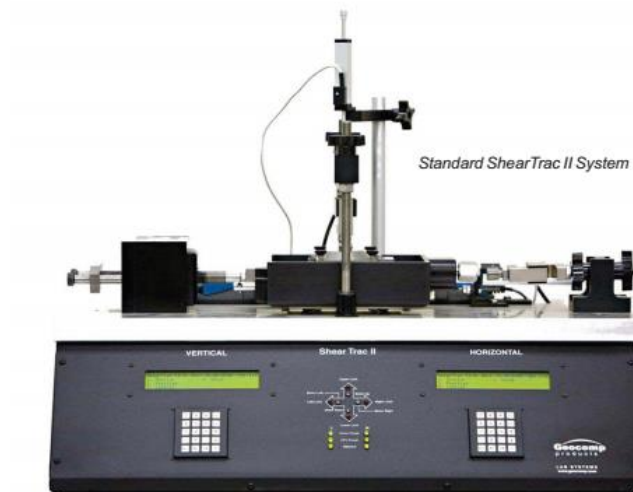
The ShearTrac II system is capable of performing the consolidation and shearing phases of a standard direct shear and residual shear test under full automatic control. The system consists of a computer-controlled unit that utilizes micro-stepper motors to apply the vertical and horizontal loads to the soil specimen. Versions of the unit are available to produce vertical and horizontal loads up to 9 kN (2000 lbs.).

The system is capable of running a consolidation phase for up to 32 increments automatically. Horizontal shearing can be applied at a specified rate of deformation or at a specified rate of horizontal force change, or at a specified set of force steps of a specified duration. The system is capable of displaying the current status of a test and graphically portraying the progress of the test in real time. The system includes the capability for the operator to alter the test process and conditions at any stage of the test. The system is also capable of performing repeated direct shear tests to determine residual strength based on a specified number of repeated cycles.

The system comes complete with hardware and software for recording all test input data and settings of selected test parameters, performing standard engineering calculations on the data, and producing graphically plotted and printed output in the standard Corps format, in accordance with Engineer Manual (EM 1110-2-1906), Laboratory Soils Testing, Appendix IX and Appendix IXa.

www.geocomp.com   125 Nagog Park   Acton, MA 01720   978.635.0012

Technical Specifications

Capacity	Up to 1.1 kN (2,500 lbs.) vertical and horizontal
Vertical Motor	Stepper motor with built-in controls for vertical load
Horizontal Motor	Stepper motor with built-in controls for horizontal load
Speed Range	0.00003 to 15 mm per minute (0.000001 to 0.6 in. per minute)
Horizontal Travel	±12.5 mm (±0.50 in.) resolved to 0.0013 mm (0.00005 in.)
Vertical Travel	25.45 mm (1.00 in.) resolved to 0.0013 mm (0.00005 in.)
Power	110/220 V, 50/60 Hz, 1 phase

Dimensions	228 x 560 x 762 mm (9 x 22 x 30 inches)
Weight	63 kg (140 lbs.)

ShearTrac II	Load capacity
ST-1000	4.5 kN (1,000 lbs.)

Accessories

ShearTrac II accessories including ShearTrac II box to test square or round samples up to 101 mm (4 in.) dimension/diameter, includes top and bottom porous stones.

Geo-NET-PC Network card and cable to link ShearTrac II to PC.

SHEAR Software package to automatically run and report direct/residual shear test on ShearTrac II.

Typical Test Output

User-friendly Interface
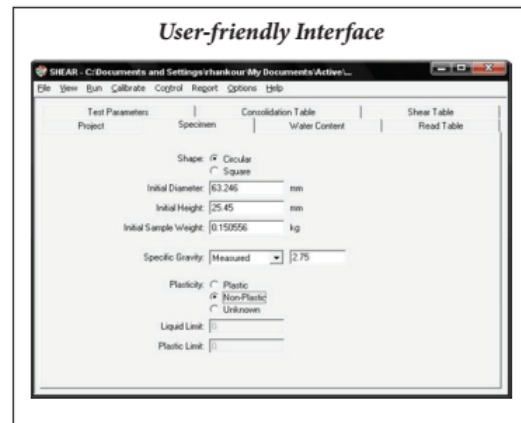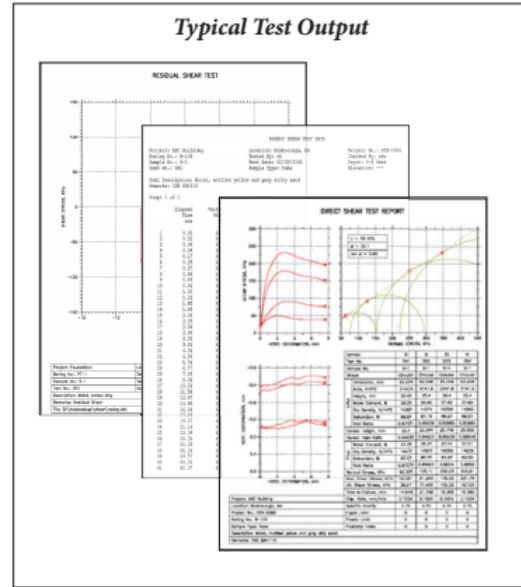
Trace of the Test Robot and the Curve Fitted Circle
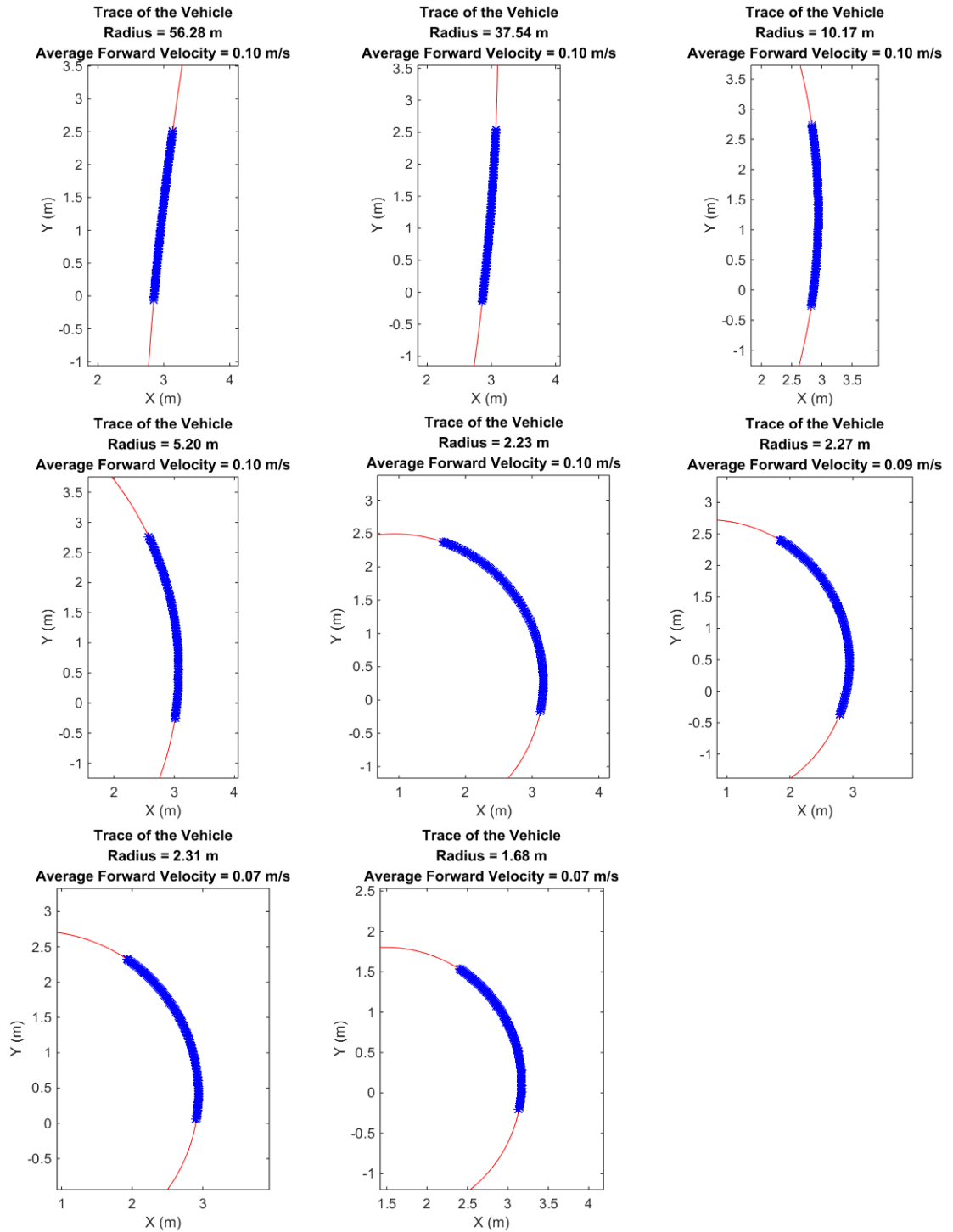
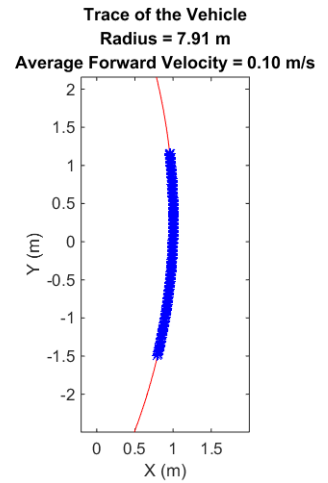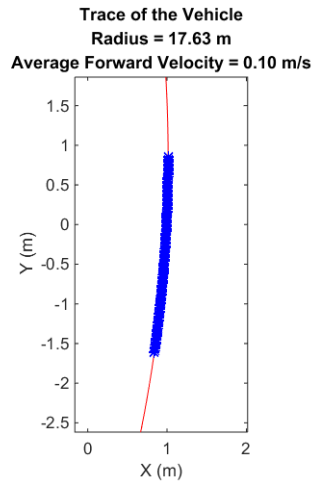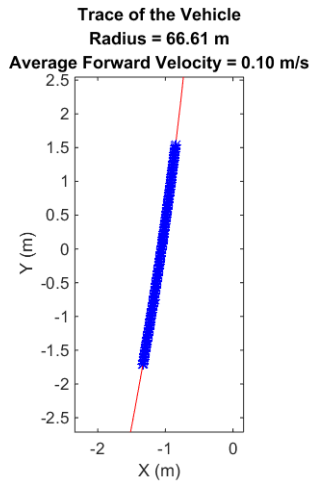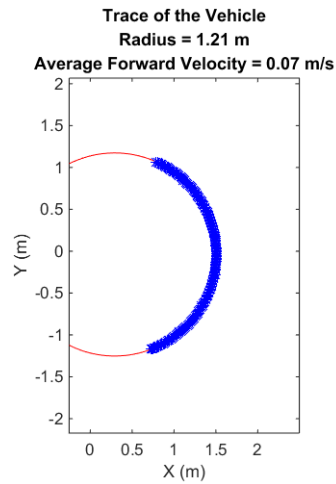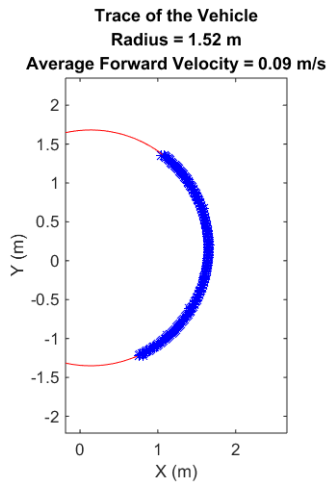Test Robot in 4-Wheel Configuration Forward Velocity = 0.1 m/s

Test Robot in 4-Wheel Configuration Forward Velocity = 0.2 m/s

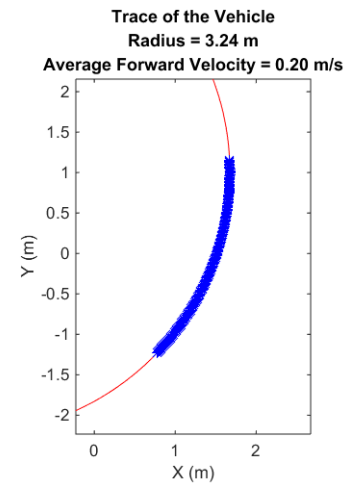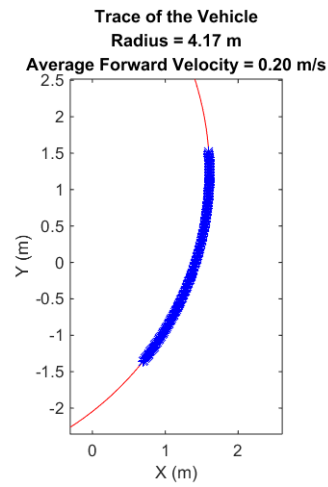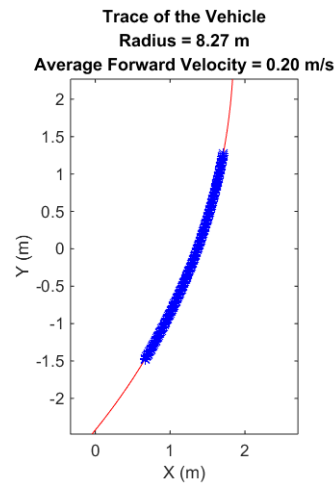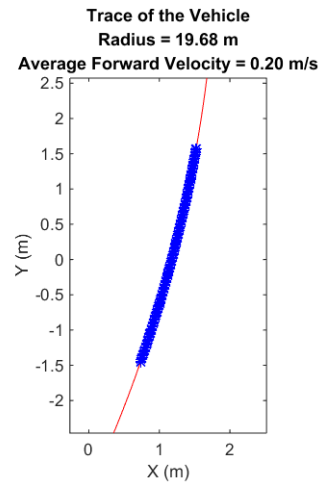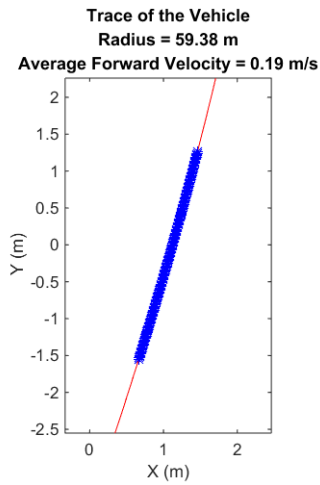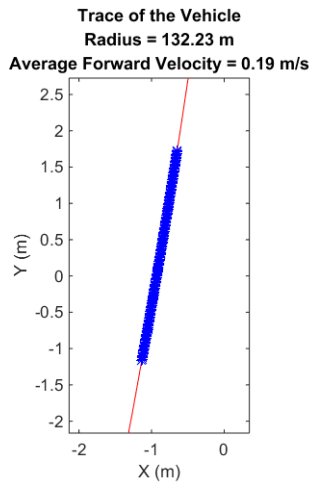**Trace of the Vehicle**
Radius = 85.62 m
Average Forward Velocity = 0.20 m/s

Trace of the Vehicle
Radius = 33.11 m
Average Forward Velocity = 0.18 m/s

Trace of the Vehicle
Radius = 28.14 m
Average Forward Velocity = 0.20 m/s

Trace of the Vehicle
Radius = 11.15 m
Average Forward Velocity = 0.20 m/s

Trace of the Vehicle
Radius = 5.16 m
Average Forward Velocity = 0.20 m/s

Trace of the Vehicle
Radius = 4.06 m
Average Forward Velocity = 0.19 m/s

Trace of the Vehicle
Radius = 2.89 m
Average Forward Velocity = 0.19 m/s

Trace of the Vehicle
Radius = 2.43 m
Average Forward Velocity = 0.20 m/s

Trace of the Vehicle
Radius = 2.36 m
Average Forward Velocity = 0.18 m/s

145
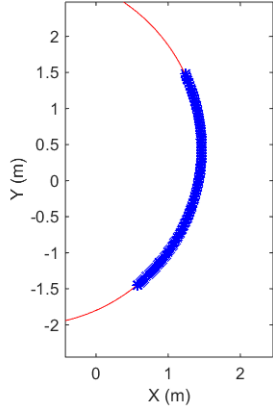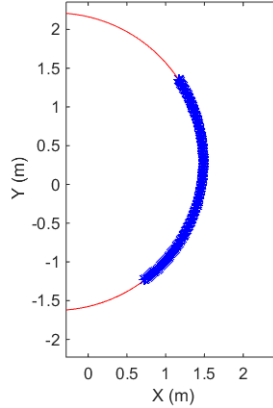
Test Robot in 6-Wheel Configuration Forward Velocity = 0.1 m/s

Trace of the Vehicle
Radius = 1.52 m
Average Forward Velocity = 0.09 m/s

Trace of the Vehicle
Radius = 1.21 m
Average Forward Velocity = 0.07 m/s

Test Robot in 6-Wheel Configuration Forward Velocity = 0.2 m/s

Trace of the Vehicle
Radius = 132.23 m
Average Forward Velocity = 0.19 m/s
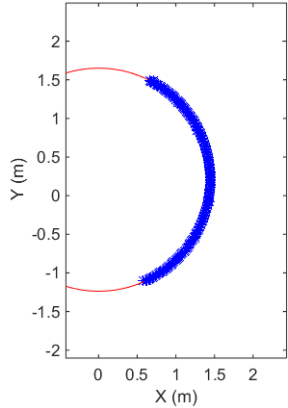
Trace of the Vehicle
Radius = 59.38 m
Average Forward Velocity = 0.19 m/s

Trace of the Vehicle
Radius = 19.68 m
Average Forward Velocity = 0.20 m/s

Trace of the Vehicle
Radius = 8.27 m
Average Forward Velocity = 0.20 m/s

Trace of the Vehicle
Radius = 4.17 m
Average Forward Velocity = 0.20 m/s

Trace of the Vehicle
Radius = 3.24 m
Average Forward Velocity = 0.20 m/s

Trace of the Vehicle
Radius = 2.45 m
Average Forward Velocity = 0.20 m/s

Trace of the Vehicle
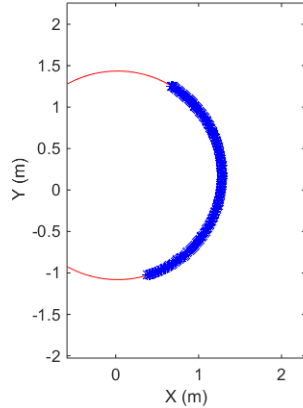**Radius = 1.92 m**
Average Forward Velocity = 0.19 m/s

Trace of the Vehicle
Radius = 1.62 m
Average Forward Velocity = 0.18 m/s
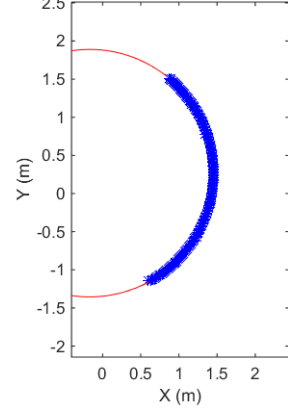
Trace of the Vehicle
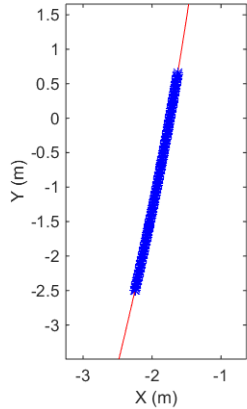**Radius = 1.44 m**
Average Forward Velocity = 0.17 m/s

Trace of the Vehicle
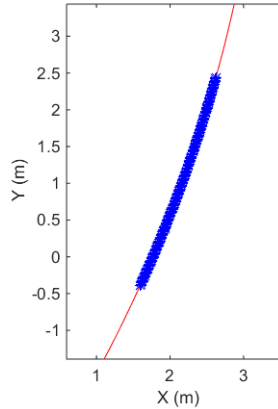**Radius = 1.26 m**
Average Forward Velocity = 0.17 m/s

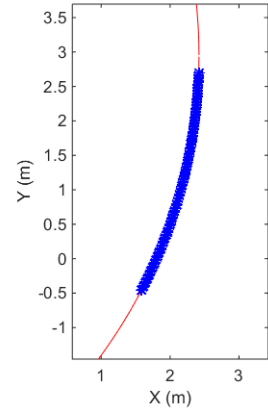Test Robot in Track Configuration Forward Velocity = 0.1 m/s

Trace of the Vehicle
Radius = 59.06 m
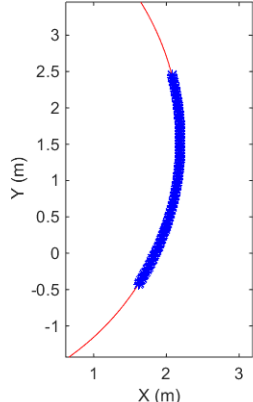**Average Forward Velocity = 0.10 m/s**

Trace of the Vehicle
Radius = 19.44 m
Average Forward Velocity = 0.10 m/s

Trace of the Vehicle
Radius = 7.40 m
Average Forward Velocity = 0.10 m/s

148

Trace of the Vehicle
Radius = 3.64 m
Average Forward Velocity = 0.10 m/s

Trace of the Vehicle
Radius = 1.83 m
Average Forward Velocity = 0.10 m/s
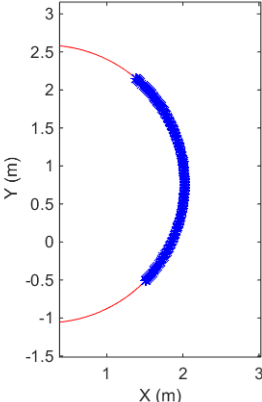
Trace of the Vehicle
Radius = 1.44 m
Average Forward Velocity = 0.10 m/s

Trace of the Vehicle
Radius = 1.00 m
Average Forward Velocity = 0.09 m/s

Trace of the Vehicle
Radius = 0.84 m
Average Forward Velocity = 0.08 m/s

Test Robot in Track Configuration Forward Velocity = 0.2 m/s

Trace of the Vehicle
Radius = 43.46 m
Average Forward Velocity = 0.20 m/s

Trace of the Vehicle
Radius = 33.49 m
Average Forward Velocity = 0.20 m/s

Trace of the Vehicle
Radius = 17.48 m
Average Forward Velocity = 0.20 m/s

149

Trace of the Vehicle
Radius = 7.62 m
Average Forward Velocity = 0.20 m/s

Trace of the Vehicle
Radius = 3.77 m
Average Forward Velocity = 0.20 m/s

Trace of the Vehicle
Radius = 2.97 m
Average Forward Velocity = 0.20 m/s

Trace of the Vehicle
Radius = 2.04 m
Average Forward Velocity = 0.20 m/s

Trace of the Vehicle
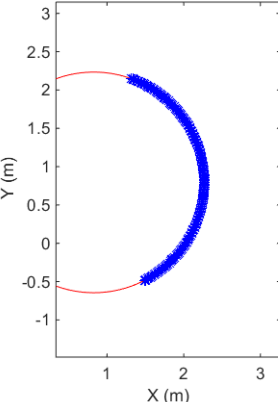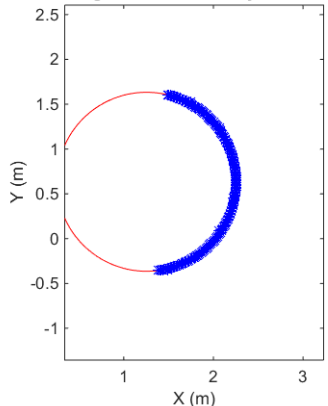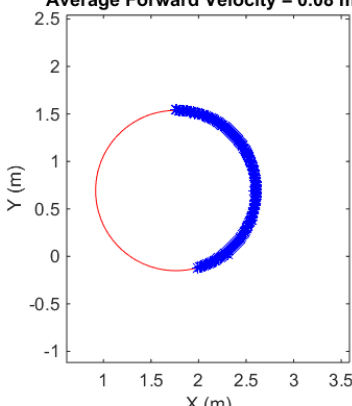Radius = 1.46 m
Average Forward Velocity = 0.19 m/s

Trace of the Vehicle
Radius = 1.18 m
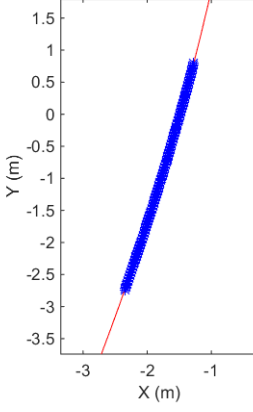Average Forward Velocity = 0.19 m/s

Trace of the Vehicle
Radius = 0.97 m
Average Forward Velocity = 0.19 m/s

Trace of the Vehicle
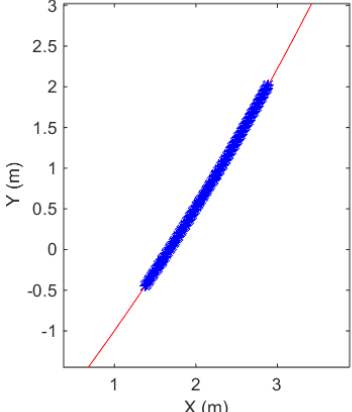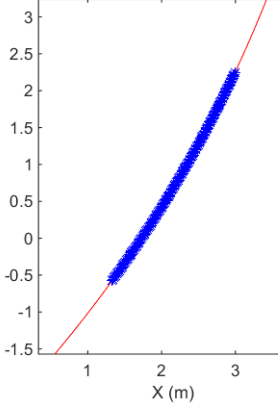Radius = 0.82 m
Average Forward Velocity = 0.18 m/s

150

BIBLIOGRAPHY

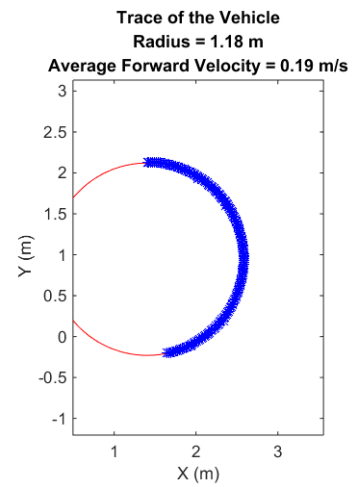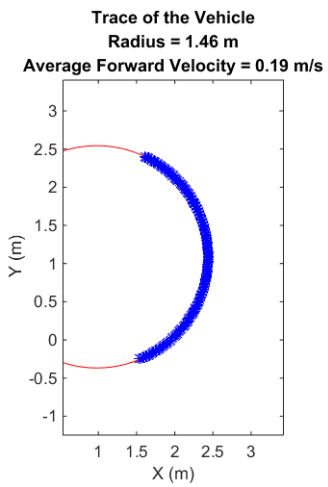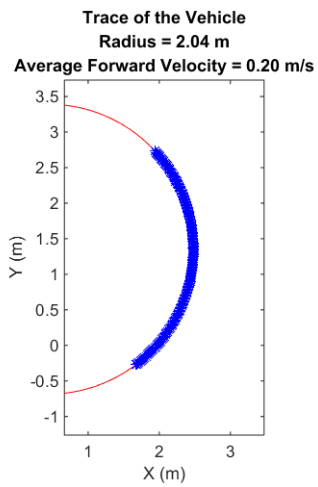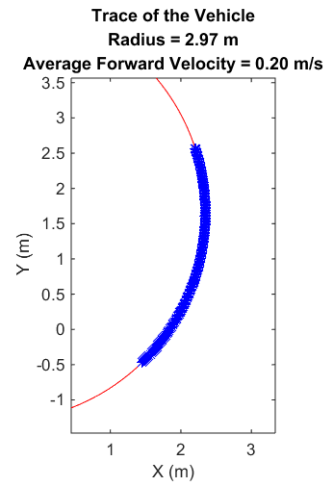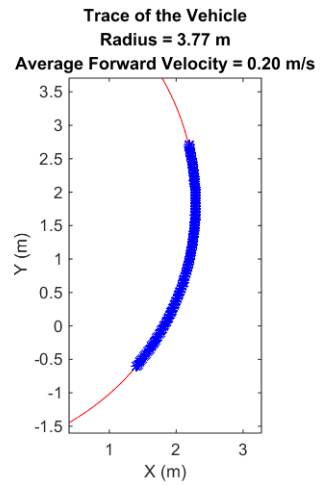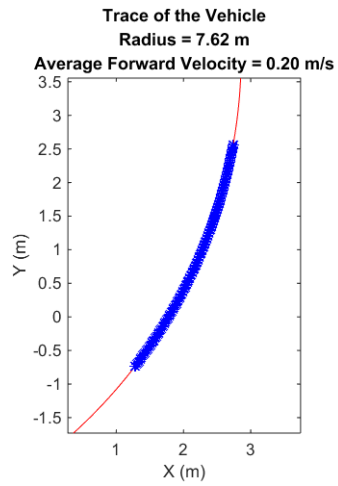[1] D. Gage, "A Brief History of Unmanned Ground Vehicle (UGV) Development Efforts," *Unmanned Systems Magazine,* vol. 13, no. 3, 1995.

[2] R. Padbury and X.Zhang, "Lithium-oxygen batteries-Limiting factors that affect performance," *Journal of Power Sources,* vol. 196, pp. 4436-4444, 2011.

[3] A. Feickert and N. Lucas, "Army Future Combat System (FCS) "Spin-Outs" and Ground Combat Vehicle (GCV): Background and Issues for Congress," Congressional Research Service, Library of Congress, Washington D.C., 2009.

[4] F. Kalhammer, B. Kopf, D. Swan, V. Roan and M. Walsh, "Status and Prospects for Zero Emissions Vehicle Techonology: Report of the ARB Independent Expert Panel 2007," Prepared for State of California Air Resouces Board, Sacramento, California, 2007.

[5] M. Bekker, Theory of Land Locomotion, The University of Michigan Press, 1962.

[6] K. Terzaghi, Theoretical Soil Mechanics, Chapman and Hall, 1943.

[7] M. Bekker, Off-the-road locomotion: research and development in terramechanics, The University of Michigan Press, 1960.

[8] M. Bekker, Introduction to terrain-vehicle systems, Ann Arbor: The University of Michigan Press, 1969.

[9] J. Wong, Terramechanics and off-road vehicle engineering: terrain behaviour, off-road vehicle performance and design, 2nd ed., Amsterdam, The Netherlands: Butterworth-Heinemann, 2010.

[10] J. Wong, Theroy of Ground Vehicles, 2nd ed., New York: John Wiley & Sons, Inc., 1993.

[11] M. Gobbi, M. Aiolfi, M. Pennati, G. Previati, F. Levi, M. Ribaldone and G. Mastinu, "Measurement of the forces and moments acting on farm tractor pneumatic tires," *Vehicle System Dynamics,* vol. 43, pp. 412-433, 2005.

[12] C. Fervers, "Improved FEM simulation model for tire-soil interaction," *Journal of Terramechanics,* vol. 41, no. 2-3, pp. 87-100, 2004.

[13] J. Lee, "Finite element modeling of interfacial forces and contact stresses of pneumatic tire on fresh snow for combined longitudinal and lateral slips," *Journal of Terramechanics,* vol. 48, pp. 171-197, 2011.

[14] K. Xia, "Finite element modeling of tire/terrain interaction: Application to predicting soil compaction and tire mobility," *Journal of Terramechanics,* vol. 48, pp. 113-123, 2011.

[15] R. Yong and E. Fattah, "Prediction of wheel-soil interaction and performance using the finite element method," *Journal of Terramechanics,* vol. 13, no. 4, pp. 227-240, 1976.

[16] A. Varghese, J. Turner, T. Way, C. Johnson and H. Dorfi, "Traction prediction of a smooth rigid wheel in soil using coupled Eulerian-Lagrangian analysis," in *SIMULIA Community Conference*, 2012.

[17] J. Pruiksma, G. Kruse, J. Teunissen and M. v. Winnendael, "Tractive performance modelling of the ExoMars rover wheel design on loosely packed soil using coupled Eulerian Lagrangian finite element techniques," in *11th Symposium on Advanced Space Technologies in Robotics and Automation*, 2011.

[18] T. Canfield and M. Murray, "The use of finite elements to model soil/track interactions in coupled multi-body dynamic simulations: Is real time simulation feasible?," in *Summer Computer Simulation Conference*, Reno, NV, 1992.

[19] J. Wong and A. Reece, "Prediction of rigid wheel performance based on the analysis of soil-wheel stresses part I. Performance of driven rigid wheels," *Journal of Terramechanics,* vol. 4, pp. 81-98, 1967.

[20] Z. Janosi and B. Hanamoto, "Analytical determination of drawbar pull as a function of slip for tracked vehicles in deformable soils," in *1st International Conference on Terrain-Vehicle Systems*, Turin, Italy, 1961.

[21] L. Ding, H. Gao, Z. Deng, K. Yoshida and K.Nagatani, "Slip ratio for lugged wheel of planetary rover in deformable soil: definition and estimation," in *International Conference on Intelligent Robots and Systems*, 2009.

[22] G. Ishigami, A.Miwa, K.Nagatani and K. Yoshida, "Terramechanics-based model for steering manuever of planetary exploration rovers on loose soil," *Journal of Field Robotics,* vol. 24, no. 3, pp. 233-250, 2007.

[23] W. Li, L. Ding, H. Gao, Z. Deng and N. Li, "Rover simulation based on terramechanics and dynamics," *Journal of Terramechanics,* vol. 47, pp. 227-242, 2010.

[24] W. Steeds, "Tracked vehicles," *Automobile Engineer,* pp. 143-148; 187-190; 219-222, 1950.

[25] K. Weiss, "Skid-steering," *Automobile Engineer,* pp. 22-25, 1971.

[26] J. Crosheck, "Skid-steering of crawlers," *SAE Transactions,* vol. 84, pp. 1390-1404, 1975.

[27] M. Kitano and H. Jyozaki, "A theoretical analysis of steer-ability of tracked vehicles," *Journal of Terramechanics,* vol. 13, no. 4, pp. 241-258, 1976.

[28] M. Kar, "Prediction of track forces in skid-steering of military tracked vehicles," *Journal of Terramechanics,* vol. 24, no. 1, 1987.

[29] J. Wong and C. Chiang, "A general theory for skid steering of tracked vehicles on firm ground," *Automobile Engineer,* vol. 215, pp. 343-355, 2001.

[30] W. Ehlert, B. Hug and I. Schmid, "Field measurements and analytical models as a basis of test stand simulation of the turning resistance of tracked vehicles," *Journal of Terramechanics,* vol. 29, no. 1, pp. 57-69, 1992.

[31] W. Yu, E. Collins and O. Chuy, Dynamic modeling and power modeling of robotic skid-steered wheeled vehicles, INTECH Open Access Publisher, 2011.

[32] W. Yu, O. Chuy, E. Collins and P. Hollis, "Analysis and experimental verification for dynamic modeling of a skid-steered wheeled vehicle," *IEEE Transactions on Robotics,* vol. 26, no. 2, 2010.

[33] O. Chuy, E. Collins, W. Yu and C. Ordonez, "Power modeling of a skid steered wheeled robotic ground vehicle," in *IEEE International Conference on Robotics and Automation*, Kobe, 2009.

[34] S. Al-Milli, L. Seneviratne and K. Althoefer, "Track-terrain modeling and traversability prediction for tracked vehicles on soft terrain," *Journal of Terramechanics,* vol. 47, pp. 151-160, 2010.

[35] T. Guo and H. Peng, "A simplified skid-steering model for torque and power analysis of tracked small unmanned ground vehicles," in *American Control Conference (ACC)*, 2013.

[36] K. Kozlowski and D. Pazderski, "Modeling and control of a 4-wheel skid-steering mobile robot," *Int. J. Appl. Math. Comput. Sci,* vol. 14, no. 4, pp. 477-496, 2004.

[37] J. Martinez, A. Mandow, J. Morales, S. Pedraza and A. Garcia-Cerezo, "Approximating kinematics for tracked mobile robots," *The International Journal of Robotics Research,* vol. 24, no. 10, pp. 867-878, 2005.

[38] J. Morales, J. Martinez, A. Mandow, A. Garcia-Cerezo and S. Pedraza, "Power consumption modeling of skid-steer tracked mobile robots on rigid terrain," *IEEE Transactions on Robotics,* vol. 25, no. 5, pp. 1098-1108, 2009.

[39] J. Yi, H. Wang, J. Zhang, D. Song, S. Jayasuriya and J. Liu, "Kinematic modeling and analysis of skid-steered mobile robots with applications to low-cost inertial-measurement-unit-based motion estimation," *IEEE Transactions on Robotics,* vol. 25, no. 5, pp. 1087-1097, 2009.

[40] Y. Wu, T. Wang, J. Liang, J. Chen, Q. Zhao, X. Yang and C. Han, "Experimental kinematics modeling estimation for wheeled skid-steering mobile robots," in *International Conference on Robotics and Biomimetics (ROBIO)*, Shenzhen, 2013.

[41] J. Pentzer and S. Brennan, "Model-based prediction of skid-steer robot kinematics using online estimation of track instantaneous centers of rotation," *Journal of Field Robotics,* vol. 31, no. 3, pp. 455-476, 2014.

[42] J. Wong, M. Barber and J. Preston-Thomas, "Some further studies of the mechanical properties of muskeg," *Journal of Terramechanics,* vol. 19, no. 2, 1982.

[43] J. Wong, M. Garber, J. Radforth and J. Dowell, "Characterization of the mechanical properties of muskeg with special reference to the vehicle mobility," *Journal of Terramechanics,* vol. 16, no. 4, 1979.

[44] J. Wong and J. Preston-Thomas, "On the Characterization of the Shear Stress-Displacement Relationship of Terrain," *Journal of Terramechanics,* vol. 19, no. 4, 1983.

[45] H. Shibly, K. Iagnemma and S. Dubowsky, "An equivalent soil mechanics formulation for rigid wheels in deformable terrain, with application to planetary exploration rovers," *Journal of Terramechanics,* vol. 42, pp. 1-13, 2005.

[46] i. Coroperation, "iRobot 510 Packbot," [Online]. Available: http://www.irobot.com/~/media/Files/Robots/Defense/PackBot/iRobot-510-PackBot-Specs.pdf.

[47] Z. Jia, W. Smith and H. Peng, "Fast analytical models of wheeled locomotion in deformable terrain for mobile robots," *Robotica,* vol. 31, no. 1, pp. 35-53, 2013.

[48] W. Smith, H. Peng, Z. Filipi, D. Kramer and M. Pozolo, "Development of a design tool for small off-road unmanned wheeled ground vehicles: a case study," in *AUVSI's Unmanned Systems*, 2011.

[49] J. Pentzer, S. Brennan and K. Reichard, "On-line estimation of vehicle motion and power model parameters for skid-steer robot energy use prediction," in *American Control Conference(ACC)*, Portland, 2014.

[50] I. The Mathworks, "What Is Camera Calibration?," 1994-2016. [Online]. Available: http://www.mathworks.com/help/vision/ug/camera-calibration.html. [Accessed 20 January 2016].

[51] I. The Mathworks, "vision.BlobAnalysis System object," 1994-2016. [Online]. Available: http://www.mathworks.com/help/vision/ref/vision.blobanalysis-class.html?refresh=true. [Accessed 16 January 2016].

[52] J. Wong, "The effect of vibrations on the performance of terrain-vehicle systems," *Journal of Terramechanics,* vol. 7, pp. 11-21, 1970.

[53] J. Wong, "Effect of vibration on the performance of off-road vehicles," *Journal of Terramechanics,* vol. 8, pp. 25-42, 1972.

[54] L. Laib, "On the mobility of cross-country vehicles, with emphasis on modeling their dynamic motion," *Vehicle System Dynamics,* vol. 29, pp. 682-703, 1998.

[55] P. K. a. G. A. L. Laib, "The effects of off-road vehicle on the soil cohesion and internal friction," *Jarmuvek es Mobilgepek,* vol. 2, pp. 132-152, 2008.

[56] NASA, "Wheels and Legs," 2016. [Online]. Available: http://mars.nasa.gov/msl/mission/rover/wheelslegs/. [Accessed 04 2016].